Title
INSTABILITY OF AN ALTERNATING-CURRENT POSITIVE COLUMN IN A MAGNETIC FIELD

Author
Rugge, Henry F.

Publication Date
1963-04-22

UCRL-10698

University of California

Ernest O. Lawrence Radiation Laboratory

INSTABILITY OF AN ALTERNATING-CURRENT POSITIVE COLUMN IN A MAGNETIC FIELD

DISCLAIMER

Research and Development

UCRL-10698
UC-20 Controlled
Thermonuclear Processes
TID-4500 (19th Ed.)

UNIVERSITY OF CALIFORNIA
Lawrence Radiation Laboratory
Berkeley, California

Contract No. W-7405-eng-48

INSTABILITY OF AN ALTERNATING-CURRENT POSITIVE COLUMN IN A MAGNETIC FIELD

Henry F. Rugge

(Thesis)

April 22, 1963

Printed in USA. Price $2.50. Available from the
Office of Technical Services
U. S. Department of Commerce
Washington 25, D.C.

INSTABILITY OF AN ALTERNATING-CURRENT POSITIVE COLUMN IN A MAGNETIC FIELD

Contents

INSTABILITY OF AN ALTERNATING-CURRENT POSITIVE COLUMN IN A MAGNETIC FIELD

Henry F. Rugge

Lawrence Radiation Laboratory
University of California
Berkeley, California

April 22, 1963

ABSTRACT

The positive column of a glow discharge in a magnetic field is known to become macroscopically unstable at some critical magnetic field, B_c. Kadomtsev's proposed driving mechanism for this helical ($m = 1$) instability is such that if one periodically reverses the axial electric field at a frequency greater than the growth rate of the instability, one would expect it to be suppressed.

A detailed study of the instability was made in direct-current half-wave-rectified (unidirectional) current, and square and sinusoidal alternating-current glow discharges in H_2, D_2, He, Ne, and Ar. The study of the direct-current discharges corroborated previous results and yielded experimental parameters necessary for comparison with theory. Electron-temperature measurements at $B = 0$ and near the critical magnetic field were obtained by employing single- and double-probe techniques. Half-wave rectified discharges over a wide range of frequencies yielded instabilities whose onset (B_c) and helical nature duplicated those of the direct-current discharges. However, the instability in the alternating-current discharges was found to be suppressed as the electric-field reversal frequency was increased; this substantiates the Kadomtsev model of the driving mechanism.

Although the model of Kadomtsev is not specifically applicable to time-dependent discharges, the quasi-direct-current nature of the square-wave discharges encourages a comparison between the theory and the alternating-current experiments. The frequency-dependent suppression of the alternating-current instability is compared with the theoretical growth rates. The effect of several m-value modes is calculated, and results show good qualitative agreement. Good quantitative agreement is obtained when the Johnson and Jerde modification of the Kadomtsev theory is employed.

I. INTRODUCTION

The positive column of a glow discharge has been shown to exhibit a macroscopic instability when a longitudinal magnetic field of sufficient strength is applied.[1-5] Several theories have been proposed to explain this phenomenon.[6-10] Aside from the intrinsic value of understanding the instability mechanism, it is also interesting to note that this mechanism is not restricted to the positive column. Simon and Guest[11] have shown that the instability can develop without an applied electric field, because of unequal streaming rates of ions and electrons in the longitudinal direction. Since the proposed instability mechanism is not very sensitive to the degree of ionization, Hoh[8] suggests it may also be operative in highly ionized plasmas such as the Stellarator and Zeta machines. Similar instabilities have been observed in a highly ionized Cs plasma[12] and in the electron-hole plasma of a semiconductor.[13-16] Our positive-column work investigates in particular the properties related to the growth mechanism of the instability.

Positive columns of glow discharges have been widely used in gas-discharge and plasma physics work.[17] They are not only easily produced in many gases, but do provide a steady-state weakly ionized plasma whose parameters are reasonably well known. One can vary discharge parameters such as electron temperature and axial electric field in a known manner by simply changing the tube radius or pressure.

The appearance of the normal cold-cathode glow discharge is described in Fig. 1, and is accompanied by the accepted classification of its various regions.[18] The axial distribution of several of its parameters is also included. The use of hot cathodes, as in this experiment, eliminates the cathode fall region, V_c, hence the discharge requires less maintenance voltage.

The positive column is that region bounded on the cathode side by the Faraday dark space, and near the anode by the anode glow. It is so called because it connects the negative zones to the anode; that

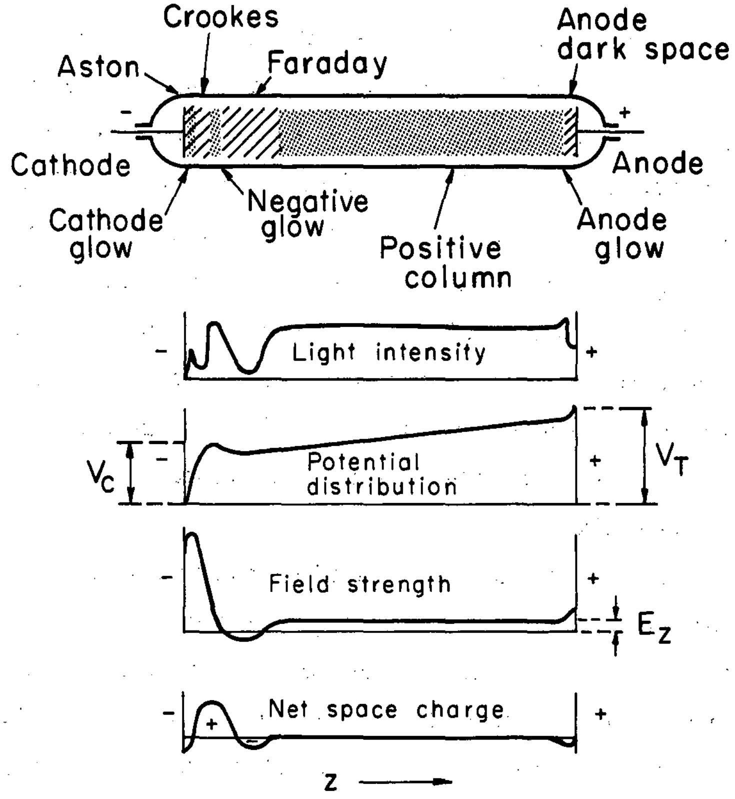

MU-29828

Fig. 1. Classification of the glow-discharge regions, and axial distribution of some important parameters.

is, its potential is positive with respect to the cathode region. The column serves only as a conducting path in which the longitudinal electric field is constant; there is little or no net space charge, i.e., $n_+ \approx n_- = n$.

Typical positive-column parameters are as follows. Neutral gas pressures range from 10^{-2} to 10 mm Hg, while electron densities are of the order of 10^9 to 10^{11} particles per cm^3, yielding a percentage ionization of approximately $10^{-3}\%$. Electron temperatures are normally a few electron volts, whereas ion and neutral temperatures are much lower. Typical electron neutral mean free paths are in the mm to cm range. The Debye length $[\lambda_D = (kT_-/4\pi ne^2)^{1/2}]$, a measure of the shielding distance of one ion from another by the electrons, is much less than the dimensions of a normal discharge vessel, and we are dealing with a weakly ionized plasma dominated by electron-neutral and ion-neutral collisions.

Bickerton and von Engel analyzed the positive column of a He discharge in a longitudinal magnetic field, making the discharge long enough to avoid end effects.[19] Their maximum field strength was approximately 600 G. They concluded that in zero magnetic field the Langmuir theory of free ion fall[20] described best the properties of the discharge, whereas in a magnetic field Schottky's theory of ambipolar diffusion[21] applied. No instabilities were observed.

This work was extended by Lehnert[3] and Lehnert and Hoh[4] by employing very large magnetic fields in similar geometries. The axial electric field was measured as a function of magnetic field strength. The magnetic field decreases the loss of charged particles to the wall, hence the electric field necessary to maintain the discharge was expected to decrease monotonically. Agreement was found up to a certain critical magnetic field, B_c. Above this magnetic field the electric field increased markedly, denoting an increased loss of particles to the wall.

A detailed examination of the phenomenon was done by Allen et al.[1] and Paulikas and Pyle.[2] Their study of the positive column has shown that at B_c a macroscopic instability appears in the column. This instability transforms the azimuthally symmetric column into a constricted rotating helical state that was photographically recorded with a rotating-mirror streak camera. The rotational frequency and wavelength of the helix, as well as the critical magnetic field strength, were documented as a function of the discharge parameters.

The most widely accepted theory has been given by Kadomtsev and Nedospasov.[6] They consider the growth of a screw-shaped perturbation superimposed on the stationary electron density and potential. The other theories are modifications of Kadomtsev's work[8, 9, 10] except for a theory of Hoh which involves the stability of the sheath surrounding the plasma.[7] Both the Hoh and Kadomtsev theories yield values of B_c that give good agreement with experiment, but Hoh's theory does not discuss the mechanism by which the sheath affects the plasma, whereas the Kadomtsev theory does correctly predict the nature of the instability. Hoh now considers the theoretical explanation given by Kadomtsev and Nedospasov to be the correct one.[8]

Other experiments[22-25] in various types of discharges immersed in magnetic fields also showed increased losses when compared with previous classical theories. These were followed by theoretical papers discussing the results on both a microscopic and macroscopic basis.[26, 27, 28]

The ac work described herein is an extension of the dc positive-column work. Previous ac discharge work in our frequency range (below 100 kc/sec) is very sparse, even without the presence of a magnetic field; a summary of this work is given by Francis.[29] Our experiment investigates the onset of the instability as a function of discharge parameters, including the ac frequency. Both sine-wave and square-wave current forms are employed. Square current wave shapes best simulate quasi-dc conditions, that is, a constant current that is reversed every half-cycle. In this manner dc conditions should prevail over this half-cycle, yet the instability should also be suppressed if the current-reversal frequency is greater than the growth rate of the instability. A comparison is then made between the experimental results and the dc theory of Kadomtsev and Nedospasov, and one of its modifications due to Johnson and Jerde.[9]

II. THEORY

A. Classical Theory

In the uniform steady-state positive column the electric field must have such a value that the number of electrons and ions produced per second just balances the loss to the walls. It is assumed that ionization in the gas occurs only by single collisions and that the charged-particle loss is due to ambipolar diffusion. Only collisions between charged particles and neutrals are considered, because of the low fractional ionization. Volume recombination in the gas is neglected (Pahl has shown this is a negligible effect[30]). In the noble gases, as well as in hydrogen and deuterium, it is also possible to neglect electron attachment. Employing these assumptions one writes the particle-balance equation

$$\nabla^2 n(r) + \frac{\nu_i}{D_a} n(r) = 0, \qquad \text{(II-1)}$$

where ν_i is the number of ion pairs produced per second per electron, and D_a, the ambipolar diffusion coefficient,[31] is given by

$$D_a = \frac{D_+\mu_- + D_-\mu_+}{\mu_+ + \mu_-} \quad \frac{1}{1 + \mu_+\mu_- B^2}, \qquad \text{(II-2)}$$

where $D_\pm$ and $\mu_\pm$ are the electron and ion diffusion coefficients and mobilities at $B = 0$. The solution to Eq. (II-1) in cylindrical geometry is

$$n(r) = n(0)\, J_0\left[\left(\frac{\nu_i}{D_a}\right)^{1/2} r\right], \qquad \text{(II-3)}$$

where J_0 is the zero-order Bessel function of the first kind. The boundary condition $n(R) = 0$ gives

$$\nu_i = \left(\frac{2.4}{R}\right)^2 D_a, \qquad \text{(II-4a)}$$

if the average mean free path $\bar{\lambda} << R$ (Schottky theory). If $\bar{\lambda} \approx R$, or if the ratio of the ion density at the walls to that on the axis is not much smaller than one, the modified Schottky theory[19] applies,* and the ionization rate is related to other parameters as follows

$$\frac{4D_a}{Ru_+} = \frac{1}{x}\,\frac{J_0(x)}{J_1(x)}\,, \tag{II-4b}$$

where $x = (\nu_i/D_a)^{1/2}R$ and u_+ is the thermal-ion velocity.

The ionization rate ν_i depends strongly upon the form of the ionization cross section as well as the shape of the electron-velocity distribution, which is not necessarily Maxwellian. Measurements of electron-velocity distributions in a discharge with standing striations have shown the presence of a high-energy group.[49] Usually the positive column exhibits striations, either moving or standing; two notable exceptions are alkali discharges[32] and helium at pressures less than about 0.5 mm Hg. Recent probe measurements by Müller have shown that in a He positive column the electron-velocity distribution is near Maxwellian and does not change much in form with magnetic field.[5]

The electron temperature necessary to produce the required ionization rate ν_i may be obtained from Eq. (II-4). Also, the axial electric field E_z is connected with the electron temperature through the energy balance relation; that is, the energy gain of an electron in the field E_z between two collisions should, on the average, balance the loss of energy of the electron in a collision. Denoting $x(T_-)$ as the fractional energy loss by an electron in one collision, it can be shown that[33, 34]

$$E_z = \left(\frac{64}{\pi}\right)^{1/4}\left[x(T_-)\right]^{1/2}\frac{kT_-}{e\lambda_-}\,, \tag{II-5}$$

where λ_- is the electron mean free path. The presence of a longitudinal magnetic field decreases the loss of particles to the wall, hence the electron temperature necessary to maintain the discharge decreases

---

*It should be noted that the modified Schottky theory is also correct for $\bar{\lambda} \ll R$.

and consequently so does the axial electric field. This was demonstrated at low magnetic fields by Bickerton and von Engel.[19]

B. Instability Theory

As noted in the Introduction, several theoretical investigations of the stability of the positive column in a longitudinal magnetic field have been carried out. Hoh[7] starts with Bohm's criterion for the stability of a sheath[35] and shows that a sufficiently strong magnetic field can affect the radial drift of the ions such that the sheath is no longer stable. However, a propagation mechanism of the instability into the plasma is not described. Further, Hall has criticized that Bohm's criterion is not applicable to the positive column due to the small potential drop across the sheath.[36] Hoh later concurred with the Kadomtsev and Nedospasov approach. Their theory is presented in some detail below. Subsequently, other authors attempted to put Kadomtsev's theory on a firmer physical and mathematical basis.[8, 9, 10] A brief description of these theories follows the Kadomtsev analysis, and a more detailed comparison appears in Appendix A.

Kadomtsev and Nedospasov employ a perturbation analysis with the following assumptions: $\Omega_- \tau_- \gg 1 \gg \Omega_+ \tau_+$, $D_+ \approx 0$, and $1/\tau_+ \gg \omega$, where $\Omega_\pm$ and $\tau_\pm$ are the ion and electron cyclotron frequencies and the mean time between collisions with neutrals, respectively, D_+ is the ion diffusion coefficient, and ω is the frequency of oscillations considered.

The equations of motion and continuity for electrons and ions are

$$\frac{\kappa T_\mp}{m_\mp n} \nabla n = \mp \frac{e}{m_\mp} \mathbf{v}_\mp \times \mathbf{B} \pm \frac{e}{m_\mp} \nabla V - \frac{\mathbf{v}_\mp}{\tau_\mp}, \tag{II-6}$$

$$\frac{\partial n}{\partial t} + \nabla \cdot (n \mathbf{v}_+) = \frac{\partial n}{\partial t} + \nabla \cdot (n \mathbf{v}_-) = \nu_i n, \tag{II-7}$$

where $\underset{\sim}{v}_{\pm}$ are the ion and electron drift velocities, and V is the electric potential. In the equilibrium state, n and V depend only on distance from the axis of the tube. Assuming that the mean free path of the ions $\lambda_+ << R$ and equating the density at the wall to zero (Schottky condition), the following unperturbed equations are obtained:

$$n_0(r) = n(0) J_0 \left(\frac{2.4}{R} r \right) , \qquad \text{(II-8)}$$

$$\frac{dV_0}{dr} = \frac{D_-}{\mu_- + \mu_+ (\Omega_- \tau_-)^2} \frac{1}{n_0} \frac{dn_0}{dr} . \qquad \text{(II-9)}$$

Perturbations of the form $J_1[(3.83/R)r]$ are introduced such that

$$n(\underset{\sim}{r}, t) = n(0) J_0 \left(\frac{2.4}{R} r \right) + n_1 J_1 \left(\frac{3.83}{R} r \right)$$

$$\cdot \exp[i(m\phi + kz - \omega t)] \qquad \text{(II-10a)}$$

and

$$V(\underset{\sim}{r}, t) = V_0(r) + V_1 J_1 \left(\frac{3.83}{R} r \right)$$

$$\cdot \exp[i(m\phi + kz - \omega t)] . \qquad \text{(II-10b)}$$

Linearizing the resulting equations, then multiplying them by the weighting factor $J_1(3.83r/R)$ and integrating over r,* they obtain a dispersion relation for the frequency ω as a function of the wave number $k = 2\pi/\lambda$. Thus the stability criterion, $\text{Im}(\omega) < 0$, is obtained.

Their choice of $J_1(3.83r/R)$ as a perturbation is somewhat arbitrary and their multiplication of the continuity equations by $J_1(3.83r/R)$ before averaging is not clear, although Hoh[37] states that

---

*Since the chosen perturbation does not exactly solve the equations, Kadomtsev requires that the average deviation in the range $0 < r < R$ be zero.

the latter manipulation may be regarded as an application of the approximative method of Galerkin[38] for solution of differential equations.† Their choice of $V_1(r)$ leading to $V_1(R) = 0$ as a boundary condition has been criticized by Ecker.[39]

Disregarding these criticisms for the moment, we continue. For stability we have

$$\mathrm{Im}(\omega) = \left(\frac{3.83}{R}\right)^2 \frac{D_-}{y(\Omega_-\tau_-)^2} \left(\frac{1}{\left(\frac{0.33}{\Omega_-\tau_-}\; m\; \frac{\mu_-}{\mu_+}\right)^2 + \left[\frac{1+y}{y} + \frac{k^2}{0.79}\; \frac{\mu_-}{\mu_+} \left(\frac{R}{3.83}\right)^2\right]^2} \right)$$

$$\left\{-\frac{1.28+y}{0.8(y+1)}\, x^4 - (2+y)x^2 - 0.12\,\frac{\mu_-}{\mu_+}\,\frac{ym^2}{y+1} - 0.6(1+y) + 0.2\,xyv^* m\,\frac{\mu_-}{\mu_+}\right\} < 0, \tag{II-11}$$

where

$$x \equiv \frac{k\Omega_-\tau_- R}{3.83}\,,$$

$$v^* \equiv \frac{v_{-z} R}{2.4D_-}\,,$$

and

$$y \equiv \frac{\mu_+}{\mu_-}\,(\Omega_-\tau_-)^2\,.$$

Since the sign of Eq. (II-11) depends only on the sign of the terms in curly brackets, the condition for stability can be simplified to

$$Kx^4 + Fx^2 + G_1 + G_2 > 0.16\, mv^* x\, \frac{\mu_-}{\mu_+}\,, \tag{II-12}$$

where

$$K \equiv \frac{1.28 + y}{y(y+1)}\,,$$

---

† This method is also known as the Ritz method.

$$F \equiv \frac{0.8(y+2)}{y} ,$$

$$G_1 \equiv \frac{0.48(1+y)}{y} ,$$

$$G_2 \equiv 0.1 \frac{\mu_-}{\mu_+} \frac{m^2}{1+y} .$$

Upon examining the equations leading to Eq. (II-12) one finds the following physical significance.[6, 8, 40] The right-hand side of this equation contains the longitudinal electric field $[v^* = (\mu_- E_z R)/2.4D_-]$ and is the driving mechanism of the instability. The term Kx^4 provides stabilization due to diffusion and conduction along the magnetic field, while G_1 represents the same effects perpendicular to the axis. In addition Fx^2, which arises from the coupling between longitudinal and transverse diffusion effects, also tends to stabilize the perturbation. In general, G_2 is the most important term contributing to stabilization. It arises from an $\underset{\sim}{E}_{or} \times \underset{\sim}{B}$ rotation of the perturbed electron distribution, where $\underset{\sim}{E}_{or}$ is the unperturbed radial electric field.

A qualitative picture of the onset of the instability[8] can be given with the aid of Fig. 2. The solid lines represent the screw-shaped (m = 1) perturbation. The ions can be assumed to remain fixed with respect to the electrons due to their relatively low mobility and temperature. Now, in an electric field (E_z) applied as indicated, the entire electron screw will be displaced in the positive z direction. The electron screw would then occupy the zone indicated by the dashed lines. Hence, the axial electric field causes a charge separation which in turn creates a perturbed azimuthal electric field as indicated, in the positive ϕ direction. This produces a radial drift $\underset{\sim}{E}'_{\phi} \times \underset{\sim}{B}$ that drives the plasma to the wall. However, the $\underset{\sim}{E}_{or} \times \underset{\sim}{B}$ azimuthal drift rotates the screw in the negative ϕ direction, tending to counteract the destabilizing effect of the axial electric field. Onset of the instability occurs when the destabilizing effect outweighs the stabilizing mechanisms. It should be noted that the instability can grow for E_z parallel or antiparallel to B—the pitch of the spiral is simply reversed. Hence

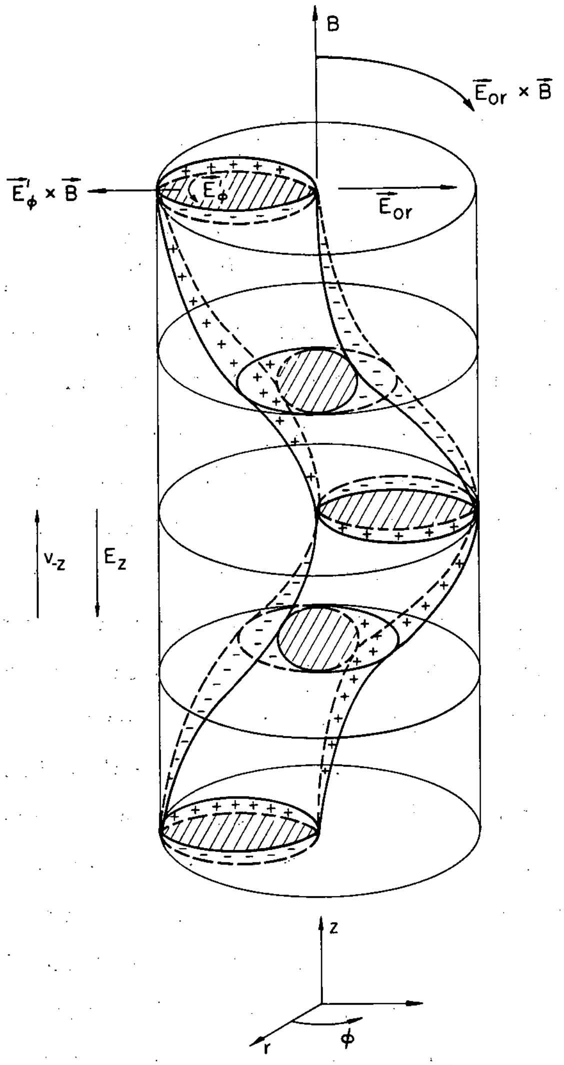

MU-29830

Fig. 2. Schematic diagram from Hoh[8] for left-handed screw instability for m=1. The perturbed-electron distribution is indicated by the dashed lines, while that of the ions is represented by the solid lines.

the instability should be suppressed if the axial electric field were reversed in a time short compared with the growth time of the instability.

When the stability criterion is put in the form of Eq. (II-12) it can be seen that instability occurs only for $m > 0$. Equation (II-12) can be further reduced. At B_c, $\partial(\mathrm{Im}(\omega))/\partial k = 0$ (Fig. 3), as well as $\mathrm{Im}(\omega) = 0$. By taking the derivative, one is able to obtain

$$x^2 = \frac{-F + [F^2 + 12K(G_1 + G_2)]}{6K} ,$$

$$0.08v^* = \frac{\mu_+}{m\mu_-} [2Kx^2 + F]x. \qquad \text{(II-13)}$$

Equation (II-13) can then be solved for B_c and k in terms of the discharge parameters.

Hoh[8] attempts to put Kadomtsev's analysis on a firmer physical basis by explaining the instability mechanism in terms of physical arguments, as presented earlier in this section (see Fig. 2). He assumes a squared parabolic density distribution, which is very similar to Kadomtsev's perturbed density distribution $J_1(3.83\ r/R)$, and shows how the perturbed radial potential can be related to the perturbed density. This results in a perturbed potential that is finite at the wall, thus eliminating an objection to Kadomtsev's analysis. Hoh's analysis yields values of B_c quite close to those calculated from the Kadomtsev theory.

Johnson and Jerde,[9] on the other hand, attempt to put Kadomtsev's analysis on a firmer mathematical basis. They include the effect of the magnetic field on the ions, and solve the resulting equations with rigor. However, they obtain an infinite determinant of eigenvalues, $\omega(k)$, for the dispersion relation. Only the first term is used and this gives an approximate solution. They justify this approximation by showing that the next-order terms yield only about a + 6% correction, but they cannot prove convergence of the determinant. Their first-order

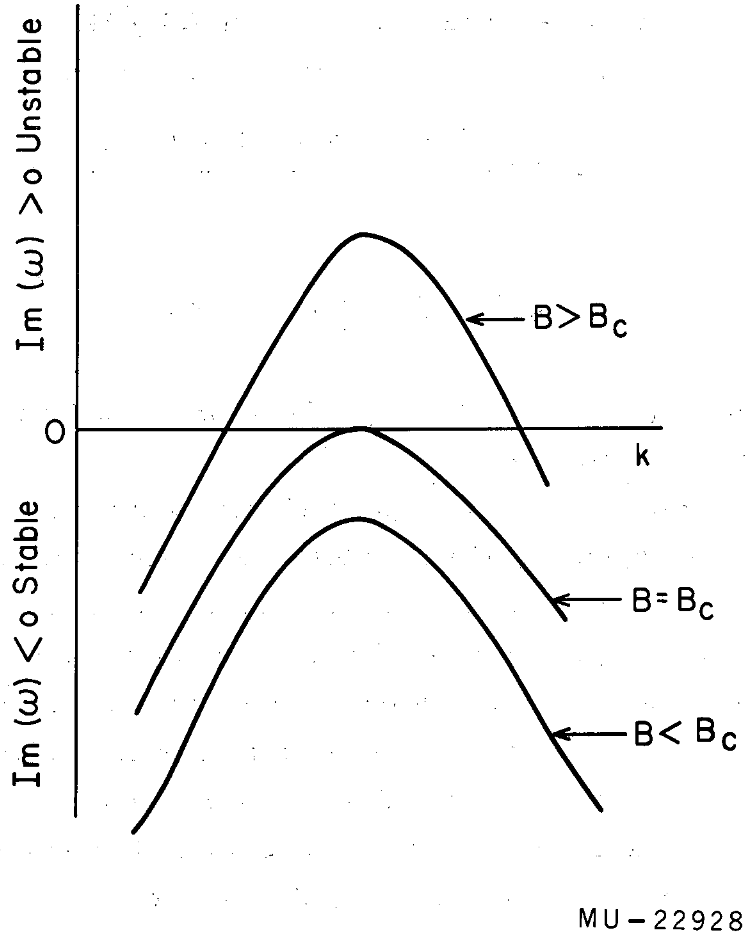

Fig. 3. The form of Im(ω) vs k for several values of B, Eq. (II-11).

approximation yields a density perturbation identical to that of Kadomtsev, while their perturbed potential has the form $J_1(3.83\ r/R)/J_0(2.4\ r/R)$, which is finite at the wall. Calculations from their theory appear in Sec. IV-E along with those from the Kadomtsev theory. A more detailed description of their approach appears in Appendix A.

Ecker[39] approaches the problem from a somewhat different viewpoint. He investigates whether an initial disturbance in the total particle number increases or decreases with time. He uses a trial function f(r) for the perturbed density $f(r) \propto r^{\nu} J_1(3.83\ r/R)$, with a perturbed potential $\propto f(r)/J_0(2.4\ r/R)$. At $\nu = 0$ Kadomtsev's perturbed density $J_1(3.83\ r/R)$ is obtained with $V_1 = J_1(3.83\ r/R)/J_0(2.4\ r/R)$; i.e., the same form as Johnson and Jerde. However, by varying ν he can vary the form of n_1 (and consequently V_1). Even small changes in ν ($\nu = 0.1$, for instance) cause appreciable changes in the value of B_c (see Figs. A-1 and A-2).

Kadomtsev's analysis and that of Johnson and Jerde will be used for comparison with the ac measurements. They are both in a form that facilitates comparison with a large volume of data.

III. EXPERIMENTAL PROCEDURE

A. Apparatus

The basic apparatus used in this experiment is shown in Fig. 4. The discharges were formed in 300-cm-long Pyrex tubes of radii 2.75 and 1.27 cm. Electrodes containing tungsten filaments were attached to both ends of the tube by means of ground-glass joints sealed with Apiezon wax. The filaments were run such that they were not emission limited. This arrangement permitted rapid repair or exchange of electrodes.

Two variable-frequency ac power sources were used in the course of the experiment. One was a 5-kW low-frequency sine-wave oscillator which would supply discharge currents from 100 mA to 2 A rms.* in the frequency range from 7 to 70 kc. The power source used for most of the measurements was a device specifically designed for the experiment to amplify the signals from standard Hewlet-Packard 200AB and 211A sine-wave and square-wave audio oscillators. It enabled us to draw currents from 100 mA to 1 A in the frequency range from 0 to 50 kc. A schematic diagram of the amplifier appears in Fig. 5. The high-power sine-wave oscillator was used mainly when very high currents (1 A to 2 A) were needed to obtain sufficient light intensity to take streak-camera photographs.

The magnetic field was provided by ten 9-in. -i. d. 6-in. -wide water-cooled coils that were spaced 2-1/4 in. apart. This was done to permit space for streak photography and photomultiplier (P. M.) monitoring of the plasma. The power supply involved provided dc field strengths that could be continuously varied from 0 to 7 kG. The axial magnetic field was found to vary by ± 3% at a radius of 4 cm, and by less than ± 2% on the axis due to the spacing of the coils.

---

*All sine-wave and square-wave currents referred to in this text will be rms and peak values, respectively, unless otherwise noted.

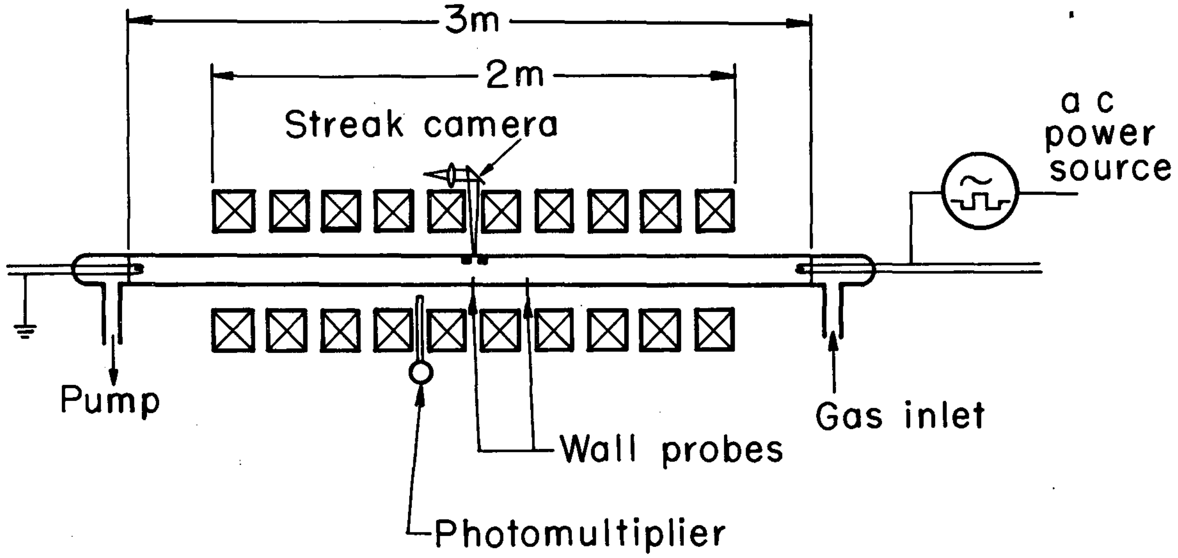

MU-27752

Fig. 4. Schematic diagram of the experimental apparatus.

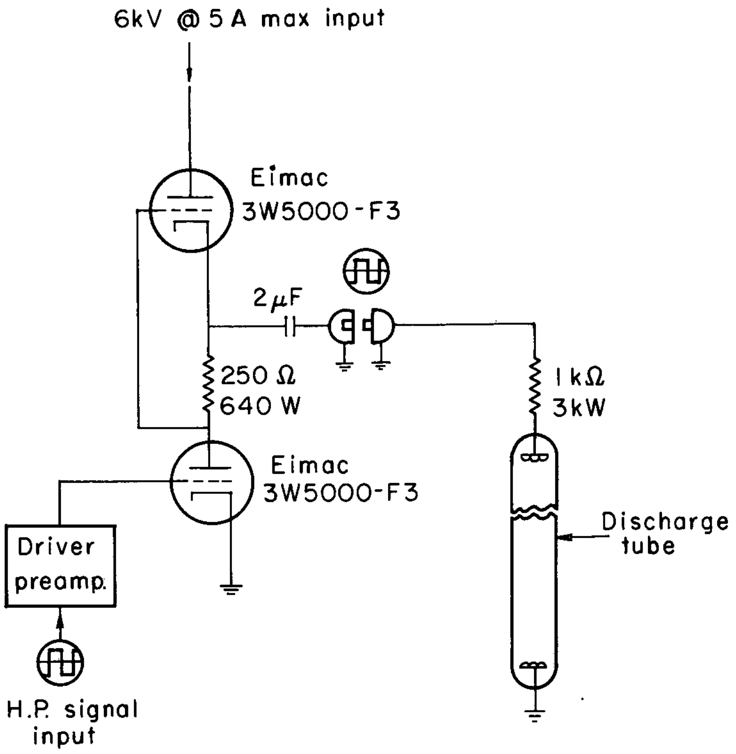

MU-29829

Fig. 5. Schematic diagram of ac amplifier.

The vacuum was provided by a 4-in. oil diffusion pump in conjunction with a refrigerated baffle system and liquid-nitorgen cold trap. The base pressure of this system was 10^{-7} mm Hg. The gases were continuously bled through the tube during an experimental run. Prior to a run the tube was allowed to "clean up" by flushing the system with the proper gas and running the discharge for a few hours. "Unclean" tubes could be identified by a difference in color and sometimes an inconclusive value of B_c. The neutral-gas pressure was measured with an Autovac gauge which was calibrated with an oil manometer. The neutral-gas temperature was estimated from thermocouple measurements on the glass tube.

B. Diagnostics

Two Langmuir-type wall probes were situated 20 cm apart, midway between the electrodes. The probes were made from 0.5-mm-diam tungsten rod ground flat at one end. They protruded approximately 1 mm into the discharge. The probes were shielded externally by a 1/8-in.-thick copper box. The probe signals were led to a 541 Tektronix oscilloscope containing a high-gain differential preamplifier. In this way the probe voltages could be displayed separately or their difference voltage taken, the latter being proportional to the axial electric field. The output from the oscilloscope was then rectified and these data were plotted on an x-y recorder as a function of applied magnetic field strength. The experimental arrangement is shown in Fig. 6.

The total voltage across the tube, V_T, and the discharge current I were continuously monitored on an oscilloscope. At times the total voltage across the tube was plotted vs magnetic field on the x-y recorder in the same manner as the probe signals. All experimental runs were taken at constant current (time-averaged).

The positive column was also monitored optically by two methods indicated in Fig. 7. A rotating-mirror streak camera enabled us to obtain space- and time-resolved information on the luminous structure of the plasma. Two-dimensional views were obtained by

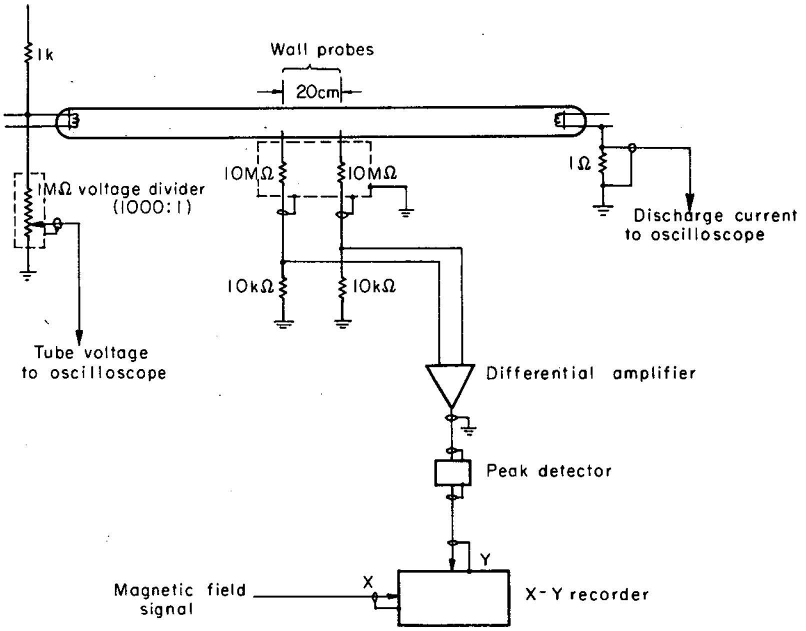

MU-29827

Fig. 6. Electrical monitoring system.

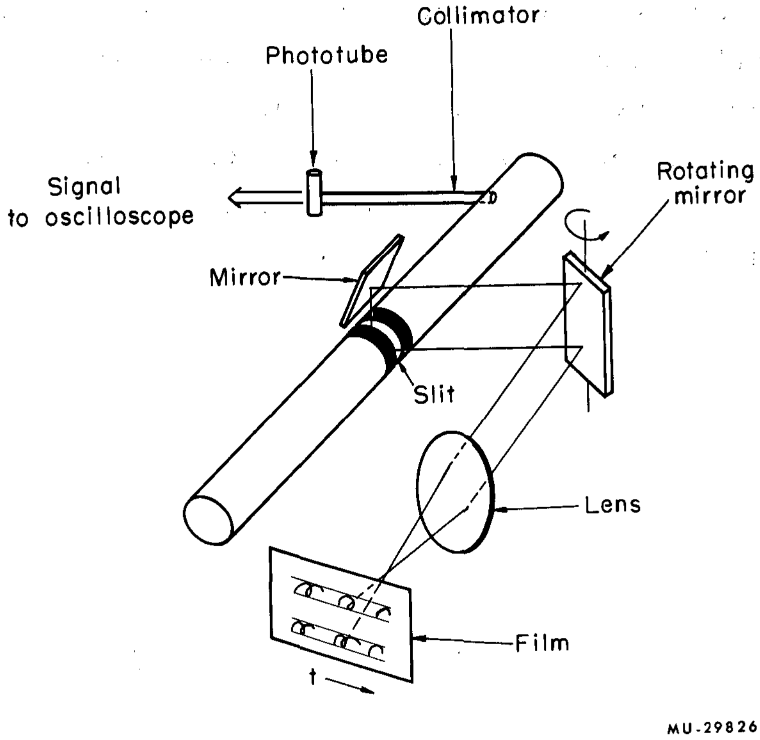

Fig. 7. Optical monitoring system.

placement of the mirror as indicated. Because of the limited light intensity, Polaroid 10 000-speed film was used in the majority of the photographs.

The time-varying light intensity was continually observed with a photomultiplier tube (Fig. 7) and the signal displayed on an oscilloscope. Its purpose was twofold. First, it enabled us to determine the wave shape of the light intensity below the critical field, which could be compared to the tube-voltage and discharge-current wave shapes. Secondly, the onset of the instability could be seen quite plainly as a sharp increase in the light intensity, and was accompanied by noise at the frequency of rotation of the spiral. This is shown in Fig. 21.

IV. RESULTS

A. Direct-Current and Half-Wave Rectified Discharges

Direct-current and half-wave rectified discharges were run to lay the groundwork for the ac discharge measurements. The results of this work and some background necessary for the discussion of the ac work will be presented in this section.

Critical magnetic field measurements were obtained in the dc discharges as a function of gas, tube radius, and pressure–yielding excellent agreement with the previous results of Paulikas and Pyle.[2] Total discharge voltages and axial electric fields were measured in order to compare them with the corresponding ac values. This comparison is given in Table II of Sec. IV-B.

The onset of the instability was determined by plotting either the axial electric field of the positive column or the total discharge voltage vs the applied magnetic field. Both methods gave the same value of B_c. Figure 8 shows typical experimental measurements of the electric fields as functions of the applied magnetic fields in a dc discharge. The experimental data represented by the solid lines were taken from the work of Paulikas and Pyle. The dashed lines represent their calculation of the axial electric field [Eq. (II-5)] by using classical theory. The onset of the instability is recognized by the sharp increase in the magnitude of the electric field. Similar curves were obtained when the total discharge voltage was plotted vs magnetic field.

The nature of the instability could be studied with the aid of a rotating-mirror streak camera. It has been shown that the onset of the instability is characterized by the transformation of the azimuthally symmetric positive column into a rotating helix.[1,2] Figure 9 shows the helical nature of the column in a 90-deg stereo streak photograph in a dc He discharge. The traces show the variation of light intensity with time and radius as seen through a slit perpendicular to the axis of the tube. It can be seen that the phase differences between the traces is 90 deg and hence corresponds to a true helix. The rotational frequency of the helix can be seen to be approximately 60×10^3 rad/sec.

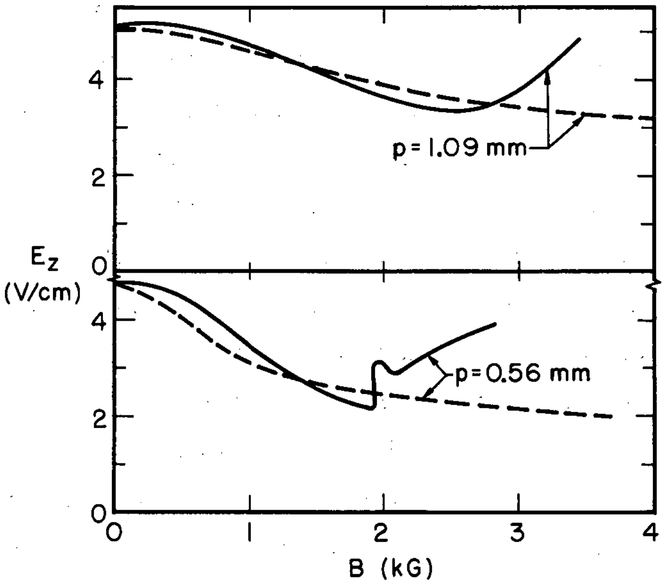

MU-27751

Fig. 8. E_z vs B; dc He gas, R = 0.9 cm, I = 200 mA.

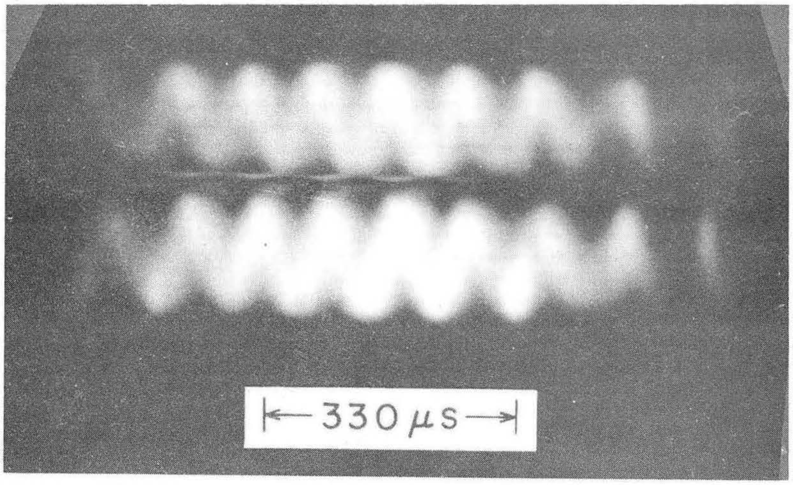

Fig. 9. Ninety-degree stereo streak photograph of helical instability in dc He discharge; $R = 2.75$ cm, $p = 0.23$ mm Hg, $B = 0.710$ kG.

ZN-2714

The dispersion relation from which Kadomtsev obtained the growth rate Im(ω) of the instability can also be solved for Re(ω), which is the rotational frequency of the instability. Solving for Re(ω) at $B = B_c$, we obtain the following approximate equation

$$\mathrm{Re}(\omega) \approx \frac{3\mu^{+} D_{-} (3.83/R)^{2}}{\mu_{-} (\Omega_{-} \tau_{-})} (0.6 + x^{2}), \qquad \text{(IV-1)}$$

where all the parameters are as defined in Chap. II. Evaluating this expression for the discharge parameters of Fig. 9, we find a value of approximately 65×10^{3} rad/sec. Rather good agreement is obtained, considering Eq. (IV-1) was derived from small-amplitude perturbation theory, while the experimental estimate was made from the fully developed helix. Photomultiplier signals have also shown the same frequency at the onset of the instability.

Electron-temperature measurements were made in He, Ne, and Ar dc discharges with both single-[41, 42] and double-probe[43] techniques. The measurements were taken with radially movable probes at B = 0 and at B slightly less than B_c. A complete discussion of these measurements is presented in Appendix B.

Electron temperatures at the critical magnetic field (actually just below it) must be known in order to calculate properly the onset of the instability in the Kadomtsev theory. Several experimenters who have compared their results with the Kadomtsev theory have used temperatures that were calculated from the electric field values at $B = B_c$,[3, 4] were calculated from the modified Schottky theory,[2] or have extrapolated previous experimental measurements from B = 0 to $B = B_c$.[6] The B_c calculated from the Kadomtsev theory is quite sensitive to the value of the electron temperature, since it is approximately directly proportional to the temperature. Paulikas and Pyle and von Gierke and Wöhler[5*] have obtained results in which the

---

[*] It should be noted that von Gierke and Wöhler used their measured values of electron temperatures in their calculations.

experimental critical magnetic fields have been roughly one-half that of the theoretical values calculated by means of the Kadomtsev theory. Incorrect electron temperatures (too low) have been proposed as a possible reason for this discrepancy.[1, 5] Table I compares some of the experimental temperatures obtained in our work with those calculated from the modified Schottky theory.[19] It can be seen that the experimental temperatures generally differ from the theoretical values by only approximately 10 to 20%. Although results of probe measurements in strong magnetic fields may be considered of dubious value, the good agreement with the modified Schottky theory tends to rule out the proposal that the discrepancy of theoretical and experimental critical magnetic fields (approximately a factor of two) could be caused by improper electron temperatures. Due to the good agreement obtained above, the modified Schottky theory will be used for consistency in the calculation of temperatures necessary in the comparison of the ac data with theory.

Discharges were also run with half-wave rectified (unidirectional) current. They were obtained by simply operating the discharge in the normal sinusoidal ac mode, and then turning off the heating current to one filament. This enabled us to see how large variations of the current with time, without actual current reversal, affected the value of the critical magnetic field. Streak photographs and E-vs-B curves were taken to determine the nature and onset of the instability under these conditions. At all but the highest frequencies, the critical magnetic field was the same as the dc value. That is, the heavily modulated current did not appreciably affect the instability in direct contrast with the ac (bidirectional) cases to be discussed later. At the higher frequencies ($\gtrsim$ 30 kc) a slight increase in the critical magnetic field was observed.

The helical structure of the column in a 50-kc half-wave rectified He discharge is visible in the streak photograph of Fig. 10. The magnetic field at which this photo was taken was approximately 900 G, which corresponds to the dc critical magnetic field.

Table I. Comparison of experimental and theoretical electron temperatures.

Gas	R (cm)	p (mm Hg)	B[a] (kG)	Single probe T_e (eV)	Double probe T_e (eV)	Mod. Schottky T_e (eV)
He	2.75	0.13	0.56	3.0	2.8	3.0
		0.44	0.91	3.0	2.7	2.8
		1.00	1.10	2.6	---	2.6
He	1.27	0.45	1.05	3.3	---	3.0
		0.80	2.20	3.0	---	2.7
Ne	2.75	0.30	1.45	2.0	1.9	2.2
		1.00	1.50	1.7	1.7	2.0
Ne	1.27	0.15	1.35	2.2	1.8	2.6
		0.90	3.00	1.7	1.5	2.1
Ar	2.75	0.15	1.10	1.2	1.3	1.3
		0.40	1.40	1.2	1.2	1.0
Ar	1.27	0.10	1.05	1.4	---	1.6
		0.30	1.50	1.4	---	1.4

[a] The magnetic field strengths chosen were slightly less than B_c.

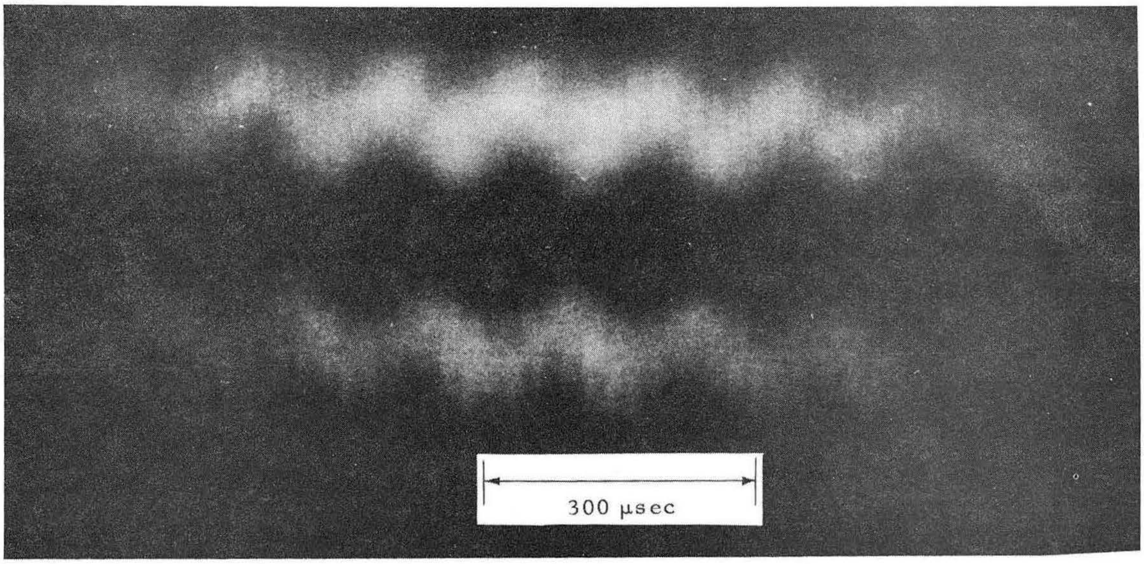

ZN-3790

Fig. 10. Ninety-degree stereo streak photo of half-wave rectified discharge; He gas, $R = 2.75$ cm, $p = 0.4$ mm Hg, $f = 50$ kc, $I = 1$-A sine wave, $B \approx 0.9 \text{ kG} \approx B_c$.

In contrast, a 50-kc ac discharge under the same operating conditions remained stable up to the limit of the magnetic field strength (7 kG). The rotational frequency of this helix can be seen to be approximately 45×10^3 rad/sec. This agrees with (to within better than 10%) the value obtained in the dc case by Paulikas and Pyle and also the value predicted by the Kadomtsev analysis as calculated by Eq. (IV-1).

The comparison between the dc and half-wave rectified results indicates that time-dependent fluctuations do not appreciably affect the properties of this instability, and therefore strengthens the validity of a comparison between the dc theory and the ac measurements.

B. Properties of the Alternating-Current Discharge at Zero Magnetic Field

Alternating-current glow discharges were investigated in H_2, D_2, He, Ne, and Ar in tubes of radius 1.27 and 2.75 cm. The discharges were run such that the current wave shape was either square or sinusoidal and oscillated about zero. However, the wave shapes deviated somewhat, depending on the gas, pressure, tube radius, and applied frequency. Figures 11 and 12 show typical oscilloscope traces, tube voltage, discharge current, electric field (voltage difference between the wall probes), and light intensity monitored by the photomultiplier tube in helium and neon discharges at zero magnetic field.

Note: All oscilloscope traces shown in this work are multiple sweeps; the time scale in the photographs runs from right to left.

Figure 11 presents oscilloscope photos of these properties for both sine-wave and square-wave current discharges operated at 2 kc. The electric field traces [Figs. 11(b) and 11(e)] can be seen to resemble the voltage traces since they are simply the difference voltage between the wall probes. The ringing in these signals was due to the ac amplifier. The P.M. traces [Figs. 11(c) and 11(f)] indicate that the light intensity closely follows the current. The nearly pure sine-wave and square-wave pulses of light indicate the absence of striations at this low pressure in He.

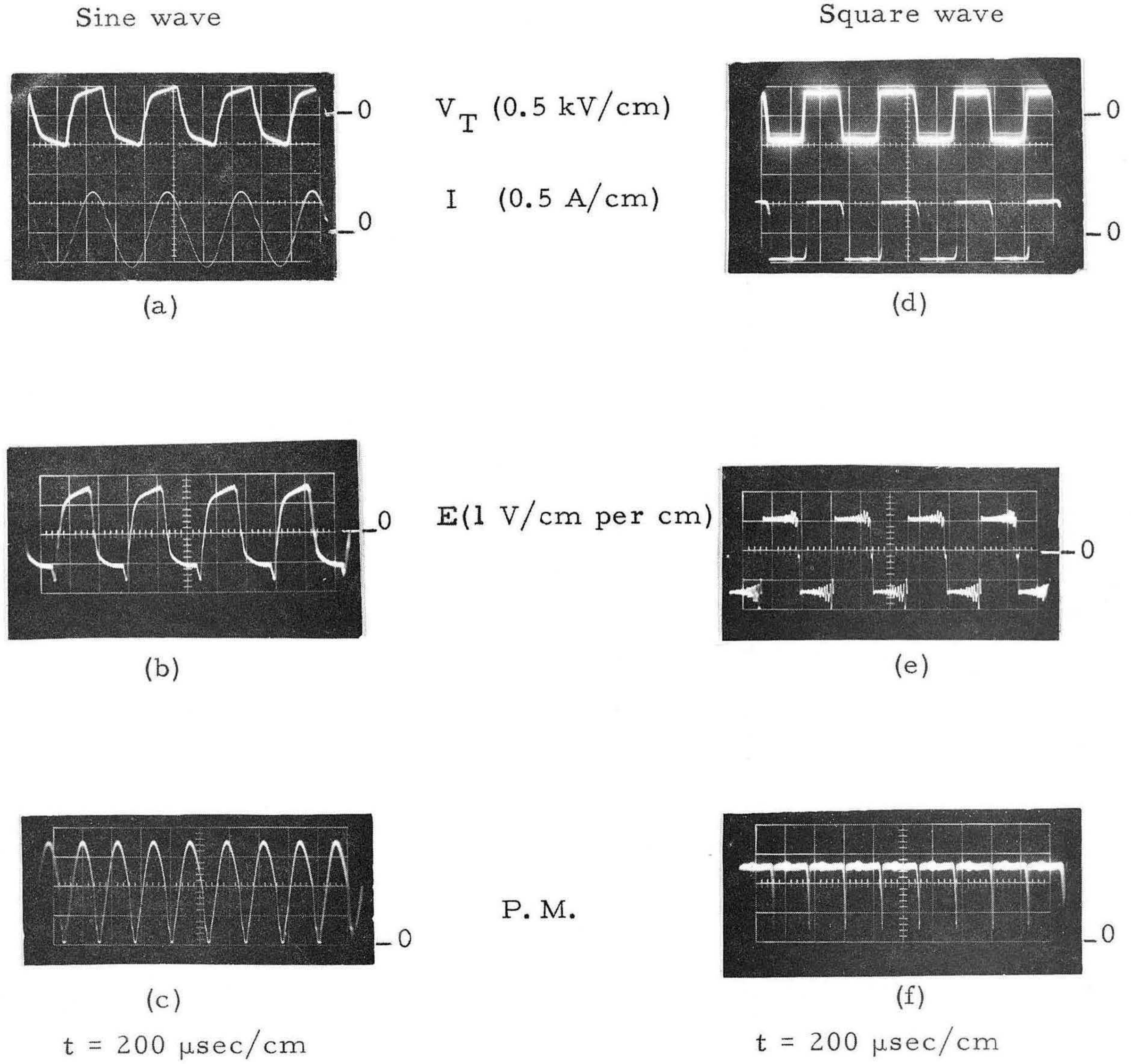

ZN-3746

Fig. 11. Tube voltage, current, electric field, and P. M. light intensity for He gas, R = 2.75 cm, p = 0.12 mm Hg, I = 500 mA, B = 0, f = 2 kc.

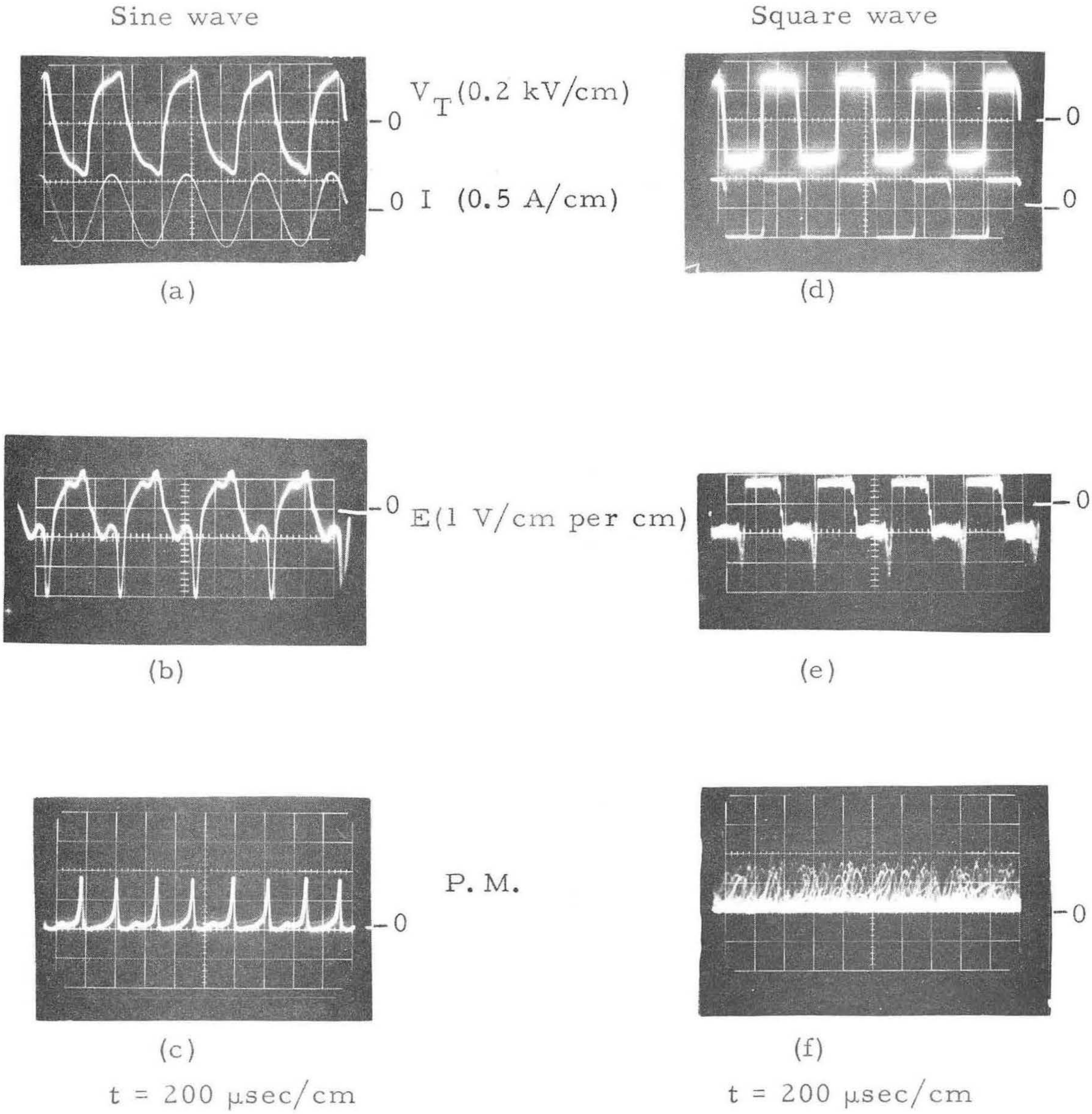

ZN-3747

Fig. 12. Tube voltage, current, electric field, and P. M. light intensity for Ne gas, R = 2.75 cm, p = 0.12 mm Hg, I = 500 mA, B = 0, f = 2 kc.

Figure 12 shows the sine-wave and square-wave characteristics for a Ne discharge under the same operating conditions. Again the electric field signals resemble their respective voltages, except for the large spikes. These are due to moving striations which are common in Ne, and can be seen in the P. M. traces [Figs. 12(c) and 12(f)]. Striations at the same velocity also appeared in a dc Ne discharge at the same pressure. The corresponding electric field signal contained the same frequency spikes as did the P. M. signal. The effect of the striations is discussed in Appendix D.

The relationship between the total voltage and discharge current is important in the comparison between the ac and the dc discharges. Figures 13 through 15 and those in Appendix C show typical oscilloscope traces of total voltage and discharge current in both square-wave and sine-wave discharges in the various gases employed.

It has been stated that if the ac discharges can be considered to behave in a quasi-dc fashion, then a comparison with the dc theory is valid. This can most easily be accomplished by the operation of a square-wave discharge. Figure 13 presents the current-voltage traces for a He discharge at several frequencies. The quasi-dc nature is exhibited at the lower frequencies. The peak voltage is identical with that obtained in a similar dc discharge. At 9 kc, limitations of the square-wave amplifier rise time became significant, and the voltage and current "rounded off" slightly. The rounding of the voltage traces on the oscilloscope photos was also partially due to a non-negligible (at frequencies greater than 10 kc) RC time constant of the voltage divider and its circuitry. This tended to filter out the high-frequency components of the square-wave signals. Hence, the actual voltages were somewhat more square than displayed on the oscilloscope, at frequencies greater than 10 kc.

Table II compares the peak voltage observed in typical square-wave discharges at a current reversal frequency of 1 kc with the total voltage observed in similar dc discharges. This was done for $B = 0$ and for B slightly less than B_c. One kilocycle was chosen because the

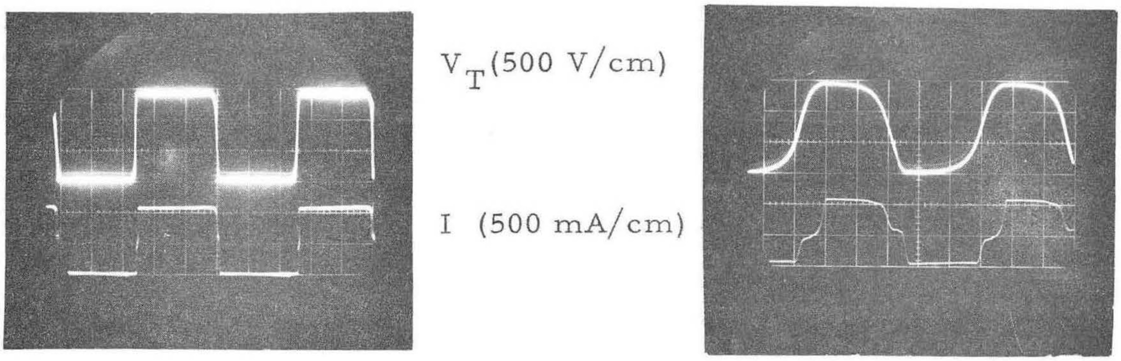

(a)
f_{osc} = 1 kc
t = 200 μsec/cm

(c)
f_{osc} = 9 kc
t = 20 μsec/cm

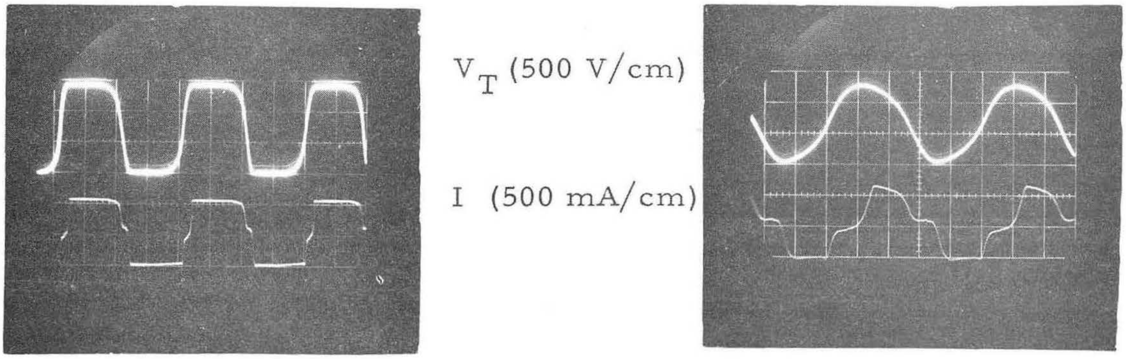

(b)
f_{osc} = 5 kc
t = 50 μsec/cm

(d)
f_{osc} = 20 kc
t = 10 μsec/cm

ZN-3748

Fig. 13. Comparison of square-wave voltage and current vs oscillator frequency for He gas, R = 1.27 cm, p = 0.12 mm Hg, I = 500 mA, B = 0, square wave.

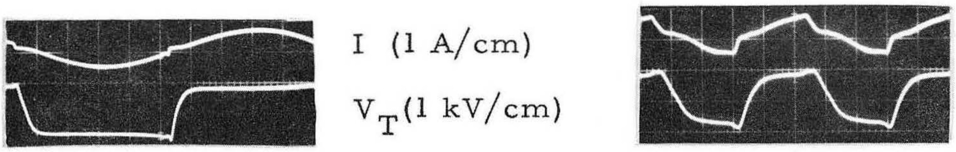

(a)

f_{osc} = 1 kc

t = 100 μsec/cm

(c)

f_{osc} = 10 kc

t = 20 μsec/cm

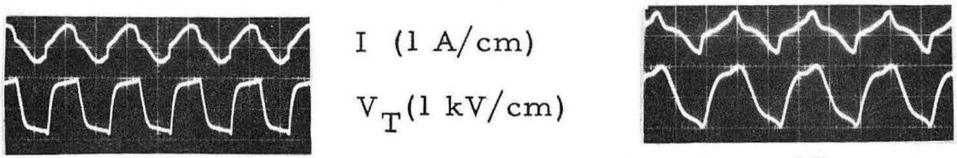

(b)

f_{osc} = 5 kc

t = 100 μsec/cm

(d)

f_{osc} = 20 kc

t = 20 μsec/cm

ZN-3749

Fig. 14. Comparison of sine-wave voltage and current vs oscillator frequency for He gas, p = 0.12 mm Hg, B = 0, R = 1.27 cm, I = 500 mA, sine wave.

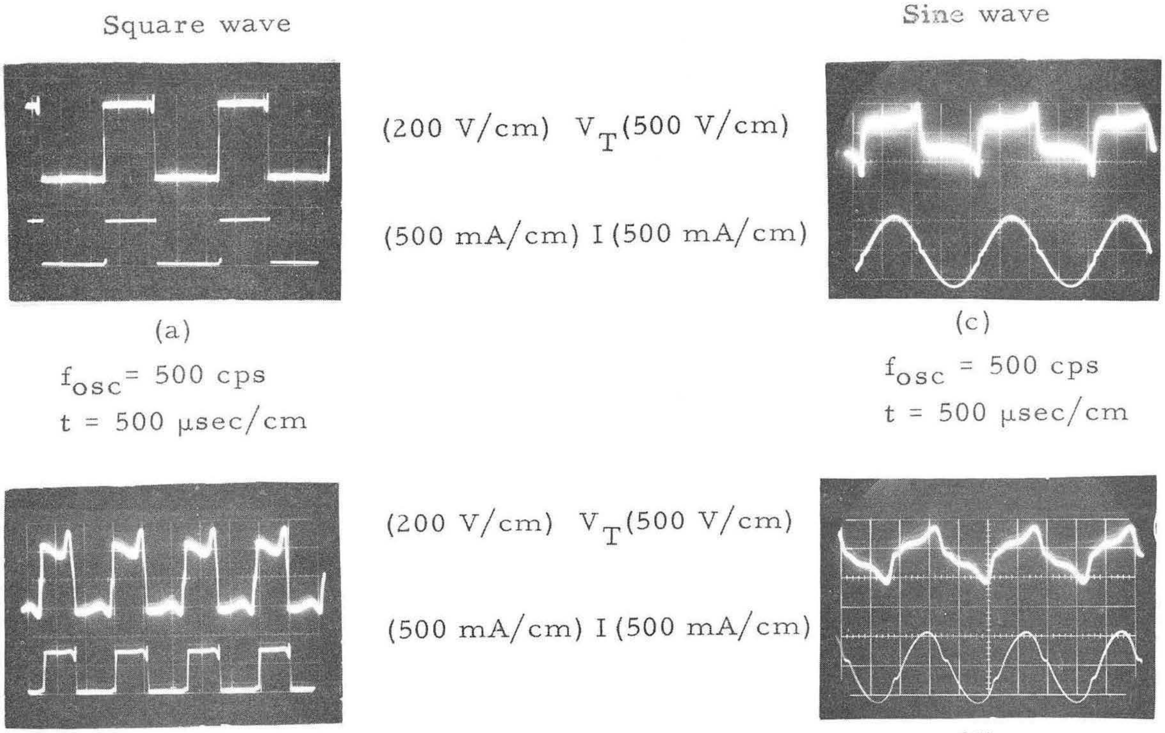

(a)
f_{osc} = 500 cps
t = 500 μsec/cm

(c)
f_{osc} = 500 cps
t = 500 μsec/cm

(b)
f_{osc} = 8 kc
t = 50 μsec/cm

(d)
f_{osc} = 3 kc
t = 100 μsec/cm

ZN-3750

Fig. 15. Comparison of sine-wave and square-wave voltage and current vs oscillator frequency for Ar gas, R = 1.27 cm, p = 0.18 mm Hg, B = 0.

Table II. Comparison of square-wave and direct-current discharge voltage.

Gas	R (cm)	p (mm Hg)	B (kG)	Square wave V_T (lkc)	DC V_T
He	2.75	0.13	0.0	425 ± 10[a]	420
			0.55	260 ± 10	260
		0.60	0.0	480 ± 10	475
			1.0	415 ± 10	410
	1.27	0.13	0.0	700 ± 20	700
			0.77	320 ± 20	310
		0.80	0.0	870 ± 20	860
			2.10	670 ± 20	660
Ne	2.75	0.60	0.0	245 ± 20	250
			1.20	160 ± 20	150
	1.27	0.16	0.0	460 ± 20	450
			1.19	220 ± 20	210
Ar	2.75	0.16	0.0	130 ± 10	140
			0.90	70 ± 10	70
	1.27	0.40	0.0	220 ± 20	220
			2.0	95 ± 20	100

[a] Deviation (±) was determined from the estimated accuracy of reading the voltage from the oscilloscope.

alternating voltages were quite square, hence an accurate peak voltage could be determined. The comparison shows the voltages to be identical within the accuracy of the measurements. Peak electric fields, determined by measuring the voltage across two probes separated by a known distance, were also compared with their dc counterparts. In those cases where the ac electric fields were measurable,[*] agreement to within approximately 10% was obtained. These results suggest that the square-wave discharges can be considered as quasi-dc up to fairly high frequencies (for example, f = 40 kc in He at low pressure).

Sine-wave discharges differ from square in that the current is continuously changing with time, not just at the point of reversal as in the square-wave case. However, it can be seen that these discharges also have a quasi-dc character. A characteristic of a normal dc glow discharge is that, once the equilibrium voltage has been established, a further increase in current does not affect the magnitude of the voltage across the discharge.[17] Figure 14 presents voltage and current wave shapes for a sinusoidal He discharge at several frequencies. At the lower frequencies the voltage can be seen to have reached a plateau and remained constant as the current continued to change with time. Even at an oscillator frequency of 10 kc the voltage tended to remain flat while the current changed. The voltage of the plateaus was also verified to equal the operating voltage across a similar dc discharge. The corresponding electric fields also agreed with the dc values. Hence, this behavior corresponds to that of a quasi-dc discharge. However, another effect was visible in the sine-wave discharges under different conditions. At an oscillator frequency of only 3 kc in Ar, for instance [Fig. 15(d)], the voltage can be seen to decrease rapidly after reaching a peak rather than remaining constant. This effect was more pronounced at higher frequencies, at higher pressure, in the larger tube, and in the discharges of low ion mobility. Hence, it may be related to the

---

[*] Problems in the determination of the ac electric fields are discussed in Subsec. IV-C and Appendix D.

drift time of ions to the walls. Under these conditions the quasi-dc nature of the discharge is questionable. However, it should be recalled that the time-dependent half-wave rectified-current discharges yielded the same values of B_c as the dc discharges. Hence, we also compare the higher frequency sinusoidal discharges to the dc theory in Subsec. IV-E.

C. Determination of the Critical Magnetic Field

The critical magnetic field at which the instability occurs was measured by three different means: the variation of the axial electric field vs applied magnetic field, the variation of the total voltage across the discharge vs applied magnetic field, and the variation of the time-averaged light intensity vs applied magnetic field. All three methods were not always employed simultaneously, but when they were, exact agreement as to the onset of the instability was obtained.

The first method involved the measurement of the differential voltage between two wall probes spaced a known distance apart. This determined the value of the axial electric field in the positive column. This signal was then plotted as a function of the magnetic field strength and frequency on the X-Y recorder. An example of a typical set of curves is shown in Fig. 16. The amplitudes of the signals are given in arbitrary units and are separated in the vertical direction in order to show clearly the structure of the curves. The frequencies (f) indicated in the figure (and those to follow) refer to electric-field reversal frequency; that is, they are twice the oscillator output frequency (f_{osc}) since the current reverses every half cycle.

The accurate determination of the value of the electric field presented quite a problem in the ac discharges. This is discussed in detail in Appendix D. Due to these complications another similar yet simpler method of detecting the critical magnetic field was employed. The total voltage across the tube (the largest part of which is due to the positive column in long discharge tubes with hot cathodes) was plotted vs magnetic field on the X-Y recorder. A typical example of one of these curves is presented in Fig. 17. A complete set of these curves for all the gases appears in Appendix D.

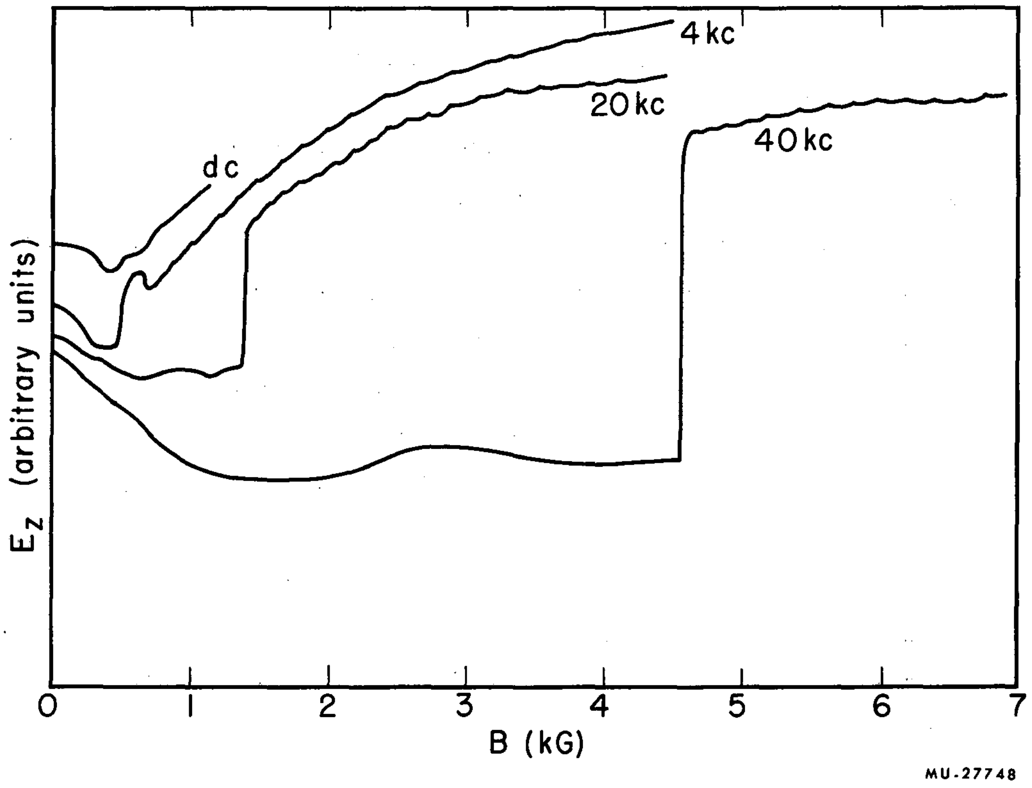

Fig. 16. E_z vs B; He gas, R = 2.75 cm, p = 0.12 mm Hg, I = 500 mA, sine wave.

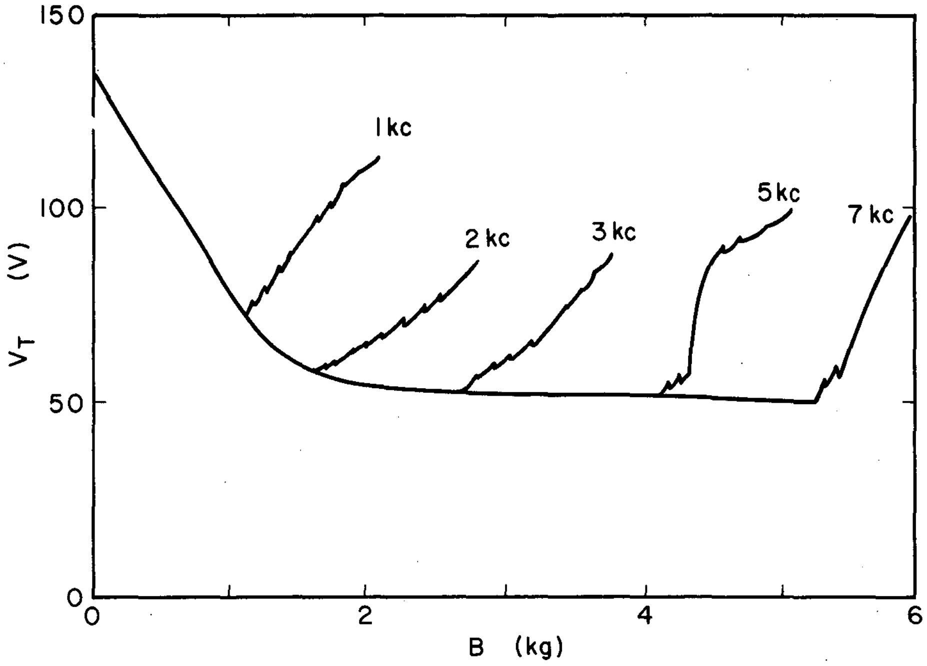

MU-30671

Fig. 17. V_T vs B; Ar gas, R = 2.75 cm, p = 0.16 mm Hg, I = 500 mA, square wave.

The final method for detecting the critical magnetic field involved the recording of the time-averaged light intensity from the center of the plasma by means of a P. M. tube. This data was also plotted on the X-Y recorder as a function of magnetic field strength. An example of this is presented in Fig. 18 and shows its similarity to the other two methods. The sharp increase in the amplitude of the light is due to the increase in the axial electric field and electron temperature, which is necessary to maintain the discharge in the unstable state due to the increased loss of plasma to the walls.

From these results it can be seen that the onset of the instability is indeed suppressed as the electric-field reversal frequency is increased. It was shown in Sec. A of this chapter that suppression actually requires a current reversal and not just a superimposed ac component of a dc current. These qualitative results agree with the Kadomtsev model for instability. A quantitative comparison appears in a later section (IV-E).

The dependence of the critical magnetic field on the magnitude of the current was also investigated. The value of B_c increased slightly with increasing discharge current, just as it did in the dc case.[1, 2] Figure 19 shows this effect in a He discharge and gives some idea as to its magnitude. It is somewhat more pronounced at higher pressures and in gases such as Ar and Ne. Under conditions of high current and pressure, cumulative ionization (rather than single-stage ionization) due to metastable states is likely to be more prevalent than at lower currents and pressures.[44] Consequently, due to this more efficient form of ionization, the axial electric field is reduced. According to Kadomtsev's model a decrease in the electric field would be reflected in an increase in B_c, which is seen in Fig. 19.

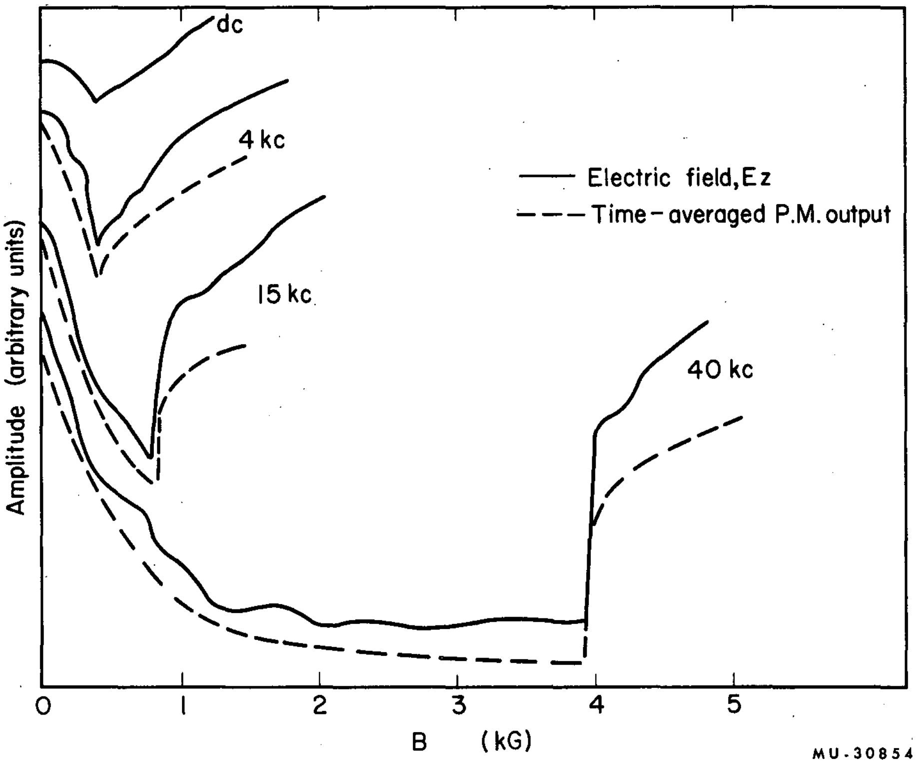

Fig. 18. E_z and light intensity vs B; He gas, R = 2.75 cm, p = 0.13 mm Hg, I = 500 mA, sine wave.

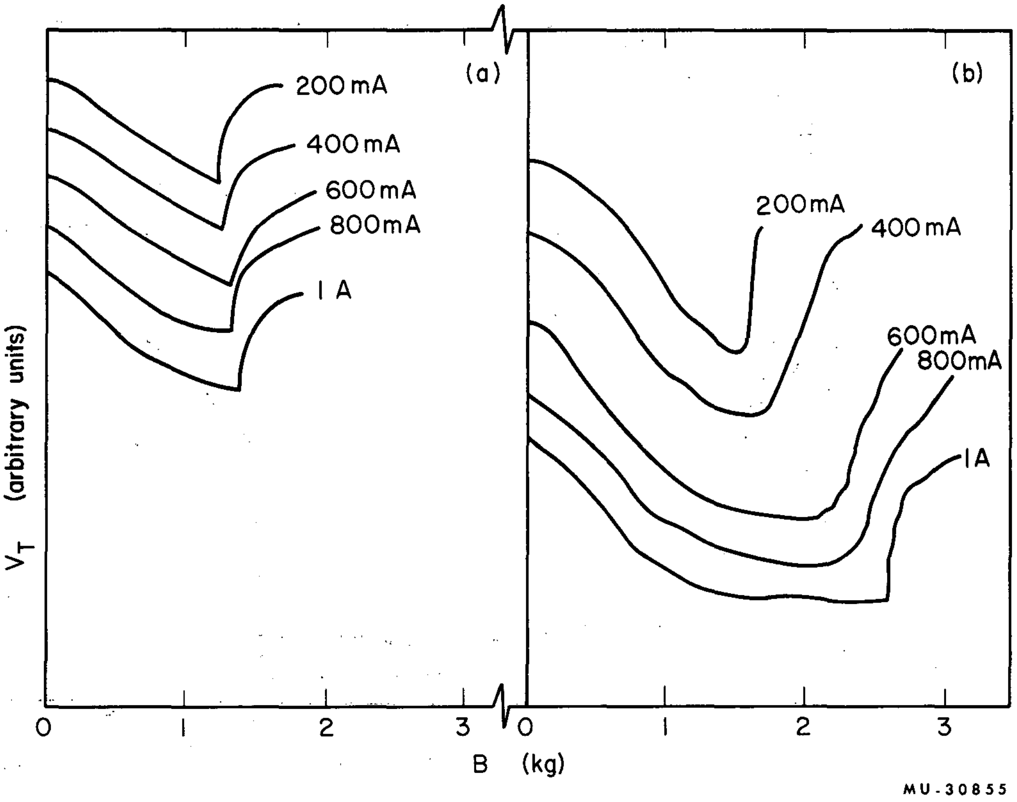

Fig. 19. B_c vs I.
(a) He gas, R = 2.75 cm, p = 0.15 mm Hg, f = 20 kc, square wave.
(b) Ar gas, R = 2.75 cm, p = 0.15 mm Hg, f = 2 kc, square wave.

D. Nature of the Instability

A rotating-mirror streak camera and a P. M. optically monitored the column in the ac discharges. The recording of the P. M. traces was straightforward, but streak photography was not practical in all gases.

Helium was found to be the most useful of the gases employed. It was the brightest, and was usually free from striations at pressures below about 0.4 mm Hg. Neon was also bright enough, but was almost always complicated with striations. Argon just did not give off sufficient light intensity for good streak photographs. Hydrogen and deuterium required such high operating voltages that the maximum current available from the power supplies was limited to around 1 A. Because of this the streak photographs taken were too faint to be reproduced in this text, although careful scrutiny revealed the helical nature of the column at the onset of the instability.

Ninety-degree stereo streak photographs together with the corresponding P. M. output traces are shown for a sinusoidal He discharge. The appearance of the three streak photos ($B = 0$, $B \approx B_c$, $B >> B_c$) in Figs. 20, 21, and 22 and their accompanying P. M. traces can be explained thusly: In Fig. 20 at $B = 0$ the sinusoidal discharge was operating in an unstriated region. Each light pulse corresponds to one half-cycle of the current (1.5 kc), hence the period for each pulse was roughly 300 μsec. The sinusoidal character of the light intensity is clearly seen in the P. M. trace and can be seen in the streak photo by the gradual fading of the light intensity as the current reverses direction. As the magnetic field was increased, the reduction in the electric field, and consequently the electron temperature, caused the light intensity from the plasma to drop markedly. Thus, no streak photos are presented for this region.

As the critical magnetic field was reached, the plasma became unstable and transformed into a rotating helix. The increased loss of particles to the wall of the tube caused the electric field and electron temperature to rise sharply and photography was again possible.

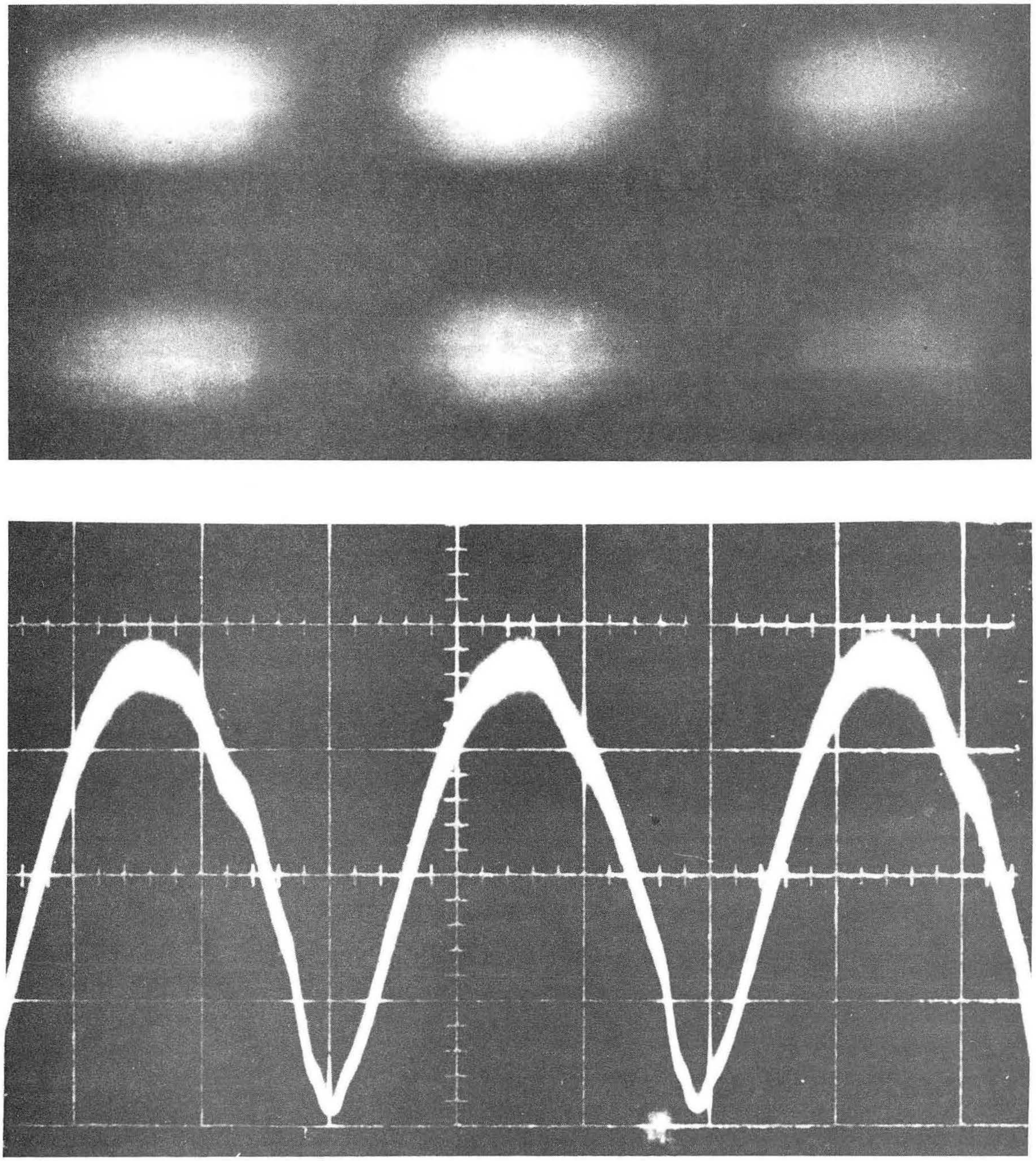

ZN-3791

Fig. 20. Ninety-degree stereo streak photograph and corresponding P. M. trace of an ac He discharge at $B = 0$; He gas, $R = 2.75$ cm, $p = 0.12$ mm Hg, $I = 1$ A, $B = 0$, $f \approx 3$ kc, sine wave.

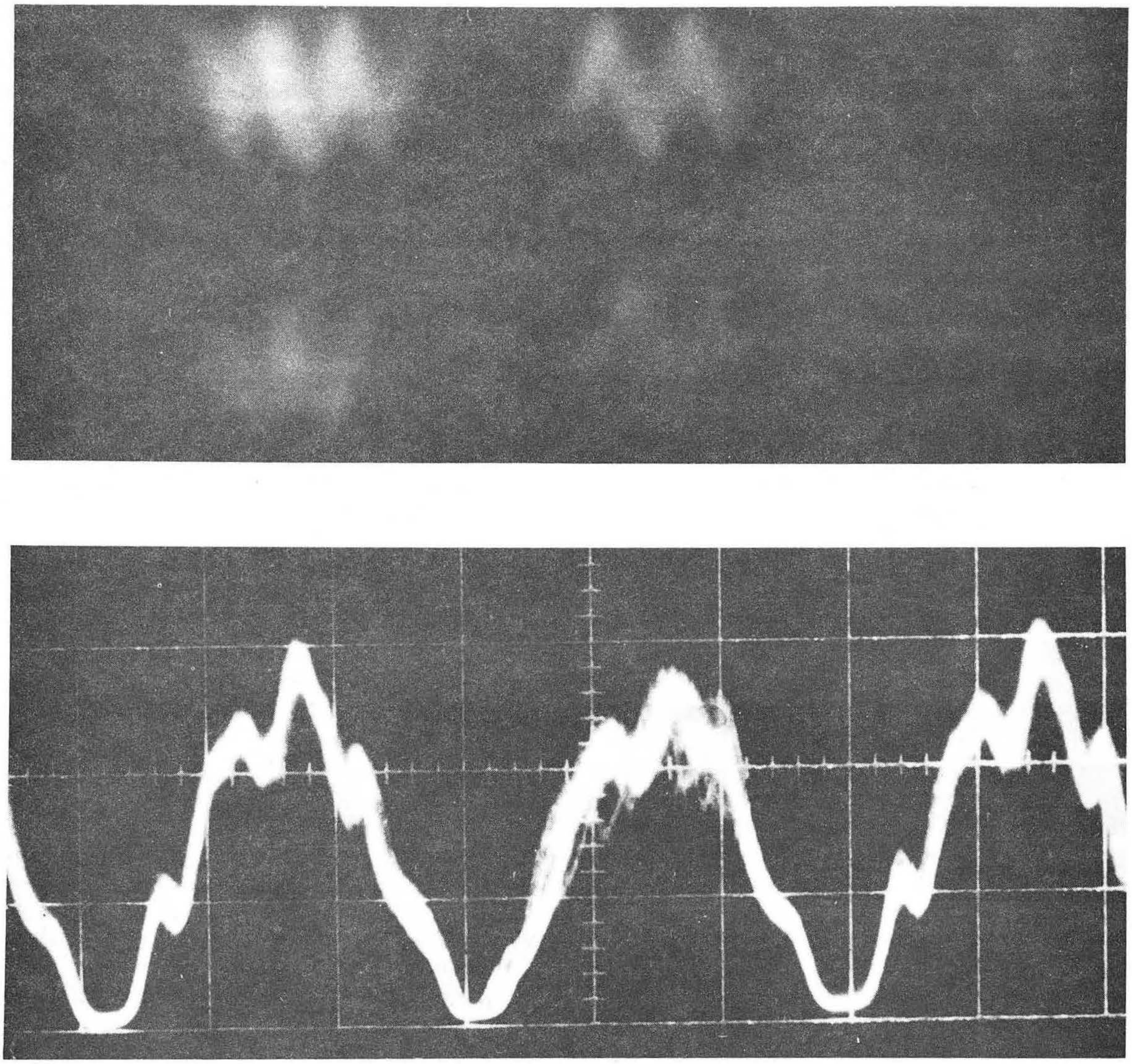

ZN-3792

Fig. 21. Ninety-degree stereo streak photograph and corresponding P. M. trace of an ac He discharge at $B \approx B_c$; He gas, $R = 2.75$ cm, $p = 0.12$ mm Hg, $I = 1$ A, $B = 0.45$ kG, $f \approx 3$ kc, sine wave.

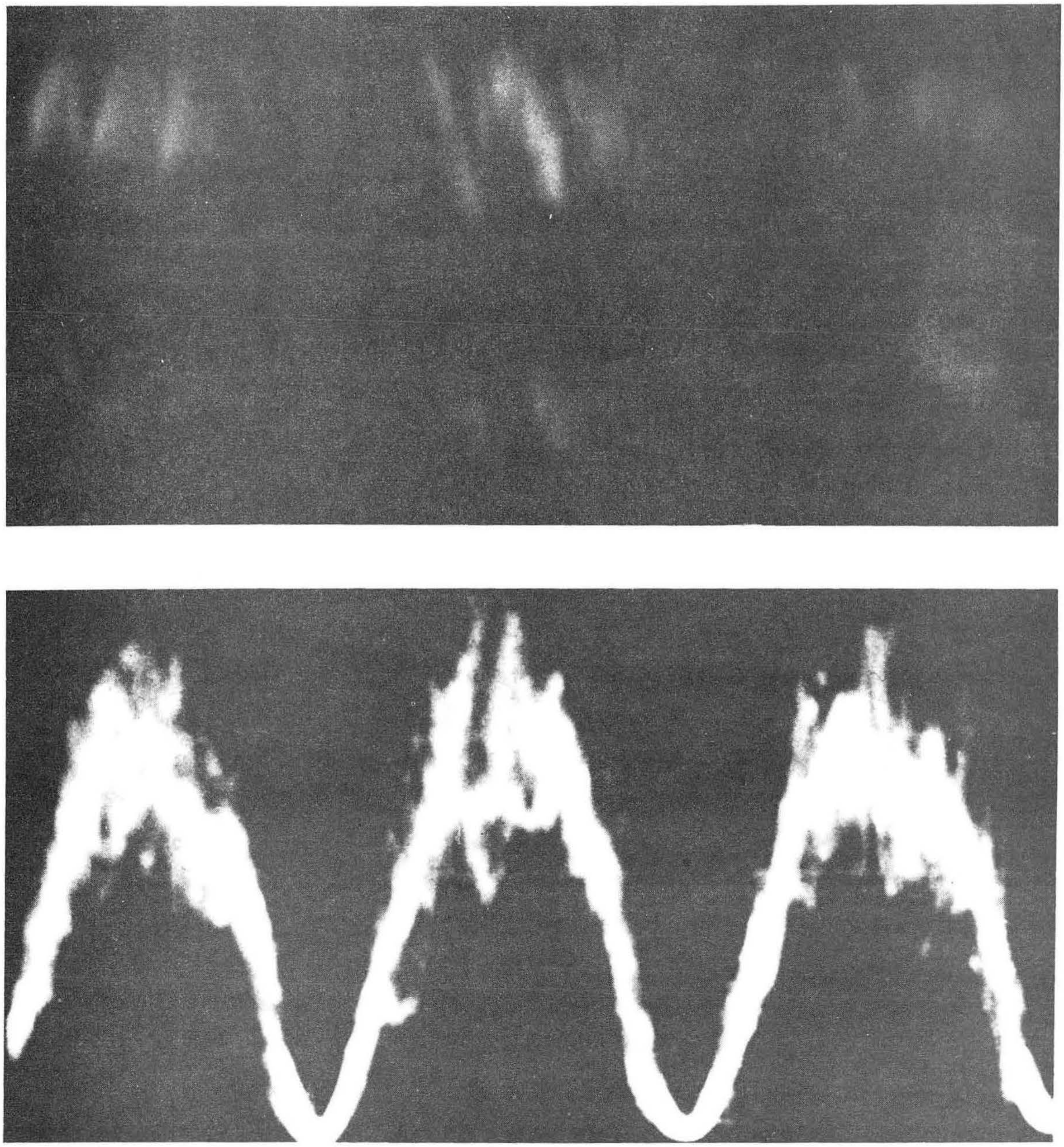

ZN-3793

Fig. 22. Ninety-degree stereo streak photograph and corresponding P. M. trace of an ac He discharge at $B > B_c$; He gas, $R = 2.75$ cm, $p = 0.12$ mm Hg, $I = 1$ A, $B = 2.4$ kG, $f \approx 3$ kc, sine wave.

The spirals can be clearly seen during each half-cycle on the streak photograph in Fig. 21. The undulations on the P. M. trace correspond well to the streak photo. From these photos the rotational frequency of the spiral is seen to be roughly 6×10^4 rad/sec. Evaluating the rotational frequency from Eq. (IV-1), we obtain a value of approximately 7×10^4 rad/sec. Again good agreement is obtained from the dc perturbation analysis.

At magnetic fields much higher than the critical field one finds the plasma in a form of turbulence. This can be seen by the hash on the P. M. trace and likewise on the streak photo. This effect can also be explained by the Kadomtsev theory. The helix that was formed at the onset of the instability corresponded to the m = 1 solution of the stability problem. Detailed calculations of higher m values by use of Kadomtsev's theory are given in Subsec. IV-E. Essentially, as the magnetic field was increased higher m-value modes became unstable. Thus at $B >> B_c$ we would expect to find a superposition of many m modes. This would then be represented by noise on the P. M. and a turbulent plasma in the streak photograph, which is exactly what was observed in Fig. 22.

E. Comparison Between Theory and Experiment

In order to verify that the onset of the instability in the ac discharges will be suppressed until the growth rate exceeds the current reversal frequency, we compare the calculated growth rate vs magnetic field with the experimental current reversal frequency vs its critical magnetic field. These comparisons appear in Figs. 23 through 35 and in Appendix E for all the gases and tube radii employed at several pressures (reduced to 0 °C) for sine-wave and square-wave currents.

<u>Note:</u> In Figs. 23 through 35 the Kadomtsev and Nedospasov[6] curves are labeled K-N, and the Johnson and Jerde[9] curves are labeled J-J. The m values appear on the curves. The experimental points are indicated by dots.

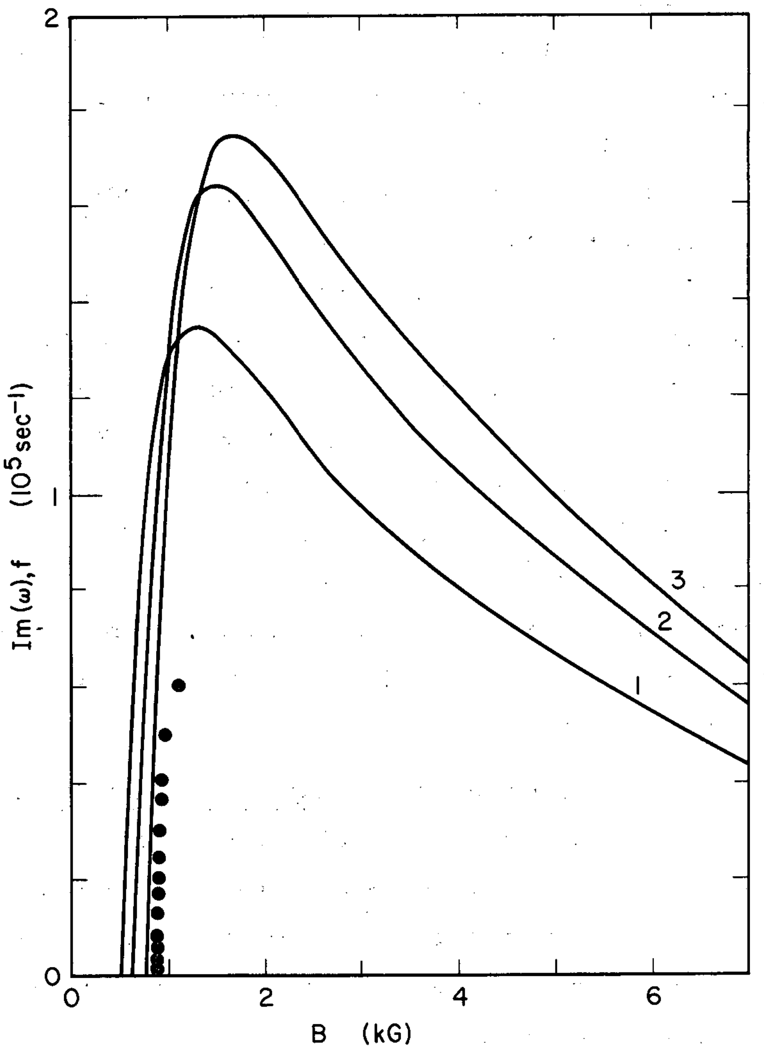

MU-30856

Fig. 23(a). Johnson and Jerde[9] curves for Im(ω), f vs B, with He$^+$, p = 0.22 mm Hg, R = 1.27 cm, I = 500 mA, square wave.

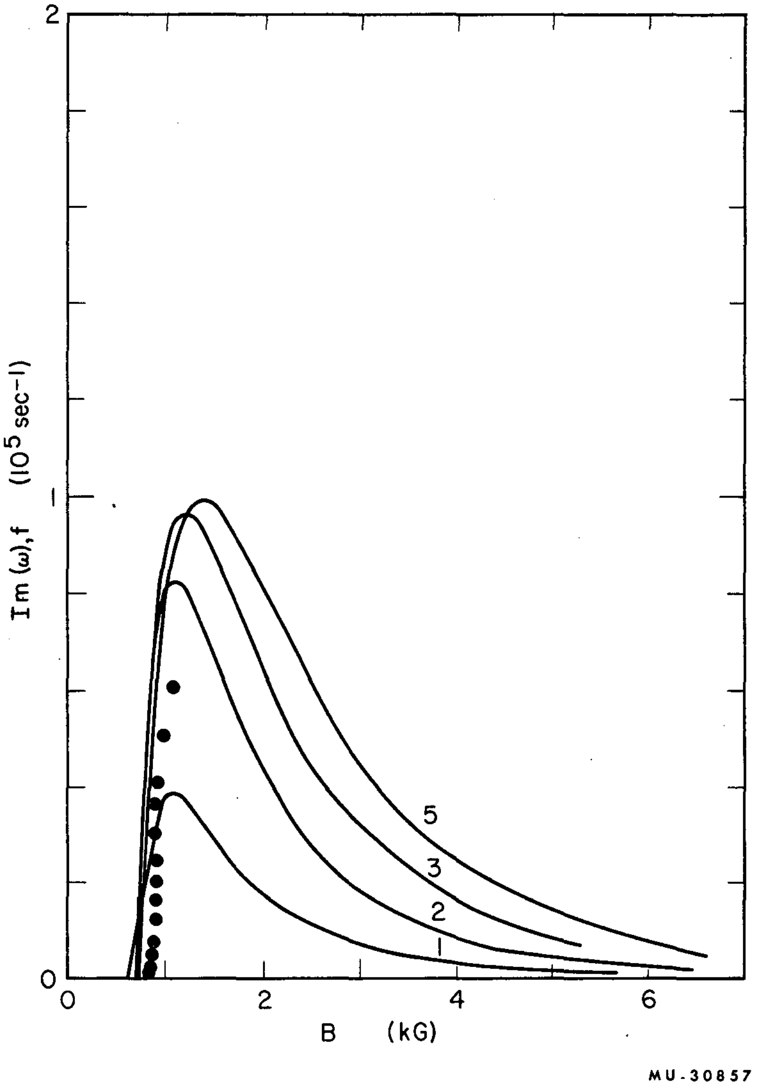

Fig. 23(b). Kadomtsev and Nedospasov[6] curves for Im(ω), f vs B, with He^+, p = 0.22 mm Hg, R = 1.27 cm, I = 500 mA, square wave.

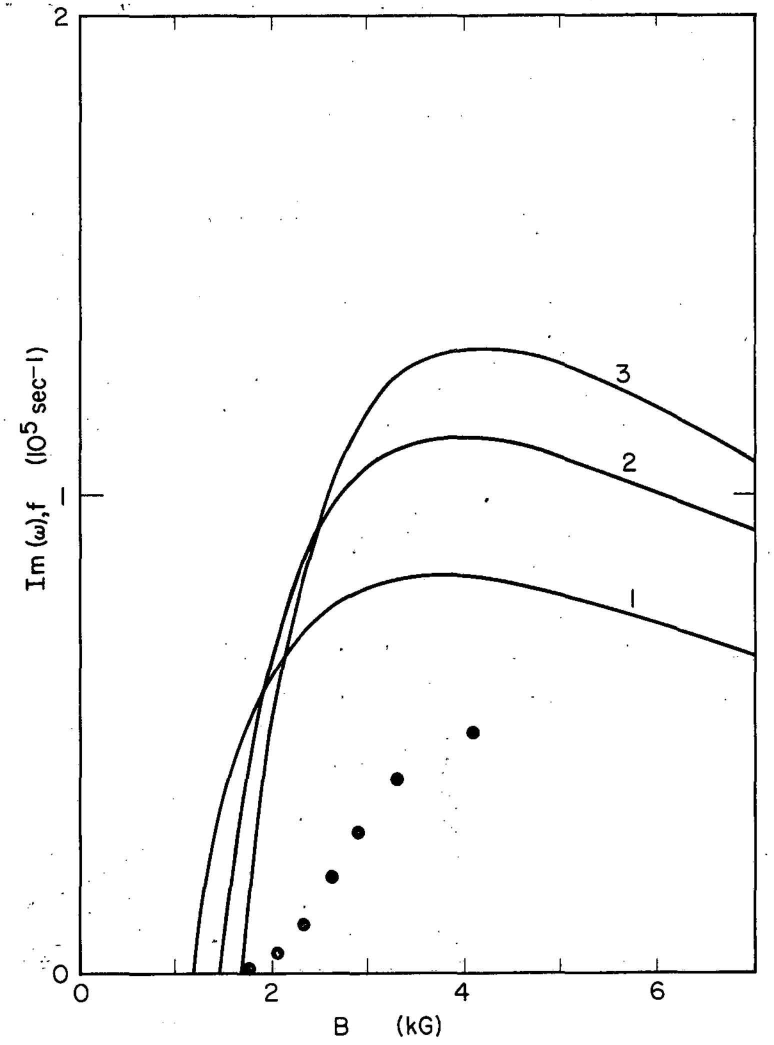

MU-30858

Fig. 24(a). Johnson and Jerde[9] curves for Im(ω), f vs B, with He^+, p = 0.8 mm Hg, R = 1.27 cm, I = 500 mA, square wave.

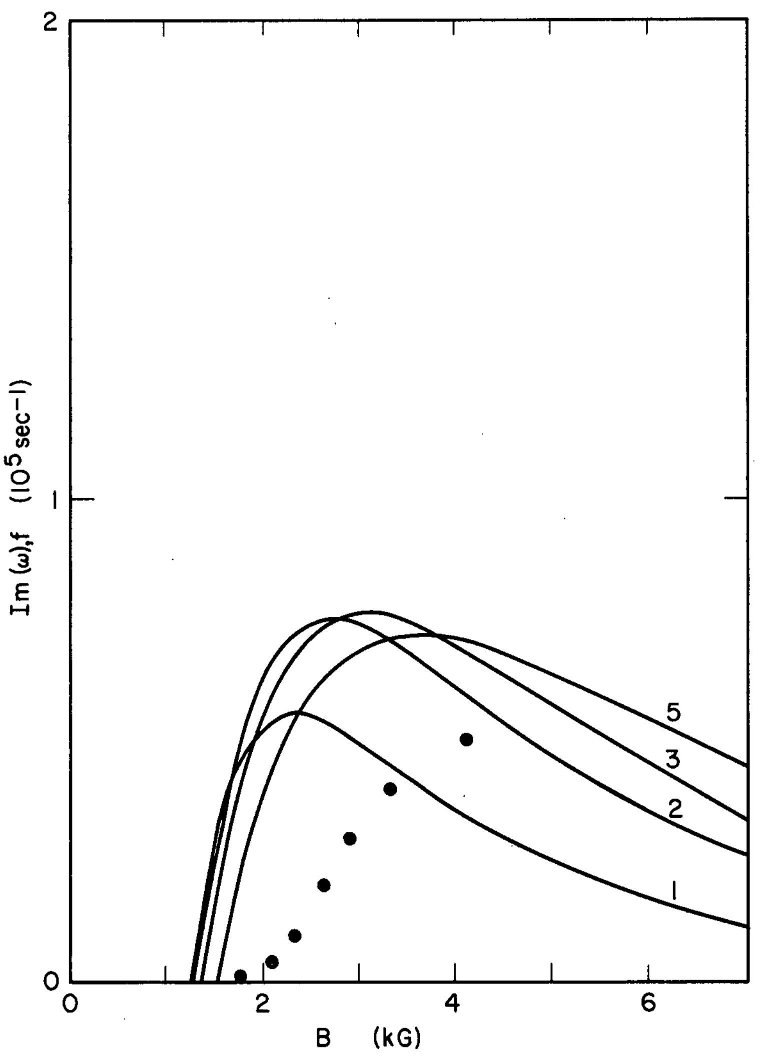

MU-30859

Fig. 24(b). Kadomtsev and Nedospasov[6] curves for Im(ω), f vs B, with He^+, $\bar{p}$ = 0.8 mm Hg, R = 1.27 cm, I = 500 mA, square wave.

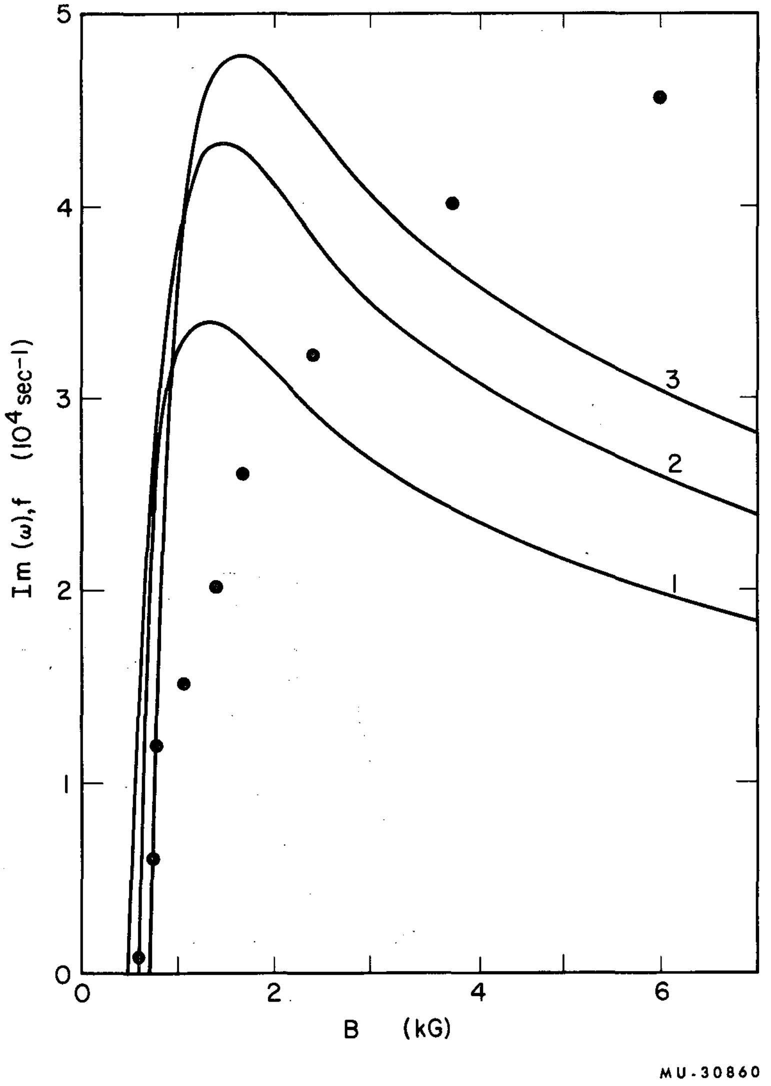

Fig. 25(a). Johnson and Jerde[9] curves for Im(ω), f vs B, with He$^+$, p = 0.22 mm Hg, R = 2.75 cm, I = 500 mA, square wave.

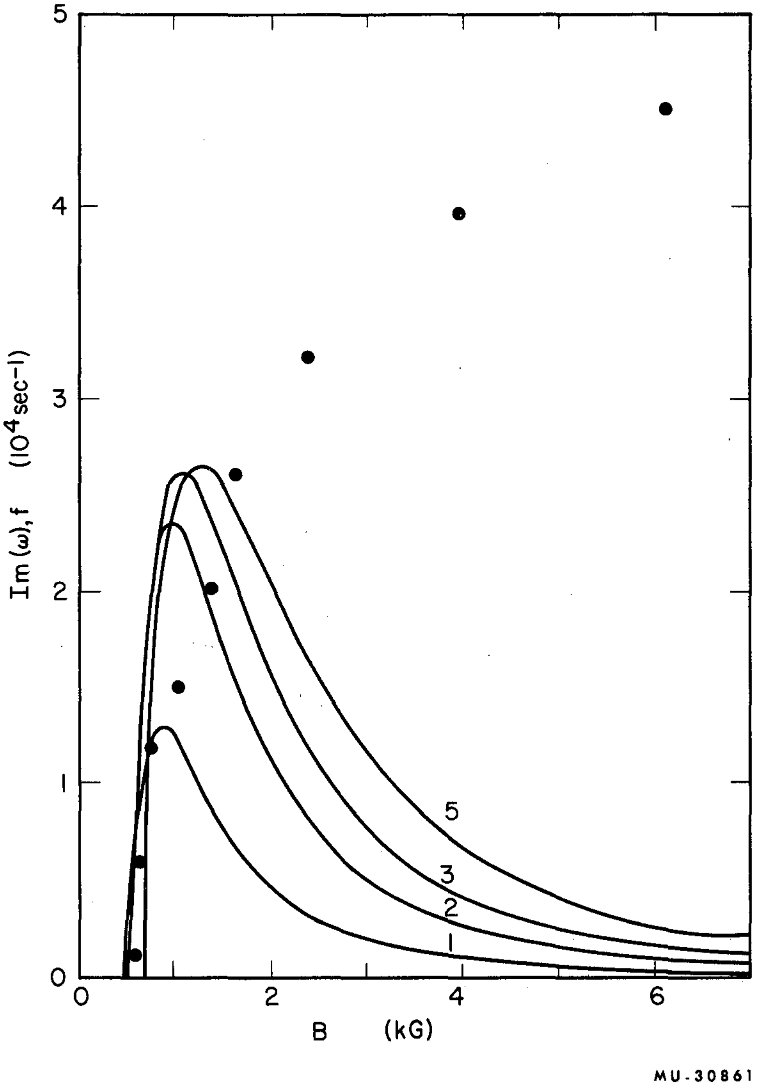

Fig. 25(b). Kadomtsev and Nedospasov[6] curves for Im(ω), f vs B, with He$^+$, p = 0.22 mm Hg, R = 2.75 cm, I = 500 mA, square wave.

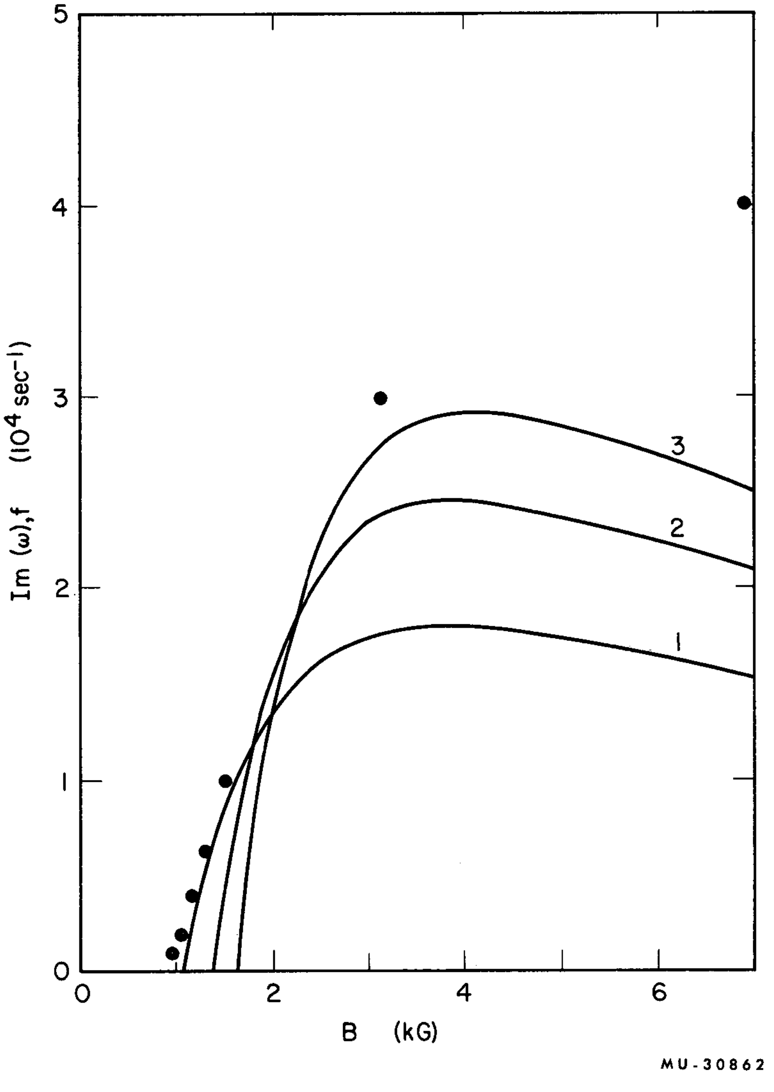

Fig. 26(a). Johnson and Jerde[9] curves for Im(ω), f vs B, with He^+, p = 0.8 mm Hg, R = 2.75 cm, I = 500 mA, square wave.

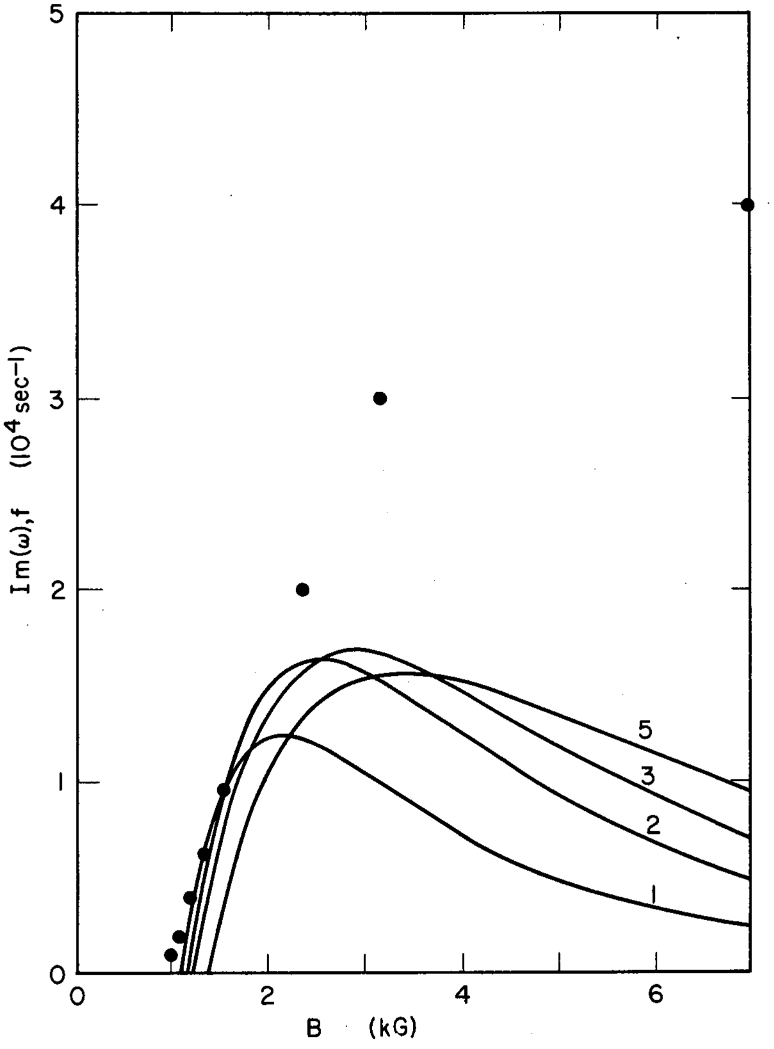

MU-30863

Fig. 26(b). Kadomtsev and Nedospasov curves for Im(ω), f vs B, with He^+, p = 0.8 mm Hg, R = 2.75 cm, I = 500 mA, square wave.

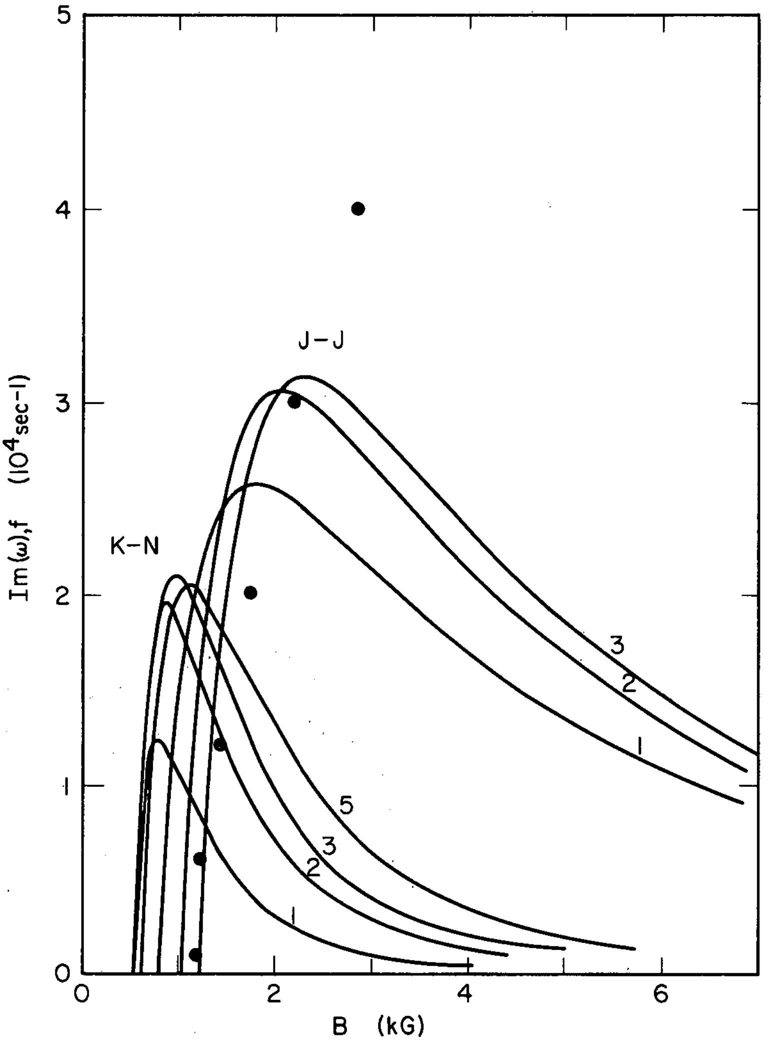

MU-30864

Fig. 27. Im(ω), f vs B, with Ne^+, p = 0.18 mm Hg, R = 1.27 cm, I = 400 mA, square wave.

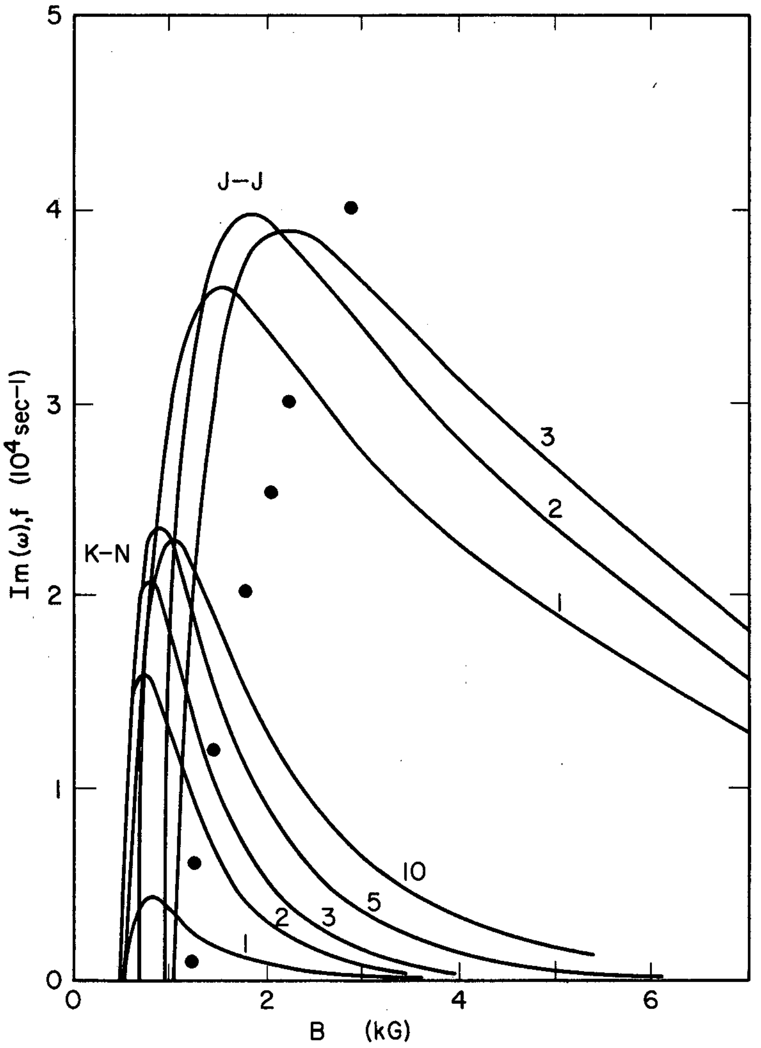

MU-30865

Fig. 28. Im(ω), f vs B, with Ne_2^+, p = 0.18 mm Hg, R = 1.27 cm, I = 400 mA, square wave.

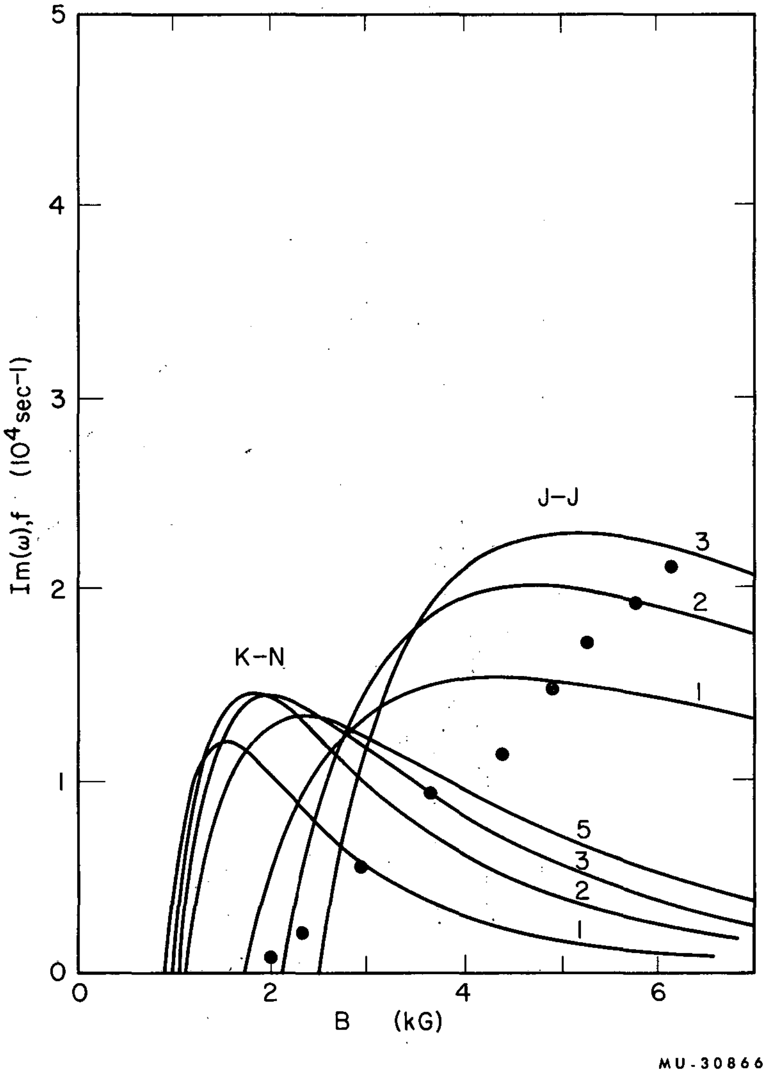

Fig. 29. Im(ω), f vs B, with Ne^{+}, p = 0.50 mm Hg, R = 1.27 cm, I = 400 mA, square wave.

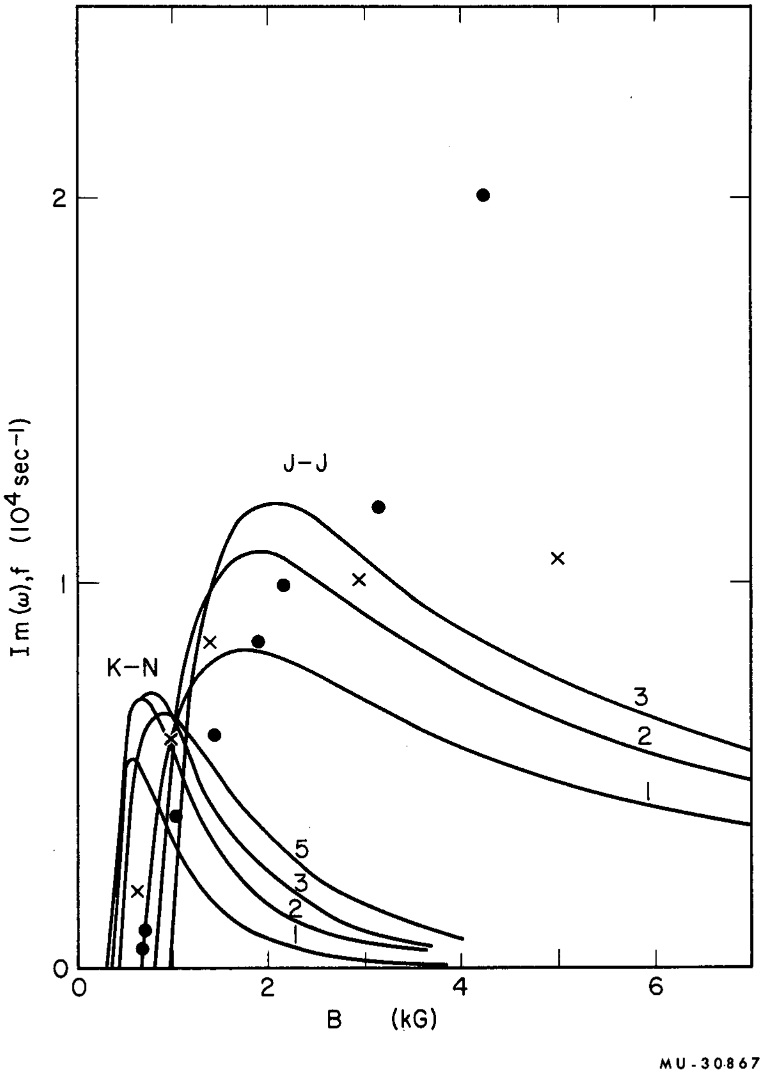

Fig. 30. Im(ω), f vs B, with Ne$^+$, p = 0.18 mm Hg, R = 2.75 cm, I = 500 mA, square wave. The ×'s represent data taken several months earlier in a different tube (same radius).

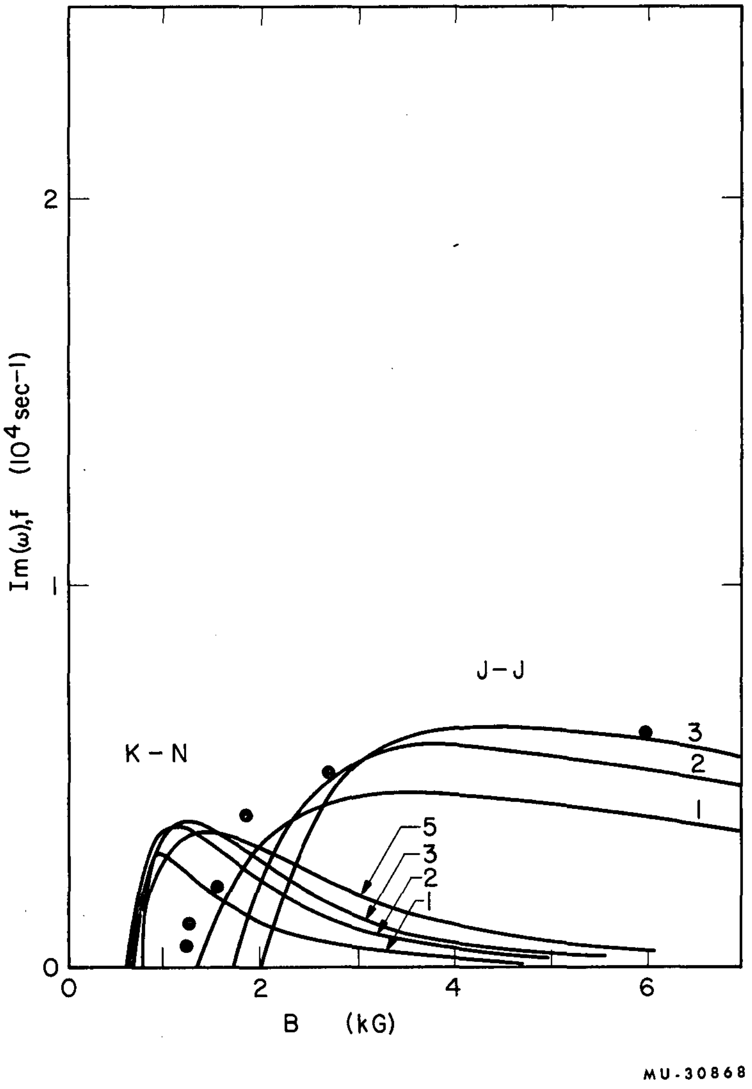

Fig. 31. Im(ω), f vs B, with Ne_2^+, p = 0.52 mm Hg, R = 2.75 cm, I = 500 mA, square wave.

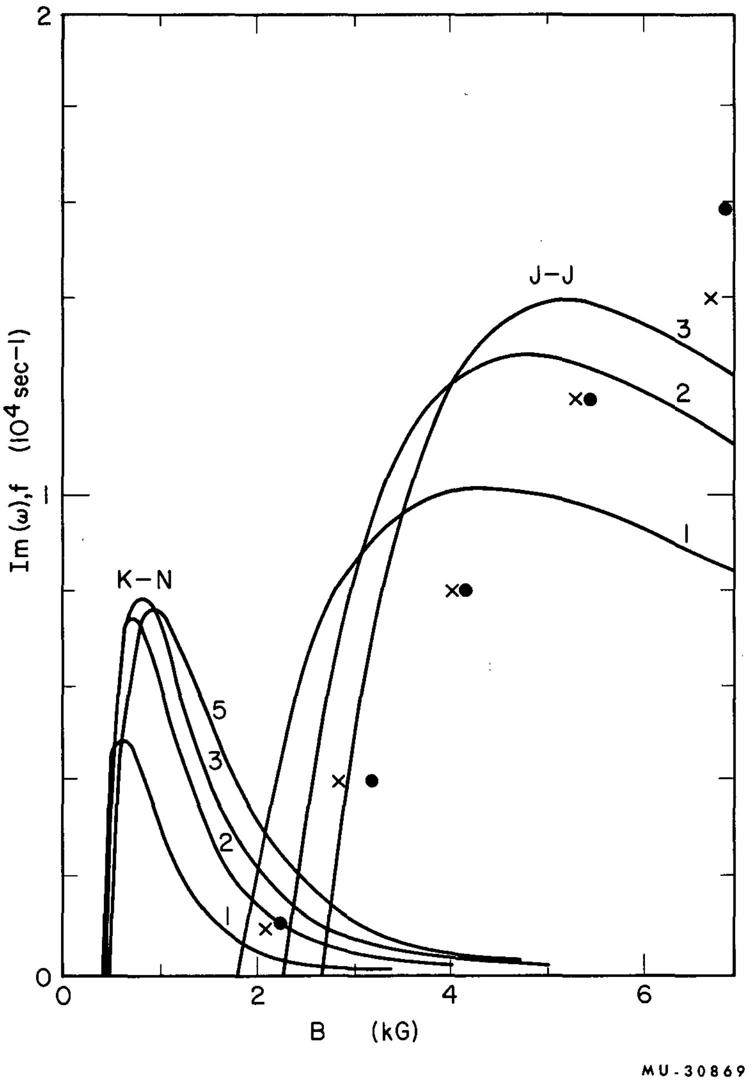

Fig. 32. Im(ω), f vs B, with Ar^+, R = 1.27 cm, p = 0.20 mm Hg, I = 500 mA, square wave ●, sine wave ×.

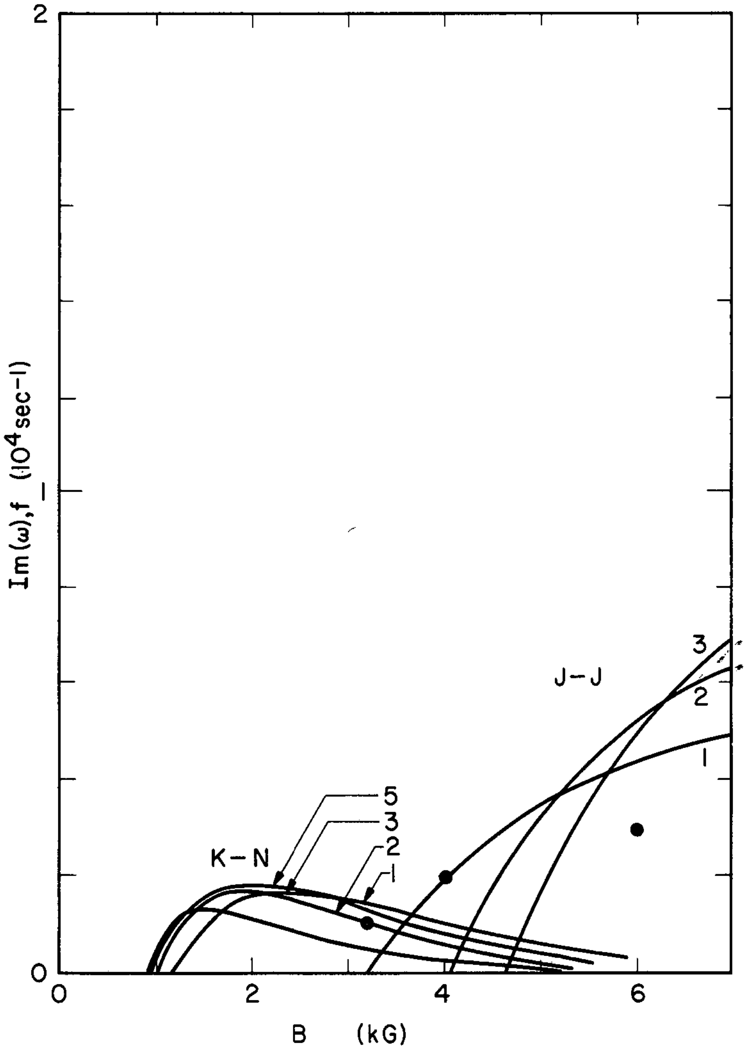

MU-30870

Fig. 33. Im(ω), f vs B, with Ar^+, R = 1.27 cm, p = 0.6 mm Hg, I = 500 mA, square wave.

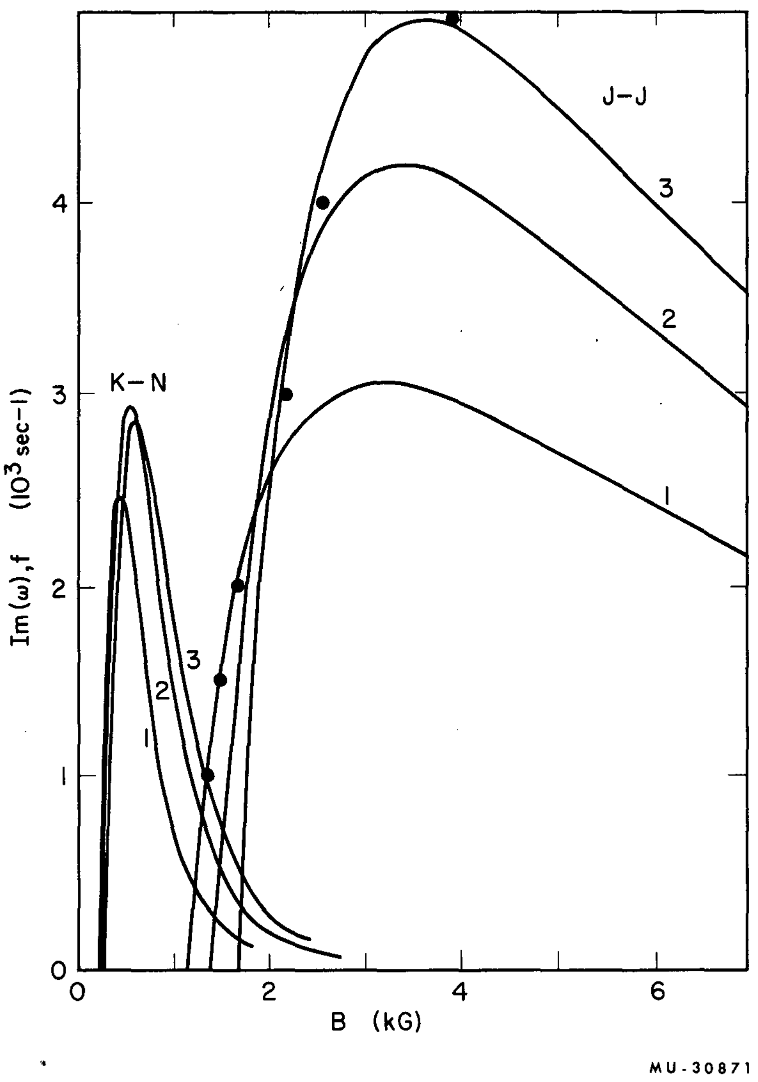

Fig. 34. Im(ω), f vs B, with Ar^+, R = 2.75 cm, p = 0.20 mm Hg, I = 500 mA, square wave.

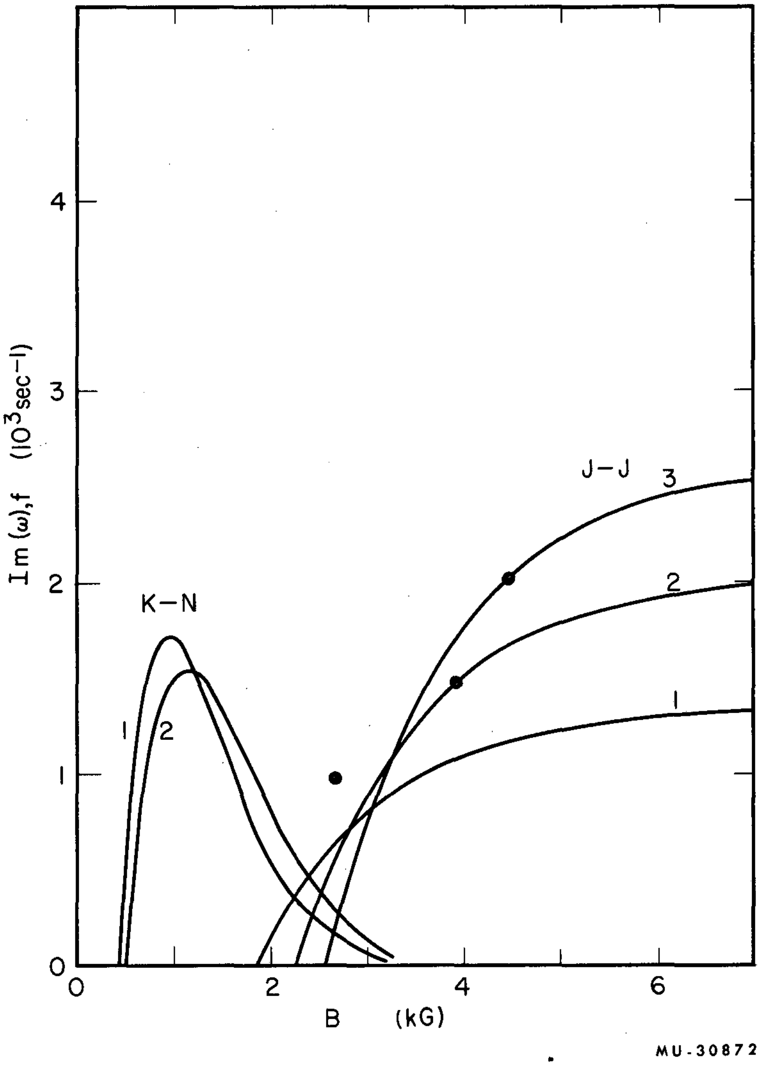

Fig. 35. Im(ω), f vs B, with Ar^+, p = 0.6 mm Hg, R = 2.75 cm, I = 500 mA, square wave.

The theoretical growth rates were calculated from both the Kadomtsev and the Johnson and Jerde[9] theory for several values of m. The calculations were done on an IBM 7090 computer. Equation II-11 yielded the growth rate Im(ω) for the Kadomtsev theory as a function of magnetic field B and azimuthal mode number m. The wave numbers k(B) were obtained from the solution of Eq. (II-13). The growth rates from the Johnson and Jerde theory were obtained in the manner described in Appendix A. The solution of these equations required values of axial electric field, electron temperature, and electronic and ionic mobilities. The same values of these parameters were used in both calculations. The axial electric fields as a function of B were obtained from the ac experiments when feasible (Appendix D). When this was not possible, they were normalized to the corresponding dc values, which were generally within 10% (Subsec. IV-B). The electron temperatures as a function of magnetic field were calculated from the modified Schottky theory for consistency and for efficiency in the computer calculations. These values agreed well with the dc experimental temperatures Subsec. (IV-A). Ionic and electronic mobilities were taken from a summary by Brown,[18] except for H_2^+ and D_2^+, which were obtained from Chanin.[45] It is probable that both atomic and molecular ions existed in the discharges. Therefore separate calculations were made with molecular ion mobilities and these are shown in several of the figures. It can be seen that the Kadomtsev and the Johnson and Jerde calculations are relatively insensitive to the value of the ion mobility. Generally the dc critical magnetic field [Im(ω) = 0] is approximately 10% less for the molecular ion, whereas the growth rates are somewhat larger.

Positive values of Im(ω) correspond to the region of instability. The lowest magnetic field at which Im(ω) is equal to zero is by definition the critical magnetic field in the dc case. As can be seen from the figures, Figs. 23 through 35, the m = 1 mode usually becomes unstable first, followed at higher magnetic fields by the higher-valued m modes. It is also evident from the figures that at magnetic fields higher than the dc critical field the theoretical growth rates of higher m-value modes may exceed that of $m = 1$. Hence, if the onset of instability is suppressed to a magnetic field at which a mode $m > 1$ has the largest growth rate, this mode could be expected to become unstable first, possibly closely followed by the other modes that corresponded to values of $\mathrm{Im}(\omega) > 0$ at that particular magnetic field. The more abrupt increase observed in the electric field (Fig. 16) at the onset of instability in the ac discharges (as compared with the dc) may be explained by this phenomenon; that is, the large growth rate and several modes contributing to the instability. Thus one would expect the shape of the experimental ac critical magnetic fields vs their current reversal frequency to resemble the envelope of the theoretical growth rates $[\mathrm{Im}(\omega_{\mathrm{max}})]$, for all values of m, vs magnetic field in those regions where the quasi-dc approach is valid. The comparison between the magnitude of the growth frequency $(\mathrm{Im}(\omega))$ and the current reversal frequency f at one value of B is dependent upon what ratio of these quantities one assumes is required for the instability to be no longer suppressed. For example, one might assume that the instability would no longer be suppressed if the growth frequency just exceeded the field reversal frequency, $[\mathrm{Im}(\omega)/f \geqslant 1]$. This would be equivalent to stating that if the density perturbation grew by a factor of e [since $n' e^{\mathrm{Im}(\omega)t} = e^{\mathrm{Im}(\omega)/f}$] or more in one half-cycle of the discharge, the instability would set in, but if it only grew by some factor less than e (i.e., $\mathrm{Im}(\omega)/f < 1$), then it would be suppressed. This factor e is somewhat arbitrary (although probably the logical choice), and the proper comparison between the magnitudes of these quantities is determined by the choice of this factor.

The experimental points are taken from the critical magnetic fields determined by the E_z-vs-B or V_T-vs-B curves previously decribed (Subsec. IV-B). The data were extremely reproducible when duplicate runs were made the same day. Even runs that were made months apart in different tubes (same radius) yielded results that never differed by more than about 5 to 10%. The X' s appearing in Fig. 30 correspond to data taken several months earlier. The pressure could not be duplicated to better than a few percent, and this combined with the slight variations in tubes and possible slight impurities could easily account for the variation.

Qualitatively the experimental results agree well with both the Kadomtsev and the Johnson and Jerde calculations. This is quite evident when comparing Im(ω) and f in He (order of 5×10^4) with that obtained in Ne (order of 10^4) and Ar (order of 10^3). Both experiment and theory show higher rates for smaller values of R and lower pressures.

Quantitatively the Johnson and Jerde theory gives better agreement. Both the values of the experimental dc critical magnetic fields and the growth rates are predicted well, except in the higher frequency range (the value depending on the gas), when the discharges are no longer in a quasi-dc state. Similarly, the sine-wave data generally agreed well with the square-wave results in the lower frequency range, but deviated somewhat at higher frequencies. An example of this is shown in Fig. 32. The quantitative failure of the Kadomtsev calculation at higher values of B is probably due to neglect of the magnetic field effect on the ions since this is not a negligible effect in the range of magnetic fields employed (several kilogauss).

V. SUMMARY AND CONCLUSIONS

The instability of a positive column immersed in a strong magnetic field is shown to be suppressed when the discharge is run in an ac manner such that the current reversal frequency is greater than the growth rate of this instability. Examination of half-wave rectified (unidirectional) discharges verified that actual current reversal is required for suppression rather than simply a strong modulation frequency. The onset of the instability occurs at higher magnetic fields as the ac frequency is increased. This agrees with the Kadomtsev model of the stability of the discharge.

Direct-current discharge measurements were taken and verified previous experimental results.[1, 2] Total voltage measurements were compared with their ac counterparts and good agreement was obtained. Electron temperatures were obtained near the critical magnetic field and were seen to agree well with those predicted by the modified Schottky theory, which were used in the theoretical calculations of the Kadomtsev theory.

Critical magnetic fields in the ac discharges were determined from E_z-vs-B or V_T-vs-B curves. The onset of the instability was generally characterized by a much sharper increase in the voltage than in the corresponding dc case. This is probably due to the larger growth rates involved and more than one mode becoming unstable at the higher magnetic fields employed. The helical nature of the $m = 1$ mode was also established in the ac discharges by means of streak photographs; the rotational frequency of these spirals agreed with dc measurements[1, 2] and theory.[6, 9] Turbulent discharges appeared at magnetic fields higher than the critical field.

Qualitative agreement is obtained between the experimental data and the growth-rate curves calculated from the analyses of Kadomtsev, and Johnson and Jerde. However, quantitatively, the Johnson and Jerde theory yields better results, giving generally good agreement with experimental values of the critical magnetic fields in both the dc and ac cases.

ACKNOWLEDGMENTS

I especially wish to thank Dr. Robert V. Pyle for his guidance, encouragement, and suggestions during the course of this work. I am grateful to J. Warren Stearns for helping with the measurements and design of equipment; to Marvin Hartley, Vincent Honey, and Donald Hopkins for the construction of the ac power supplies; to Dr. Wulf B. Kunkel, Dr. Günter Ecker, Dr. George A. Paulikas, and Dr. Roy R. Johnson for many helpful discussions of the theory and experiment; and to Dr. C. M. Van Atta for his support of this research. The experiment could not have been completed without the assistance of Harry Powell's glass shop and the mechanical shops of John Meneghetti and Harlan Hughes. I also wish to express my appreciation to Margaret Thomas for typing the manuscript.

This research was performed under the auspices of the U. S. Atomic Energy Commission.

LIST OF SYMBOLS

B	Magnetic field
D_a	Ambipolar diffusion coefficient at B
$D_\mp$	Diffusion coefficients of electrons or ions
$E_{r,\phi,z}$	Components of electric field
f	Electric field (current) reversal frequency = $2\,f_{osc}$
f_{osc}	Oscillator frequency
I	Discharge current
J_i	Bessel functions of ith order
κ	Boltzmann constant
k	Wave number (2π/wavelength)
$\lambda_\mp$	Mean free path of electrons or ions
$\mu_\mp$	Electron or ion mobilities
m	Azimuthal mode number
$m_\mp$	Electron or ion masses
$n_\mp$, n	Particle densities of electrons or ions
ν_i	Ionization rate per second per electron
$\Omega_\mp$	Electron or ion cyclotron frequencies
ω	Angular frequency
$\mathrm{Im}(\omega)$	Theoretical growth rate
$\mathrm{Re}(\omega)$	Theoretical rotational frequency
p	Neutral gass pressure (reduced to 0°C)
R	Discharge-tube radius
$T_\mp$	Electron or ion temperature
$\tau_\mp$	Mean time between collisions of electron or ion with neutral particles

u_+	Ion thermal velocity
V	Electric potential
V_T	Total voltage across discharge tube
$v_{\mp}$	Electron or ion drift velocities

APPENDICES

A. Modification of the Kadomtsev and Nedospasov Instability Theory by Johnson and Jerde

Johnson and Jerde[9] modified the Kadomtsev and Nedospasov theory to include the diffusion and magnetic field interaction terms in the ion equation of motion. They solved the equations of motion and continuity in a rigorous manner without any assumptions regarding the form of the perturbed radial density and potential distribution.

Their process of obtaining a rigorous solution to the problem involves much tedious algebra, many substitutions, and several transformations of variables. For this reason a reproduction of the theory section of their recent Physics of Fluids article which pertains to our analysis follows, with the following corrections:* The sixth term of Eq. (29) should read $D_{11}^2 a_7^2 (1 - y)z$. The same correction appears in Eq. (34c).

The growth rate Im(ω) was calculated as a function of B for m = 1, 2, and 3. Only the first term of the determinant $(E_{11} + 1 = 0)$ was used. The growth rate is defined by Eq. (19) and its value is obtained through Eqs. (25), (26), and (28). Since Eq. (10) defines the perturbations as being proportional to exp(+ iωt), and Kadomtsev defines them as proportional to exp(-iωt), we shall let $\omega \rightarrow -\omega$ in the Johnson and Jerde analysis for consistency in the stability criterion (Im < 0 for stability). The wave numbers necessary for the calculations were obtained from Eq. (33). The values of the axial electric field, electron temperature, and mobilities were the same as used in the Kadomtsev analysis, and are described in Subsec. IV-E.

The error caused by using only the first element of the determinant is estimated in the appendix of their paper. When a 2×2 determinant was calculated, it showed a difference of the order of 6%.

---

*Roy R. Johnson (Boeing Scientific Research Laboratories, Seattle, Washington), private communication.

This difference was such that the corrected value corresponded to a slight decrease in wavelength (which corresponds to a decrease in B_c). Hence, from this first-order correction, it is seen that the approximate solution (using only one term, $E_{11} + 1$) should give slightly higher values of B_c than those obtained by using the full determinant, if the determinant converges.

THEORY

General Macroscopic Equations

The macroscopic equations of motion of ions and electrons in a positive column can be derived by taking the zeroth and first velocity moments of the Boltzmann transport equation along with an assumed equation of state of the system, given by

$$P_\pm = n_\pm kT_\pm . \qquad (1)$$

Here the $-$ and $+$ subscripts refer to electron and ion quantities, respectively, P is the scalar pressure, n the configuration space density, k the Boltzmann constant, and T the temperature. These equations can be written in the form

$$\partial n/\partial t + \nabla\cdot\boldsymbol{\Gamma}_\pm = n\xi \qquad (2)$$

and

$$\boldsymbol{\Gamma}_\pm + D_\pm\nabla n \pm \mu_\pm n\mathbf{E} \pm \mu_\pm\boldsymbol{\Gamma}\times\mathbf{B} = 0. \qquad (3)$$

Equation (2) is the continuity equation, where $\boldsymbol{\Gamma}_\pm = n\mathbf{v}_\pm$ is the particle flux vector, $\mathbf{v}_\pm$ being the average velocity of either component of the plasma, and ξ is the number of ion–electron pairs created per second per electron. These equations are written using the assumptions that the mobilities are determined by collisions with neutrals, the column is isothermal and quasi-neutral ($n_- \cong n_+$), and the characteristic frequencies of the column are much less than the collision frequencies.

In Eq. (3) $D_\pm$ are the electron and ion diffusion coefficients, $\mu_\pm$ the mobilities, and $\mathbf{B}$ and $\mathbf{E}$ the magnetic and electric fields, respectively.

We now solve Eq. (3) for $\boldsymbol{\Gamma}_\pm$ explicitly, take its divergence and combine the result with Eq. (2) obtaining the following two equations in which $\boldsymbol{\Gamma}_\pm$ has been eliminated:

$$\begin{aligned}-\frac{\partial n}{\partial t} &+ n\xi + D_\pm'\nabla^2 n \pm \mu_\pm'\nabla\cdot(n\mathbf{E})\\ &+ \mu_\pm\mu_\pm'\nabla\cdot(n\mathbf{B}\times\mathbf{E})\\ &+ \mu_\pm^2 D_\pm'\mathbf{B}\cdot\nabla(\mathbf{B}\cdot\nabla n \pm n\mathbf{B}\cdot\mathbf{E}) = 0. \qquad (4)\end{aligned}$$

Here

$$\mu_\pm' = \frac{\mu_\pm}{1+\mu_\pm^2B^2}\,; \qquad D_\pm' = \frac{D_\pm}{1+\mu_\pm^2B^2}. \qquad (5)$$

In arriving at this result, we have used the conditions $\nabla\cdot\mathbf{B} = 0$ and $\nabla B^2 = 0$, the latter justifying taking $\mu_\pm'$ and $D_\pm'$ outside the ∇ operator. We have also assumed that the internal magnetic field is negligible relative to the large uniform longitudinal magnetic field which is being externally applied to the column, and hence, that $\nabla\times\mathbf{B} = 0$.

Steady-State Solutions

We will first treat the case of an unperturbed cylindrical positive column in a uniform longitudinal magnetic field $\mathbf{B} = B_0\mathbf{1}_z$ where there are no gradients of density or electric fields in the z and θ directions. In that case, the solution for the electron density in Eq. (4) is

$$n_0(r) = N_0J_0(\beta_0 r), \qquad (6)$$

where

$$\begin{aligned}\beta_0^2 &= \frac{(\mu_+' + \mu_-')\xi}{\mu_+' D_-' + \mu_-' D_+'}\\ &= \frac{\xi}{V_- + V_+}\left(\frac{1}{\mu_-'} + \frac{1}{\mu_+'}\right) = \left(\frac{2.4}{R}\right)^2 \qquad (7)\end{aligned}$$

and $V_\pm$ are the electron and ion temperatures expressed in electron volts.

The radial electric field in the unperturbed plasma is found to be

$$\begin{aligned}E_{0r} &= -\frac{D_-' - D_+'}{\mu_+' + \mu_-'}\frac{1}{n_0}\frac{\partial n_0}{\partial r}\\ &= \frac{\alpha}{n_0}\frac{\partial n_0}{\partial r} = -\alpha\beta_0\frac{J_1(\beta_0 r)}{J_0(\beta_0 r)}, \qquad (8)\end{aligned}$$

since E_{0r} must be zero on the axis.

Linearized Equations and Normal Mode Analysis

To first order in perturbations of n and $\mathbf{E}$, Eq. (4) is

$$\begin{aligned}n_1\xi &- (\partial n_1/\partial t) + D_\pm'\nabla^2 n_1 \pm \mu_\pm'\nabla\cdot(n_0\mathbf{E}_1 + n_1\mathbf{E}_0)\\ &+ \mu_\pm\mu_\pm'\nabla\cdot[\mathbf{B}\times(n_0\mathbf{E}_1 + n_1\mathbf{E}_0)]\\ &+ \mu_\pm^2 D_\pm'\mathbf{B}\cdot\nabla(\mathbf{B}\cdot\nabla n_1)\\ &\pm \mu_\pm^2\mu_\pm'\mathbf{B}\cdot\nabla[\mathbf{B}\cdot(n_0\mathbf{E}_1 + n_1\mathbf{E}_0)] = 0. \qquad (9)\end{aligned}$$

We now take a Fourier transform of n_1 and V_1 in θ, z, and t by writing

$$n_1 = f(r)\exp[i(kz + m\theta + \omega t)], \qquad (10a)$$

$$V_1 = g(r)\exp[i(kz + m\theta + \omega t)]. \qquad (10b)$$

We also have that

$$E_{1r} = -\frac{dg/dr}{g}V_1; \qquad E_{1\theta} = -\frac{im}{r}V_1;$$

$$E_{1z} = -ikV_1. \qquad (11)$$

Using Eqs. (10a), (10b), (11), the form $\mathbf{B} = B_0\mathbf{1}_z$ for the magnetic field, and assuming E_{0z} is a constant whose value is determined by the amount of the wall losses. Eq. (9) becomes

$$D_-'\frac{1}{r}\frac{d}{dr}\left(r\frac{df}{dr}\right) \pm \mu_-'\frac{1}{r}\frac{d}{dr}(rfE_{0r})$$
$$+\left(\xi - i\omega - D_-'\frac{m^2}{r^2}\right.$$
$$\left.+\frac{im}{r}\mu_-'B_0E_{0r} - D_-k^2 \pm i\mu_-kE_{0z}\right)f$$
$$= \pm\mu_-'\frac{1}{r}\frac{d}{dr}\left(rn_0\frac{dg}{dr}\right) - im\mu_-\mu_-'B_0\left(\frac{1}{r}\frac{dn_0}{dr}\right)g$$
$$\mp\left(\mu_-'n_0\frac{m^2}{r^2} + \mu_-n_0k^2\right)g, \qquad (12)$$

where we have written the differential operators explicitly.

Derivation of the General Dispersion Relation

We now define a new variable $l(r)$ by the equation

$$g(r) = [1/n_0(r)][(V_- + V_+)l(r) - \alpha f(r)], \qquad (13)$$

where α is given in Eq. (8). Substituting (13) into (12) and using (8) we arrive at

$$\frac{\mu_-'}{\mu_+' + \mu_-'}\left[\frac{1}{r}\frac{d}{dr}\left(r\frac{df}{df}\right) - \frac{m^2}{r^2}f\right] + \left\{\frac{\xi - i\omega \pm \mu_-kE_{0z}}{(V_- + V_+)\mu_-'}\right.$$
$$\left.- \frac{\mu_-k^2\left[\frac{\mu_-'}{\mu_+' + \mu_-'}(V_- + V_+)\right]}{(V_- + V_+)\mu_-'}\right\}f$$
$$= \pm\left[\frac{1}{r}\frac{d}{dr}\left(r\frac{dl}{dr}\right) - \frac{1}{r}\frac{d}{dr}\left(\frac{r}{n_0}\frac{dn_0}{dr}l\right)\right.$$
$$\left.\mp im\mu_-B_0\frac{1}{rn_0}\frac{dn_0}{dr}l - \frac{\mu_-}{\mu_-'}k^2l - \frac{m^2}{r^2}l\right]. \qquad (14)$$

We now notice that the operator acting on f is an mth-order Bessell operator and so we will proceed at this point to transform the equation by the use of finite Hankel transforms. The following notation defines the transform pairs which will be used:

$$F(\beta_i) = \int_0^R f(r)J_m(\beta_ir)r\,dr \leftrightarrow f(r)$$
$$= \frac{2}{R^2}\sum_{i=1}^{\infty} F(\beta_i)\frac{J_m(\beta_ir)}{[J_m'(\beta_iR)]^2}, \qquad (15a)$$

$$L(\beta_i) = \int_0^R l(r)J_m(\beta_ir)r\,dr \leftrightarrow l(r)$$
$$= \frac{2}{R^2}\sum_{i=1}^{\infty} L(\beta_i)\frac{J_m(\beta_ir)}{[J_m'(\beta_ir)]^2}, \qquad (15b)$$

where $J_m(\beta_jR) = 0$, for all j. We shall assume the density perturbation $f(r)$ is zero at $r = R$, and so from Eq. (13), $l(R) = 0$ as long as $g(R)$ is finite, which is quite certainly the case. From Eqs. (15a) and (15b), we have that

$$\frac{1}{r}\frac{d}{dr}\left(r\frac{df}{dr}\right) - \frac{m^2}{r^2}f \text{ is transformed to } -\beta_i^2F(\beta_i) \qquad (16a)$$

and

$$\frac{1}{r}\frac{d}{dr}\left(r\frac{dl}{dr}\right) - \frac{m^2}{r^2}l \text{ is transformed to } -\beta_i^2L(\beta_i). \qquad (16b)$$

Equations (14) are thus transformed into

$$\left[\frac{-\beta_i^2\mu_-'}{\mu_+' + \mu_-'} + \frac{\xi - i\omega \pm ik\mu_-E_{0z}}{\mu_-'(V_- + V_+)}\right.$$
$$\left.- k^2\frac{\mu_-\mu_-'}{(\mu_+' + \mu_-')\mu_-'}\right]F(\beta_i)$$
$$= \pm\left[-\beta_i^2 - \frac{\mu_-}{\mu_-'}k^2\right]L(\beta_i)$$
$$\pm\int_0^R\left\{\frac{-1}{r}\frac{d}{dr}\left[\frac{r}{n_0}\frac{dn_0}{dr}l(r)\right]\right.$$
$$\left.\mp im\mu_-B_0\frac{1}{rn_0}\frac{dn_0}{dr}l(r)\right\}J_m(\beta_ir)r\,dr. \qquad (17)$$

The next step is to eliminate $F(\beta_i)$ from Eqs. (17). This involves a rather tedious amount of algebra, which we shall not reproduce here.

We shall define the following quantities involving the mobilities:

$$a_1 = \frac{\mu_-' + \mu_+'}{\mu_-'\mu_+'}; \qquad a_2 = \frac{\mu_+\mu_-' + \mu_-\mu_+'}{\mu_-'\mu_+'};$$
$$a_3 = \frac{\mu_-\mu_+}{\mu_-'\mu_+'}; \qquad a_4 = \frac{\mu_+ + \mu_-}{\mu_+' + \mu_-'};$$
$$a_5 = \frac{\mu_+\mu_-' - \mu_-\mu_+'}{\mu_-'\mu_+'}; \qquad a_6 = \frac{\mu_+\mu_-'^2 + \mu_-\mu_+'^2}{\mu_-'\mu_+'(\mu_-' + \mu_+')};$$
$$a_7 = \frac{\mu_-\mu_-' - \mu_+\mu_+'}{\mu_-' + \mu_+'}B_0; \qquad a_8 = \frac{\mu_-\mu_+}{\mu_-'\mu_+'}(\mu_-' - \mu_+')B_0;$$
$$a_9 = \frac{\mu_-\mu_-' - \mu_+\mu_+'}{\mu_-'\mu_+'}; \qquad a_{10} = \left(\frac{\mu_-' + \mu_+'}{\mu_-'\mu_+'}\right)\mu_-\mu_+B_0. \qquad (18)$$

Note that $a_1a_7 = B_0a_9$, $a_2 = a_4 + a_6$, and $a_7a_{10} = -a_5$. We shall also use

$$\xi = (V_- + V_+)\beta_0^2/a_1$$

from Eq. (7). The complex frequency ω is now written as

$$\omega = (V_- + V_+)(b_1 + ib_2) \qquad (19)$$

and the longitudinal electric field as

$$E_{0z} = (V_- + V_+)b_3. \qquad (20)$$

The first term of the integral in Eq. (17) can be integrated by parts, recognizing that

$$l(R)J_m(\beta_iR)/n_0(R) = 0. \qquad (21)$$

Then, with Eqs. (18), (19), and (20), Eqs. (17) combine to give

$$[\beta_i^2(\beta_i^2 - \beta_0^2) + k^2(a_4\beta_i^2 + a_3k^2 - a_4\beta_0^2 + a_0\beta_i^2)$$
$$+ a_1(ib_1 - b_2)(\beta_i^2 + a_4k^2) + ika_5b_3\beta_i^2]L(\beta_i)$$
$$- [\beta_i^2 - \beta_0^2 + k^2a_6 + a_1(ib_1 - b_2) + ika_5b_3]$$
$$\cdot \int_0^R \frac{\beta_j r}{n_0}\frac{dn_0}{dr}\, l(r) J_m'(\beta_j r)\, dr$$
$$+ im[a_7(\beta_i^2 - \beta_0^2) + a_7a_1(ib_1 - b_2) + k^2a_8$$
$$+ ikb_3a_{10}] \int_0^R \frac{l(r)}{n_0}\frac{dn_0}{dr} J_m(\beta_j r)\, dr = 0. \qquad (22)$$

We now substitute for $l(r)$ in Eq. (22) in terms of the sum of $L(\beta_i)$'s as defined in Eq. (15b), and invert the order of integration and summation. Furthermore, it is convenient to define the following definite integrals:

$$C_{ij} = \frac{-2}{\beta_j^2R^2[J_m'(\beta_jR)]^2}\int_0^R \frac{\beta_j r}{n_0}\frac{dn_0}{dr} J_m(\beta_i r)J_m'(\beta_j r)\, dr$$
$$= \frac{2}{\beta_j^2R^2[J_m'(\beta_jR)]^2}$$
$$\cdot \int_0^R \frac{\beta_j r J_1(\beta_0 r) J_m(\beta_i r) J_m'(\beta_j r)}{J_0(\beta_0 r)}\, d(\beta_0 r) \qquad (23a)$$

and

$$D_{ij} = \frac{+2}{\beta_j^2R^2[J_m'(\beta_jR)]^2}$$
$$\cdot \int_0^{\beta_0 R} \frac{J_1(\beta_0 r) J_m(\beta_i r) J_m(\beta_j r)}{J_0(\beta_0 r)}\, d(\beta_0 r). \qquad (23b)$$

Equation (22) then represents an infinite set of linear homogeneous algebraic equations for the variables $L(\beta_i)$ ($i = 1, 2, 3, \cdots$), which can be written as

$$L(\beta_j) + \sum_{i=1}^{\infty} E_{ij}L(\beta_i) = 0, \quad j = 1, 2, 3, \cdots , \qquad (24)$$

where

$$E_{ij} = \frac{(A_{0j} + x_j^2a_6 + ib_{1j} - b_{2j} + ix_ja_5b_{3j})C_{ij} - im[A_{0j}a_7 + x_j^2a_8 + a_7(ib_{1j} - b_{2j}) + ix_jb_{3j}a_{10}]\, D_{ij}}{A_{0j} + x_j^2(A_{0j}a_4 + a_3x_j^2 + a_6) + (ib_{1j} - b_{2j})(1 + a_4x_j^2) + ix_ja_5b_{3j}}, \qquad (25)$$

and we have introduced the dimensionless quantities

$$b_{1j} = \frac{a_1b_1}{\beta_j^2}\,; \quad b_{2j} = \frac{a_1b_2}{\beta_j^2}\,; \quad b_{3j} = \frac{b_3}{\beta_j}\,; \quad x_j = \frac{k}{\beta_j}\,;$$
$$A_{0j} = 1 - \beta_0^2/\beta_j^2. \qquad (26)$$

The eigenvalues of the system of equations represented by (24) are given by the following infinite determinant, which is the general dispersion relation for linear perturbations in the positive column:

$$\left|\begin{array}{cccccc} 1 + E_{11} & E_{12} & \cdots & E_{1j} & \cdots \\ & & & \vdots & \\ E_{21} & 1 + E_{22} & & & \\ \vdots & & & \vdots & \\ E_{i1} & \cdots & \cdots & E_{ij} & \cdots \\ \vdots & & & \vdots & \\ E_{j1} & \cdots & \cdots & 1 + E_{jj} & \cdots \\ \vdots & & & \vdots & \end{array}\right| = 0. \qquad (27)$$

Application to the Stability of a Helical Perturbation

As an example of the application to a specific problem, we shall consider the case of $m = 1$, which corresponds to a helical perturbation of the column. We will find the solution for a one-by-one determinant and compute the error introduced by this approximation in the Appendix. That is, we shall calculate the stability criterion for $m = 1$ on the approximation that

$$1 + E_{11} = 0. \qquad (28)$$

Since a_1 and β_i^2 are positive, it follows from Eq. (26) and (19) that b_{21} has the same sign as ω_i, and hence the requirement for stability is that $b_{21} \geq 0$. By solving Eq. (28) for b_{21}, using (25), this requirement becomes

$$(1 + a_7^2)^2z^3 + [2(1 + C_{11})(1 + a_7^2)(1 + \tfrac{1}{2}a_7^2y)$$
$$+ A_{01}(1 + a_7^2)^2]z^2 + [(1 + C_{11})^2(1 + a_7^2y)$$
$$+ 2A_{01}(1 + C_{11})(1 + a_7^2) + D_{11}^2a_7^2(1 \mp y)]z$$
$$+ A_{01}[(1 + C_{11})^2 + D_{11}^2a_7^2] \qquad (1 - \gamma)$$
$$\geq -[a_7^2(1 + y)^2 + 4y]^{\frac{1}{2}}\, D_{11}b_{31}z^{\frac{1}{2}}$$
$$\cdot(1 + y)^{\frac{1}{2}}(1 + a_7^2)(1 + C_{11} + z), \qquad (29)$$

where

$$y = \mu_-\mu_+B^2 \qquad (30)$$

and

$$z = (1 + y)x_1^2. \qquad (31)$$

From Eqs. (23a), (22b), and (26), we find the following numerical values for parameters occurring in Eq. (29):

$A_{01} = 0.60611$; $1 + C_{11} = 0.413$; $D_{11} = 0.295$.

From Eq. (18) we can write $a_7 = f(\mu_-/\mu_+)g(y)$, and especially

$$\left[\frac{a_7^2(1+y)^2}{y}+4\right]^{\frac{1}{2}} = \left(\frac{\mu_-}{\mu_+}\right)^{\frac{1}{2}} + \left(\frac{\mu_+}{\mu_-}\right)^{\frac{1}{2}}. \tag{32}$$

Thus the only remaining quantity to be specified in Eq. (29) is the ratio of electron and ion mobilities. The three unknowns in Eq. (29) are y, z, and b_{31}. z involves the magnetic field and the wave number of the perturbation, y involves the magnetic field, and b_{31} involves the longitudinal electric field. Notice that the stability criterion is not affected by a change in the sign of either the magnetic field or the longitudinal electric field. In the latter case the wave number k is reversed and the helix has the opposite pitch.

At the boundary between stability and instability, the equality sign in Eq. (29) must hold, and also the derivatives of both sides of (29) with respect to k (or equivalently, with respect to z) must be equal. These conditions give us two equations in three variables. We choose to eliminate b_{31}, obtaining the following relation involving B and k at the boundary of instability:

$$3G_1G_5z^4 + (5G_1 + G_2G_5)z^3 + (3G_2 - G_3G_5)z^2 + (G_3 - 3G_4G_5)z - G_4 = 0, \tag{33}$$

where

$$G_1 = (1 + a_7^2)^2, \tag{34a}$$

$$G_2 = 2(1 + C_{11})(1 + a_7^2)(1 + \tfrac{1}{2}a_7^2y) + A_{01}(1 + a_7^2)^2, \tag{34b}$$

$$G_3 = (1 + C_{11})^2(1 + a_7^2y) + 2A_{01}(1 + C_{11}) \cdot (1 + a_7^2) + D_{11}^2a_7^2(1 \pm y), \tag{34c}$$

$$G_4 = A_{01}[(1 + C_{11})^2 + D_{11}a_7^2], \tag{34d}$$

$$G_5 = 1/(1 + C_{11}). \tag{34e}$$

When a specific gas is chosen, the ratio of mobilities is specified and the solution for the stability criterion is completely determined. One can now calculate G_1, G_2, G_3, G_4, and G_5 for various values of y. The one positive real root of Eq. (33) can then be determined, giving the wavelength of the helix at the point of instability for chosen values of y. These values of y and z can then be used in Eq. (29) to determine the corresponding values of b_{31}, and hence the ratio of longitudinal electric field to electron temperature at the point of instability. In other words, one is able to construct a curve of b_{31} vs y which divides the stable and unstable regions and defines, for a given longitudinal electric field, the critical magnetic field at the onset of the instability and the wavelength of the perturbation at this critical field.

APPENDIX

A rigorous proof of convergence of the determinant in Eq. (27) is difficult. One can prove, however, that a determinant whose elements are upper bounds for the terms given by Eq. (25) does converge.

The example which was presented was determined from the consideration of a 1 × 1 determinant. We now consider the validity of this operation by determining the error between that case and a 2 × 2 determinant. The second-order determinant is written as

$$\begin{vmatrix} 1 + E_{11} & E_{21} \\ E_{12} & 1 + E_{22} \end{vmatrix} = 0. \tag{A1}$$

It is now necessary to determine how large the correction is with respect to unity. It is possible to determine this correction as a function of the magnetic field. The value for E_{11} thus calculated from (A1) for $y = 4$,

$$E_{11} = -1 + 0.0302 + i.0512, \tag{A2}$$

which shows a correction of a magnitude of 6%. Two other cases which were considered were those of $y = 0$, and $y = \infty$. The results are

$$\begin{aligned} y = 0\ ; \quad & E_{11} = -1 + 0.0202, \\ y = \infty ; \quad & E_{11} = -1 + 0.0681. \end{aligned} \tag{A3}$$

These results indicate that the degree of error in considering a 1 × 1 determinant increases with increasing magnetic field. After the error for a given magnetic field is determined, this new value is used in place of unity in Eq. (28) and the new values of wavelength, electric field and frequency can be determined. The new error in E_{11} is then calculated and this iterative process should converge rapidly. When this was done for the two asymptotic cases it was found that the change in the parameter z was 0.34% for $y = 0$ and 1.6% for $y = \infty$. This corresponds to a change in λ/R from 4.035 to 4.029 at $y = 0$. Thus the approximation made in considering one term of the determinant appears to be valid.

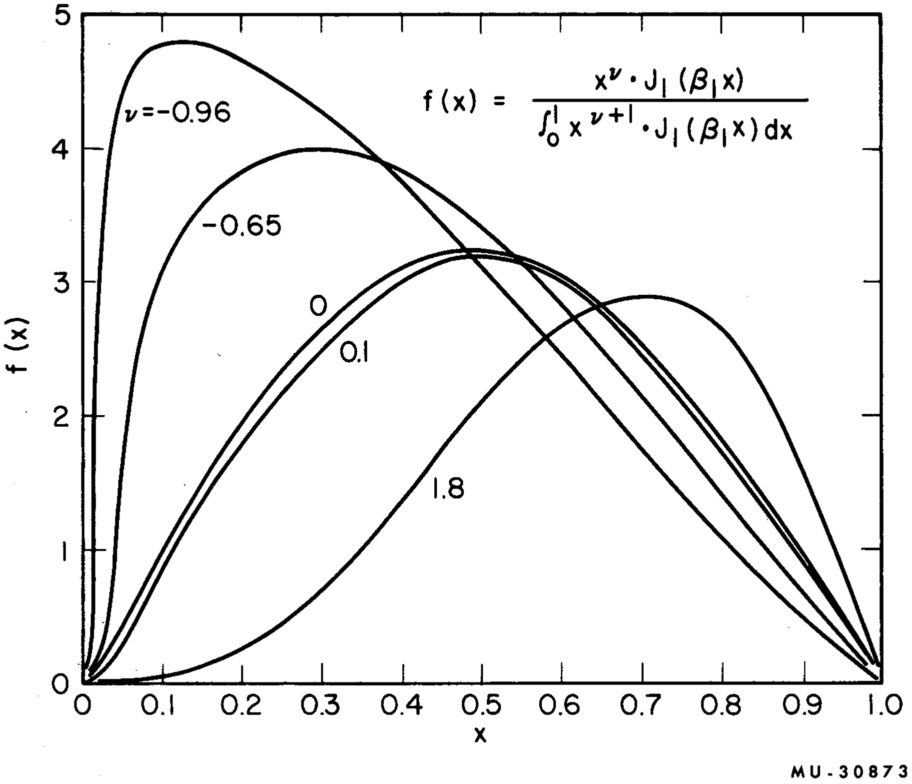

Fig. A-1. Curves showing various trial functions for perturbed radial density distribution (from Ecker[39]).

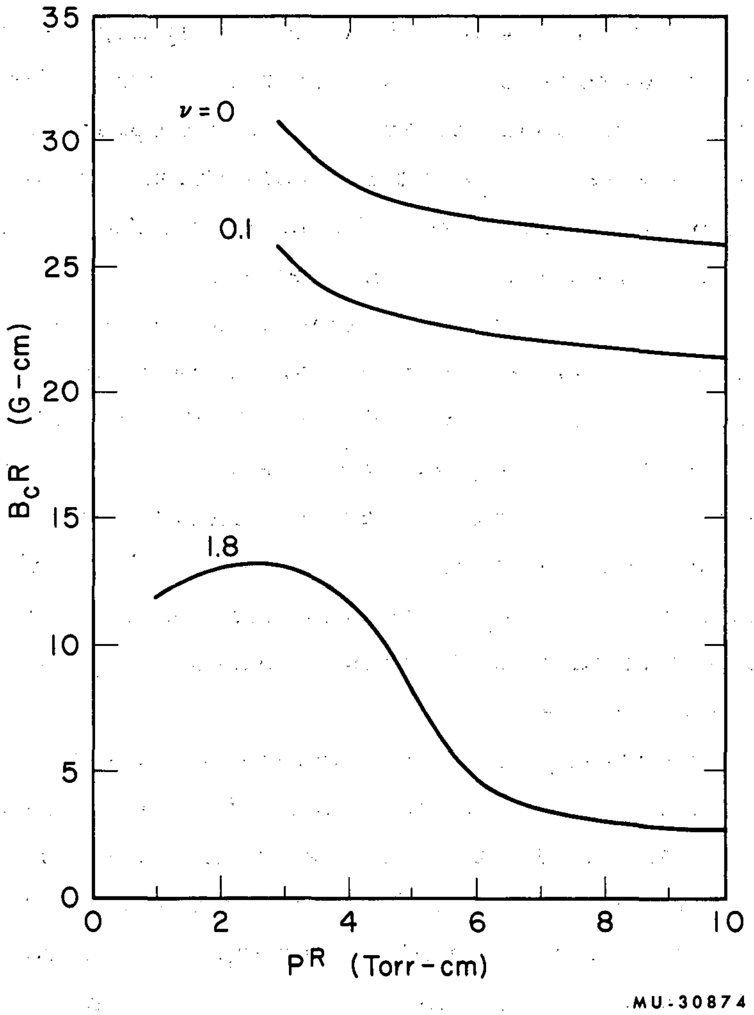

Fig. A-2. Effect of various trial functions for the perturbed radial density distribution on the value of B_c (from Ecker[39]).

B. Electron-Temperature Measurements

Electron-temperature measurements were made in He, Ne, and Ar dc discharges. Both single-[41, 42] and double-probe[43] techniques were employed at B = 0 and B slightly less than B_c. The measurements were taken with the probes shown in Fig. B-1. All measurements were made on axis (r = 0), except for a few single-probe measurements that were taken near the tube wall to check the radial variation of temperature. These temperatures were found to differ by less than 5% from the on-axis values.

Single-probe measurements in both tubes (R = 2.75 and 1.27 cm) made at B > 0 gave fairly good agreement with the modified Schottky theory values as seen in Table I. At B = 0 the single-probe measurements in He were in good agreement with previous measurements by Karelina,[46] and Bickerton and von Engel;[19] those in Ar were in good agreement with measurements by Klarfeld;[47] and those in Ne compared reasonably well with data from Seeliger and Hirchert.[48] In all cases the results had to be normalized to T_e-vs-Rp curves in order to make a comparison.

Generally, double-probe measurements should be more reliable than single-probe measurements, since no current is drawn from the plasma, and the floating probes are not as strongly affected by fluctuations in the plasma. Double-probe measurements were made with the plane of the probes parallel and perpendicular to the magnetic field. The temperatures obtained usually were identical. The double-probe temperatures obtained were reproducible. This effect was more noticeable in the small tube (R = 1.27 cm). A measurement employing the single probe technique using one probe of the double-probe arrangement gave a value approximately 25% lower than a measurement made with the actual single probe under the same conditions. This suggests that the physical size of the double probe may perturb the plasma to a large extent.

While the double-probe measurements were not always reproducible, the single-probe measurements gave results consistent with

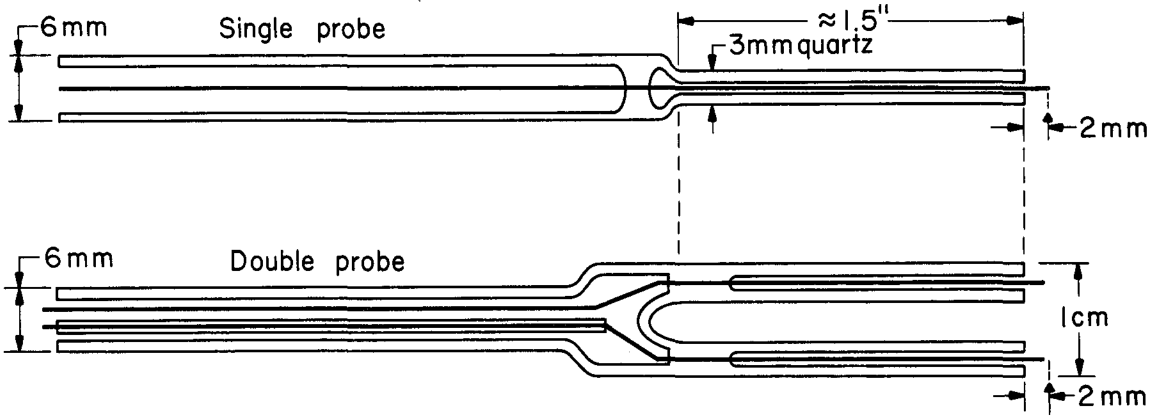

MU-30875

Fig. B-1. 20-mil-tungsten single and double probes. Each probe of the double-probe system is identical with the single probe.

previous measurements at $B = 0$, and consistent with the Bickerton and von Engle measurements and their modified Schottky theory in a magnetic field. Although there was some variation (10 to 20%),* the consistency of these measurements encouraged the use of the modified Schottky theory in the computer calculations of growth rates.

---

*The experimental temperatures were generally slightly lower than those calculated from the modified Schottky theory. Their use would result in proportionally higher values of B_c.

C. Oscilloscope Traces of Discharge Voltage and Current in the Alternating-Current Discharges

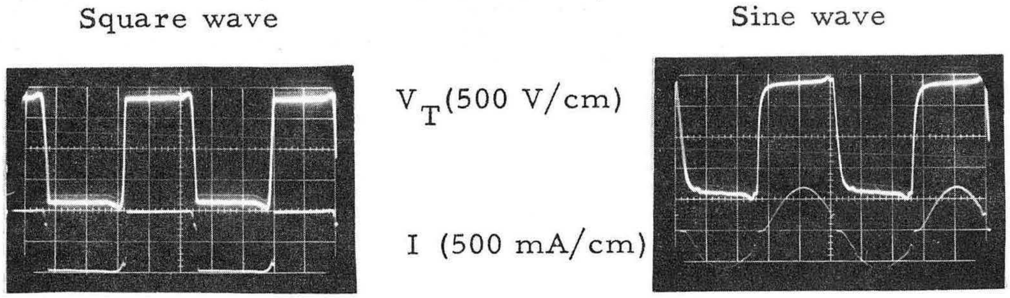

(a)
f_{osc} = 1 kc
t = 200 μsec/cm

(c)
f_{osc} = 1 kc
t = 200 μsec/cm

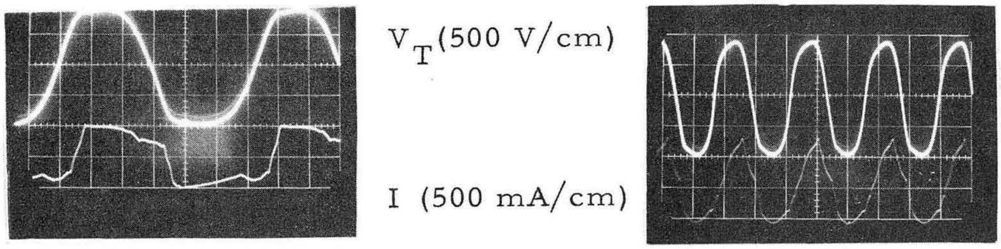

(b)
f_{osc} = 8 kc
t = 20 μsec/cm

(d)
f_{osc} = 8 kc
t = 50 μsec/cm

ZN-3751

Fig. C-1. Comparison of voltage and current vs oscillator frequency for H_2 gas, R = 2.75 cm, p = 0.1 mm Hg, B = 0.

Square wave

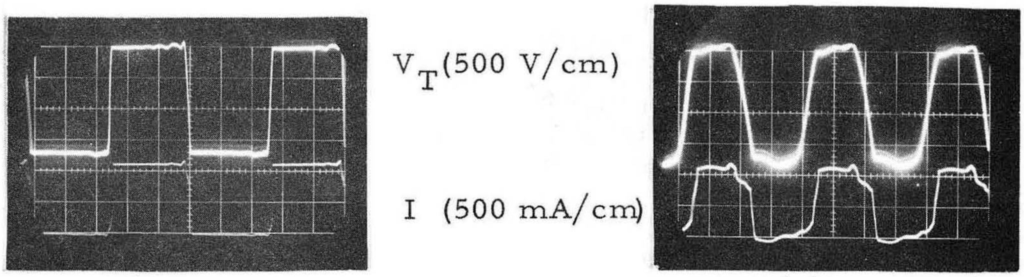

(a)
f_{osc} = 1 kc
t = 200 μsec/cm

(c)
f_{osc} = 5 kc
t = 50 μsec/cm

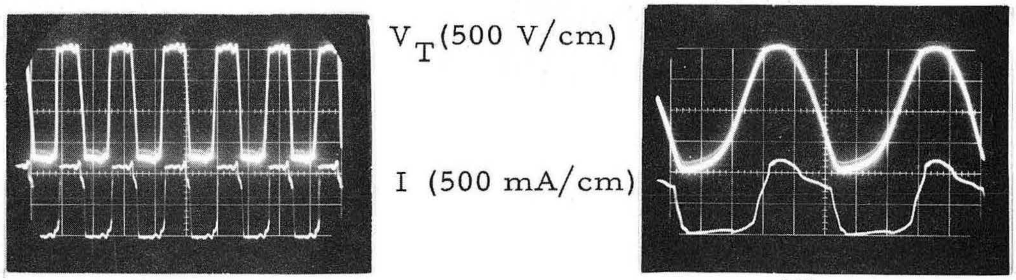

(b)
f_{osc} = 3 kc
t = 200 μsec/cm

(d)
f_{osc} = 10 kc
t = 20 μsec/cm

ZN-3752

Fig. C-2. Comparison of voltage and current vs oscillator frequency for He gas, R = 1.27 cm, p = 0.9 mm Hg, B = 0 (square wave).

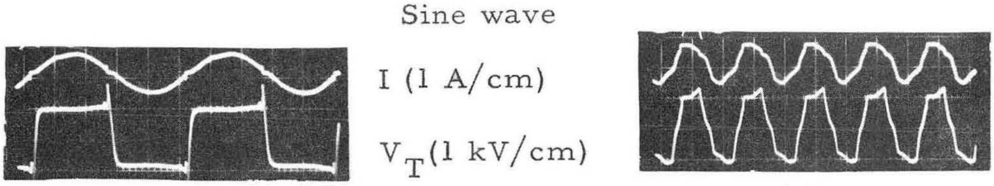

(a)
f_{osc} = 200 cps
t = 1 msec/cm

(c)
f_{osc} = 5 kc
t = 100 μsec/cm

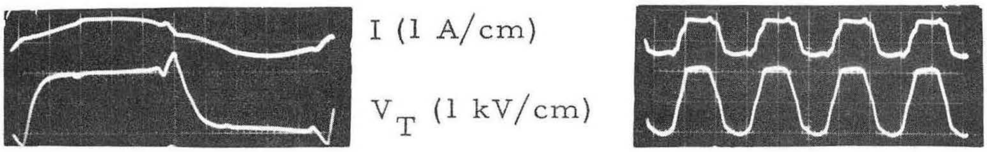

(b)
f_{osc} = 1 kc
t = 100 μsec/cm

(d)
f_{osc} = 20 kc
t = 20 μsec/cm

ZN-3753

Fig. C-3. Comparison of voltage and current vs oscillator frequency for He gas, R = 1.27 cm, p = 0.9 mm Hg, B = 0 (sine wave).

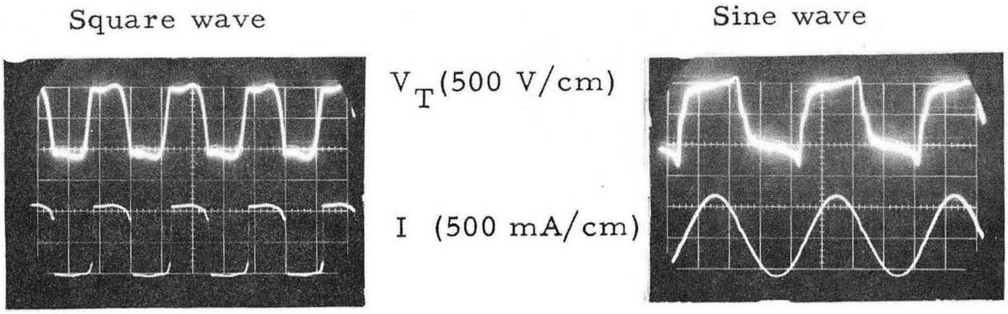

(a)
f_{osc} = 4 kc
t = 100 μsec/cm

(c)
f_{osc} = 500 cps
t = 500 μsec/cm

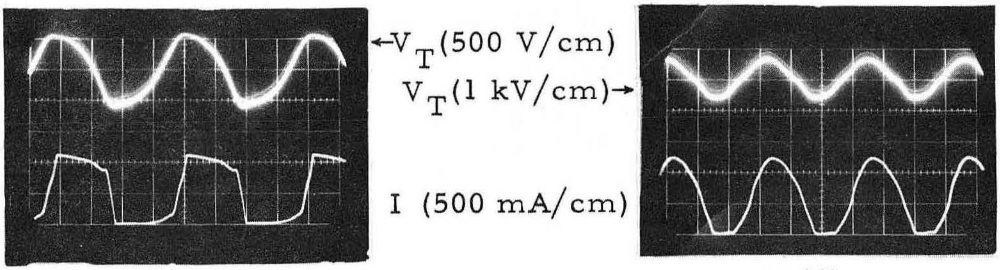

(b)
f_{osc} = 12 kc
t = 20 μsec/cm

(d)
f_{osc} = 6 kc
t = 50 μsec/cm

ZN-3754

Fig. C-4. Comparison of voltage and current vs oscillator frequency for He gas, R = 2.75 cm, p = 0.65 mm Hg, B = 0.

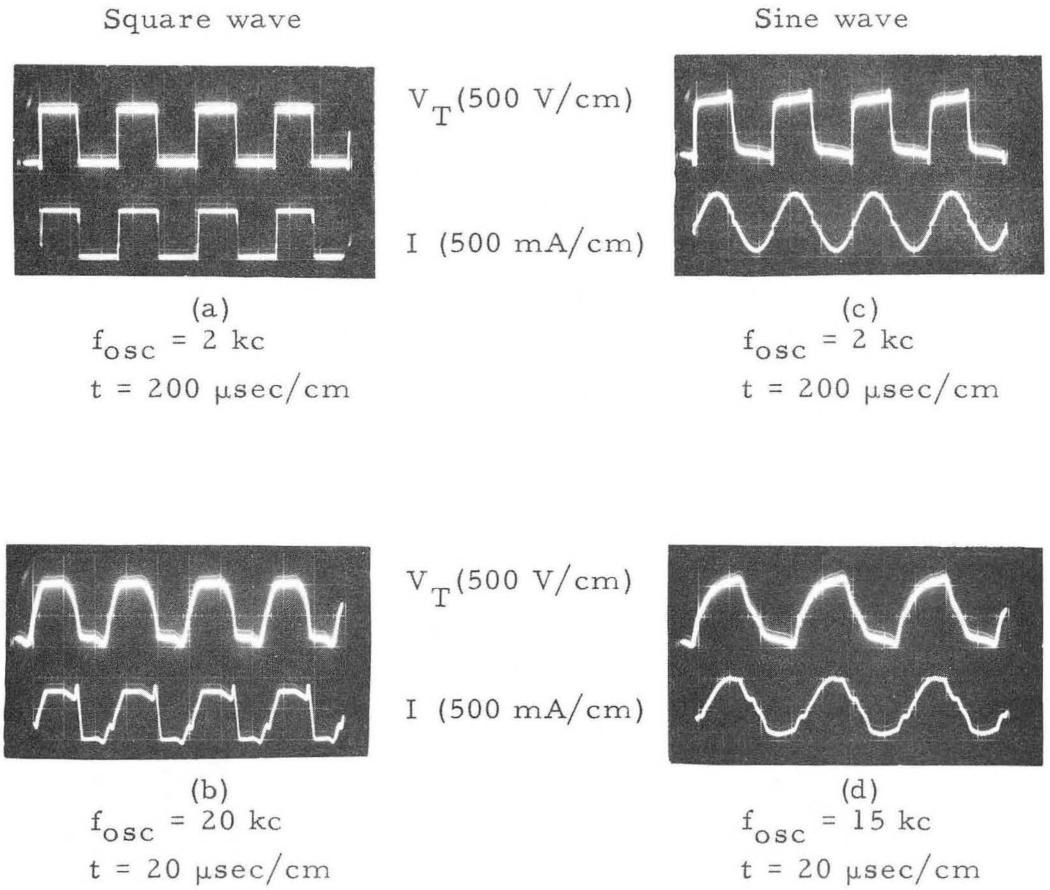

(a)
f_{osc} = 2 kc
t = 200 μsec/cm

(c)
f_{osc} = 2 kc
t = 200 μsec/cm

(b)
f_{osc} = 20 kc
t = 20 μsec/cm

(d)
f_{osc} = 15 kc
t = 20 μsec/cm

ZN-3755

Fig. C-5. Comparison of voltage and current vs oscillator frequency for Ne gas, R = 1.27 cm, p = 0.16 mm Hg, B = 0.

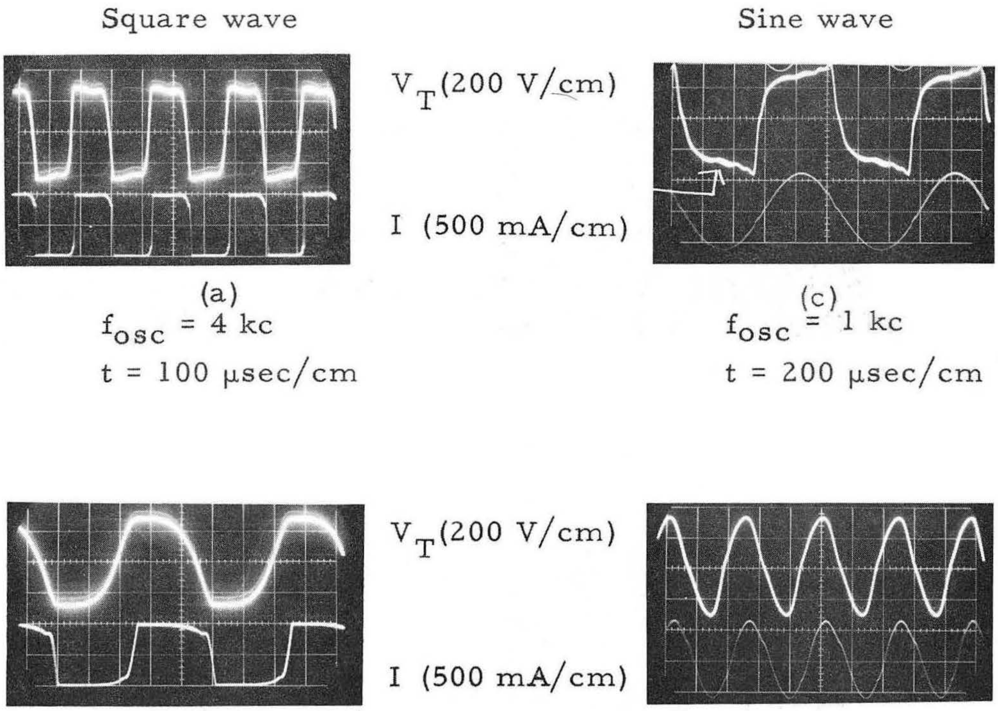

(a) f_{osc} = 4 kc
t = 100 μsec/cm

(c) f_{osc} = 1 kc
t = 200 μsec/cm

(b) f_{osc} = 10 kc
t = 20 μsec/cm

(d) f_{osc} = 8 kc
t = 100 μsec/cm

ZN-3756

Fig. C-6. Comparison of square-wave and sine-wave voltage and current vs oscillator frequency for Ne gas, R = 2.75 cm, p = 0.16 mm Hg, B = 0.

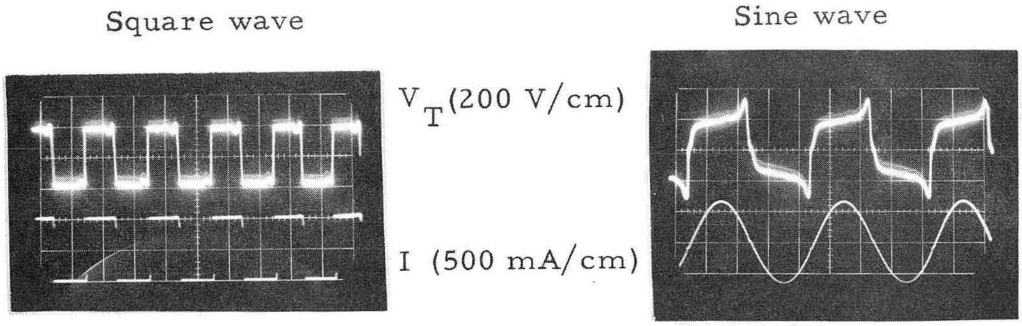

(a)
f_{osc} = 1 kc
t = 500 µsec/cm

(c)
f_{osc} = 500 cps
t = 500 µsec/cm

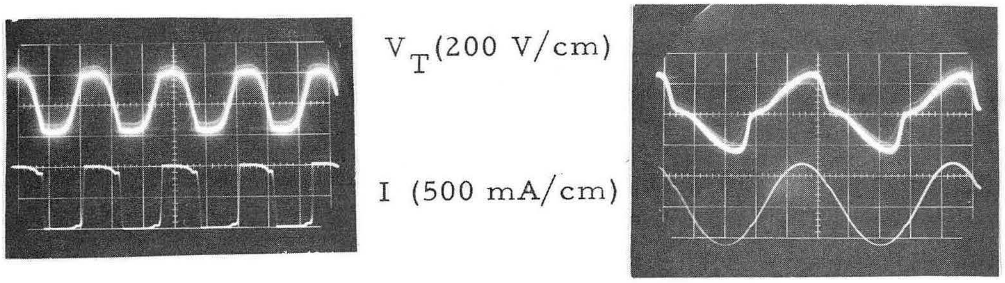

(b)
f_{osc} = 8 kc
t = 100 µsec/cm

(d)
f_{osc} = 2 kc
t = 100 µsec/cm

ZN-3757

Fig. C-7. Comparison of square-wave and sine-wave voltage and current vs oscillator frequency for Ar gas, R = 2.75 cm, p = 0.1 mm Hg, B = 0.

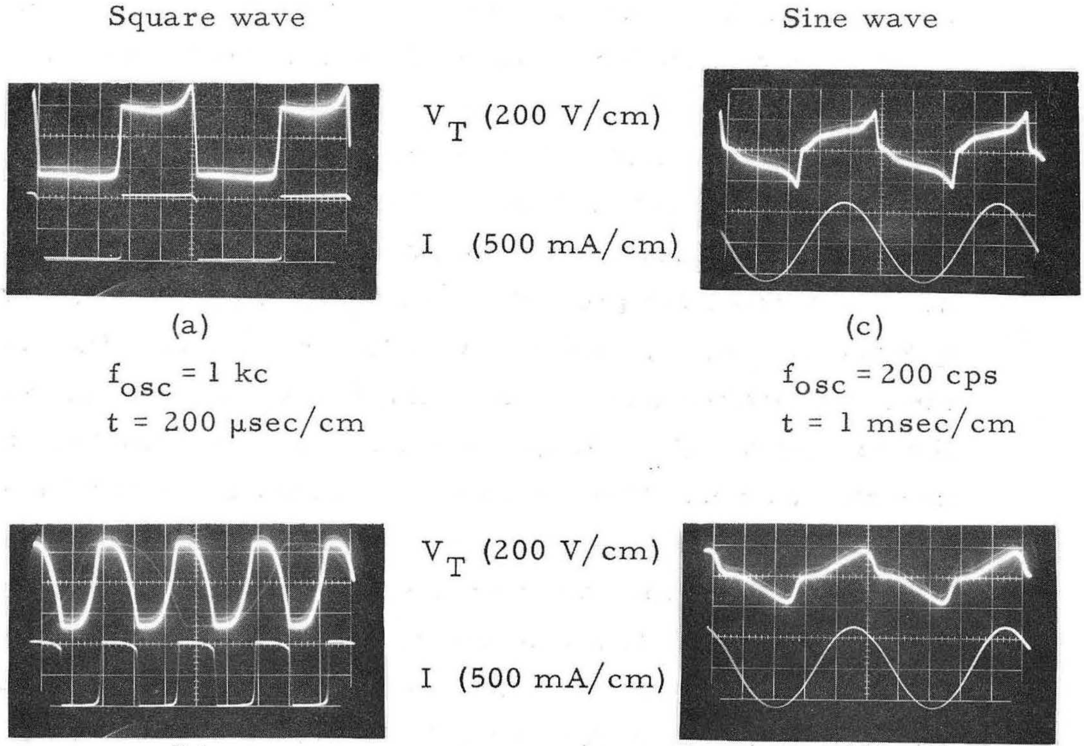

(a)
$f_{osc} = 1$ kc
$t = 200$ µsec/cm

(c)
$f_{osc} = 200$ cps
$t = 1$ msec/cm

(b)
$f_{osc} = 8$ kc
$t = 50$ µsec/cm

(d)
$f_{osc} = 2$ kc
$t = 100$ µsec/cm

ZN-3758

Fig. C-8. Comparison of square-wave and sine-wave voltage and current vs oscillator frequency for Ar gas, $R = 2.75$ cm, $I = 400$ mA, $p = 0.6$ mm Hg, $B = 0$.

D. Measurement of the Critical Magnetic Field

The critical magnetic fields in the ac discharges were determined by three different methods: the variation of the axial electric field of the positive column vs applied magnetic field, the variation of the total voltage across the discharge vs applied magnetic field, and the variation of the time-averaged light intensity vs applied magnetic field. Whenever the three methods were applied simultaneously, they gave exact agreement as to the onset of the instability.

The E_z-vs-B method has been widely used in previous dc experiments; however, the accurate determination of the actual value of the electric field presented a problem in the ac discharges. Frequently the electric field signal (difference between the voltages on the two probes) looked rather strange. At times it resembled neither the current nor the voltage wave shapes. This may have been due to several reasons. The two probes were not precisely the same distance from the wall, and one may have sampled the sheath region, since the voltage signals seen on each probe differed slightly in shape. This deviation was hardly noticeable on the oscilloscope screen, but due to the fact that the separate voltages on the probes were often greater than ten times the difference voltage (with respect to ground), the small deviation of the large scale corresponded to a much larger discrepancy when the difference was taken. Due to the ac impedance of the plasma, phase shifts existed and current and voltage wave shapes became somewhat distorted. These deviations were reflected in the separate probe signals and were also amplified when the differential voltage was obtained. Some distortion was also caused by limitations in the power supply (amplifier). Striations strongly affected the electric field signals when present [Fig. 12(b)], although they did not noticeably affect the time-averaged voltage across the tube. The undulations in the curves of Fig. 16 are due to these effects, and at times they completely masked the onset of the instability.

For these reasons, another method was used for determining the critical magnetic field. The total peak voltage across the discharge was plotted on the X-Y recorder vs B. This yielded a set of curves from which the critical fields were obtained. Samples of these curves follow in this appendix. The time-averaged light intensity was only used infrequently, mostly as a check on the other measurements.

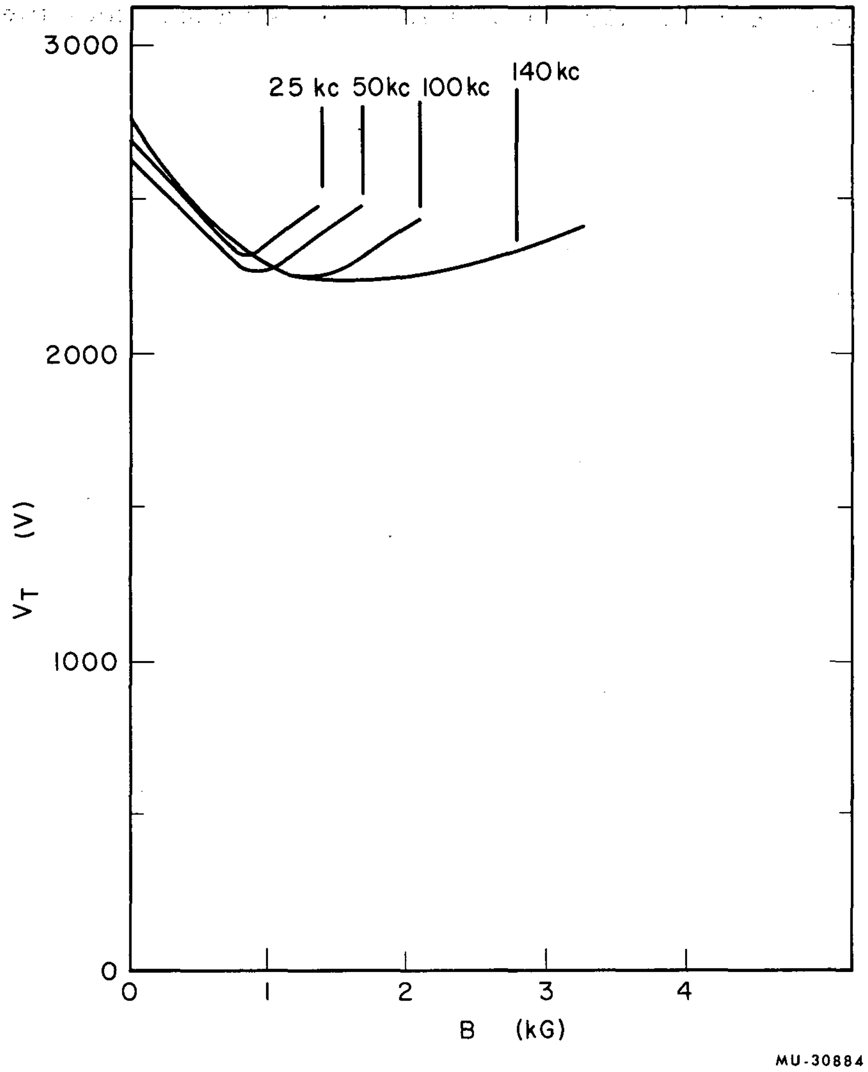

Fig. D-1. V_T vs B for H_2 gas, R = 1.27, p = 0.45 mm Hg, I = 500 mA, sine wave.

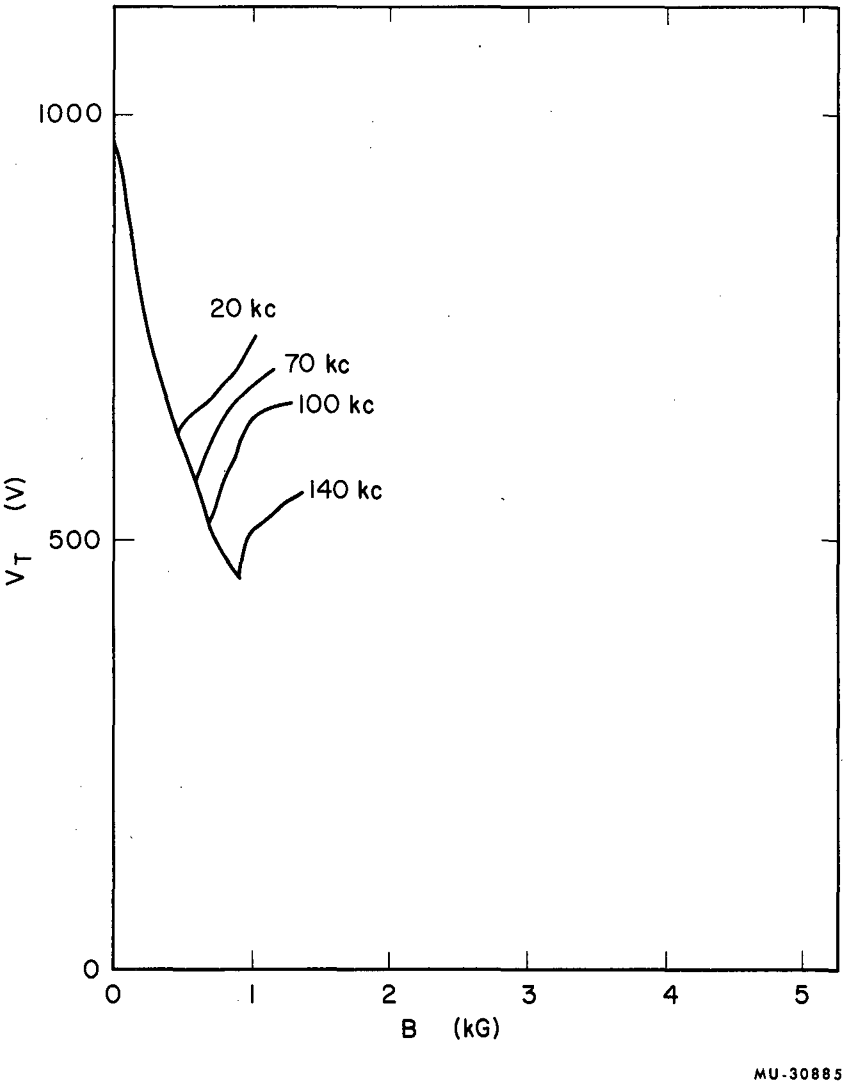

Fig. D-2. V_T vs B for D_2 gas, R = 1.27 cm, p = 0.1 mm Hg, I = 500 mA, sine wave.

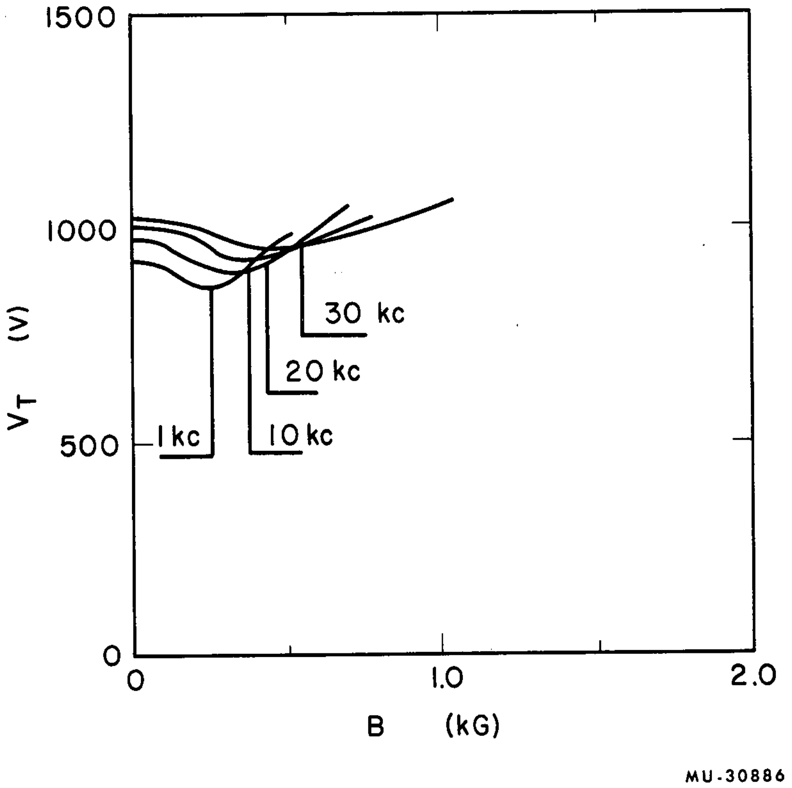

Fig. D-3. V_T vs B for D_2 gas, R = 2.75 cm, p = 0.2 mm Hg, I = 400 mA, square wave.

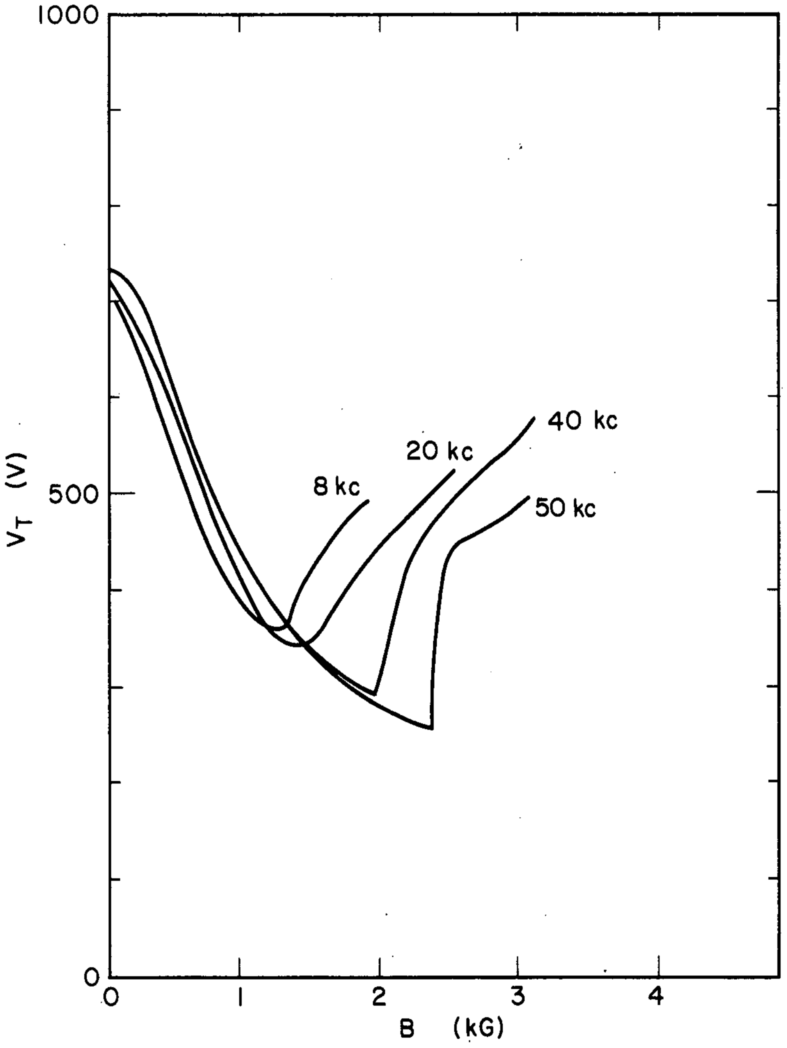

MU-30887

Fig. D-4. V_T vs B for He gas, R = 1.27 cm, p = 0.36 mm Hg, I = 500 mA, square wave.

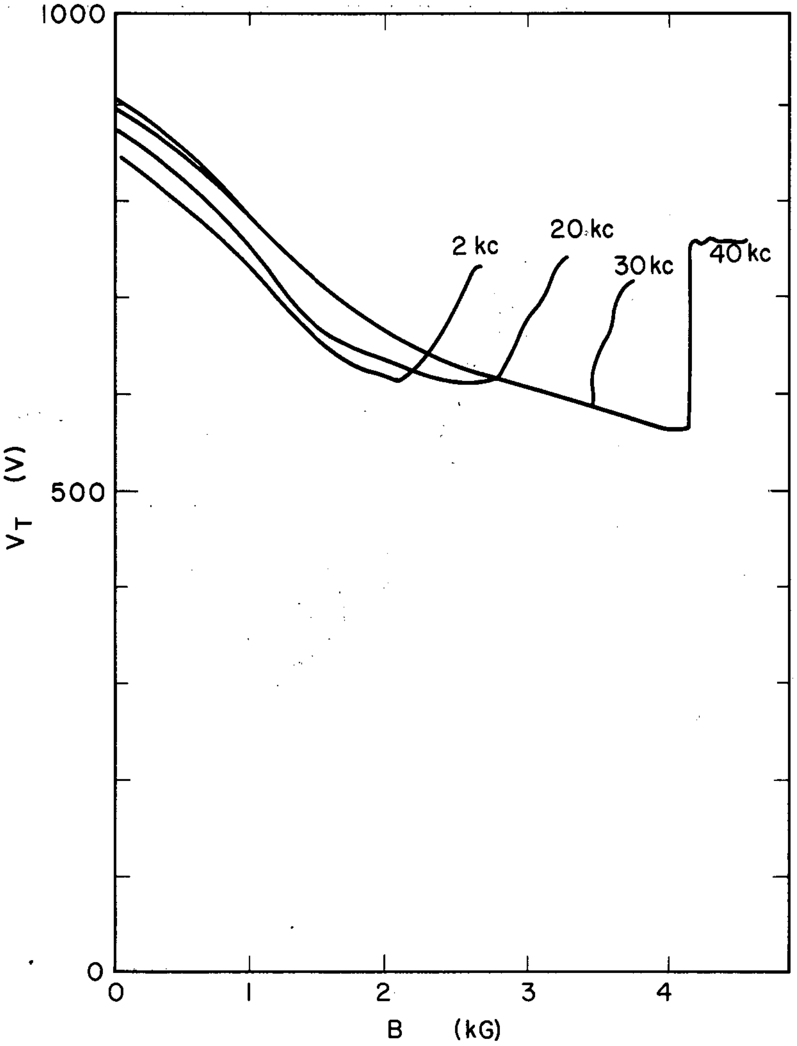

MU-30888

Fig. D-5. V_T vs B for He gas, R = 1.27 cm, p = 0.95 mm Hg, I = 500 mA, square wave.

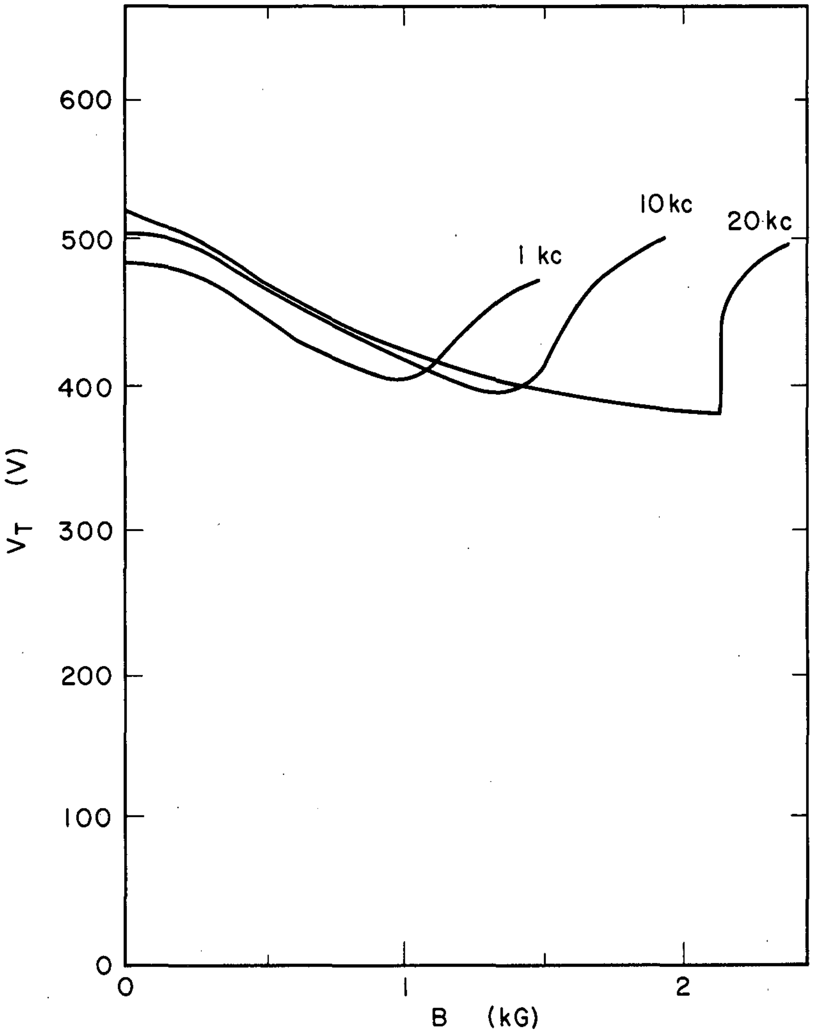

MU-30889

Fig. D-6. V_T vs B for He gas, R = 2.75 cm, p = 0.6 mm Hg, I = 500 mA, square wave.

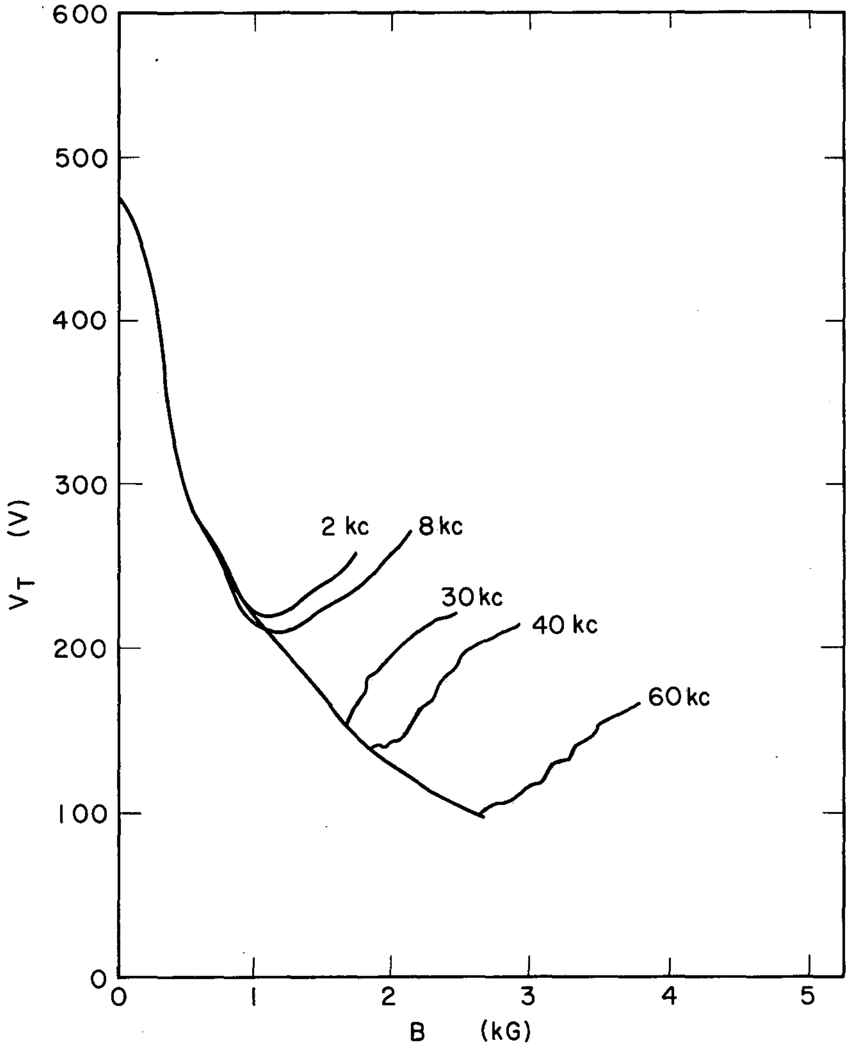

MU-30890

Fig. D-7. V_T vs B for Ne gas, R = 1.27 cm, p = 0.16 mm Hg, I = 400 mA, square wave.

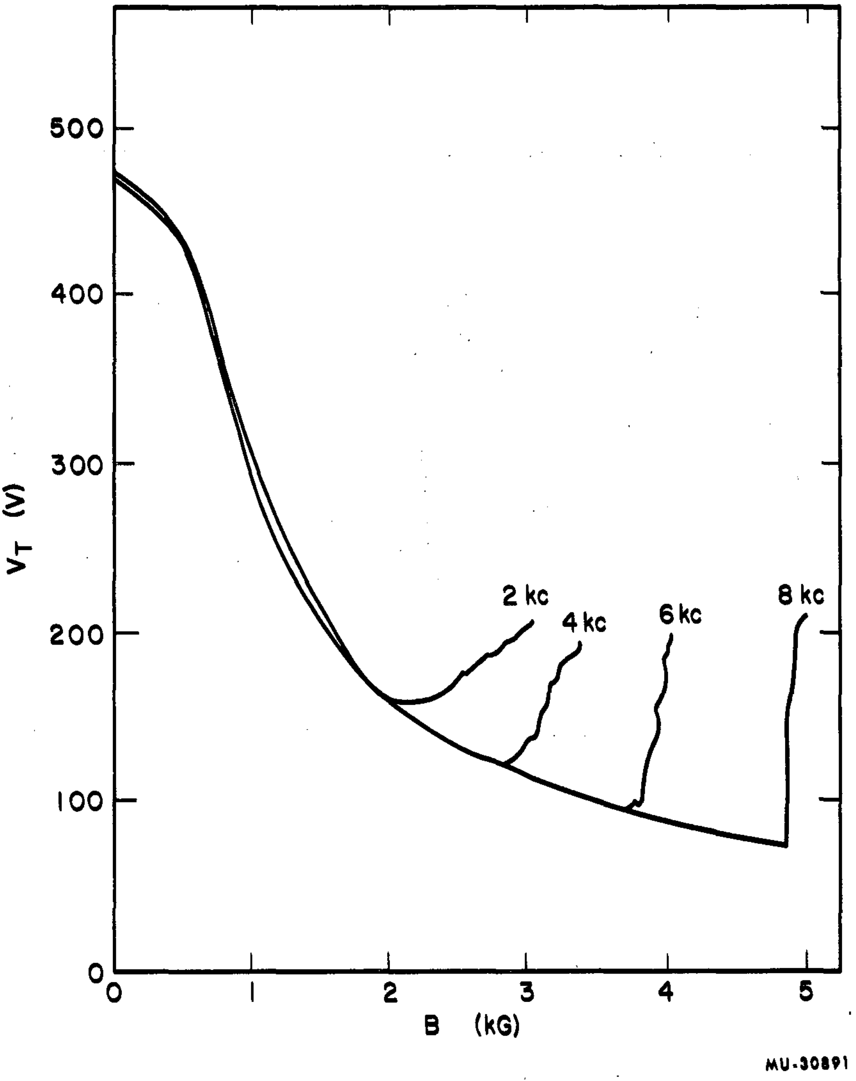

Fig. D-8. V_T vs B for Ne gas, R = 1.27 cm, p = 0.6 mm Hg, I = 400 mA, square wave.

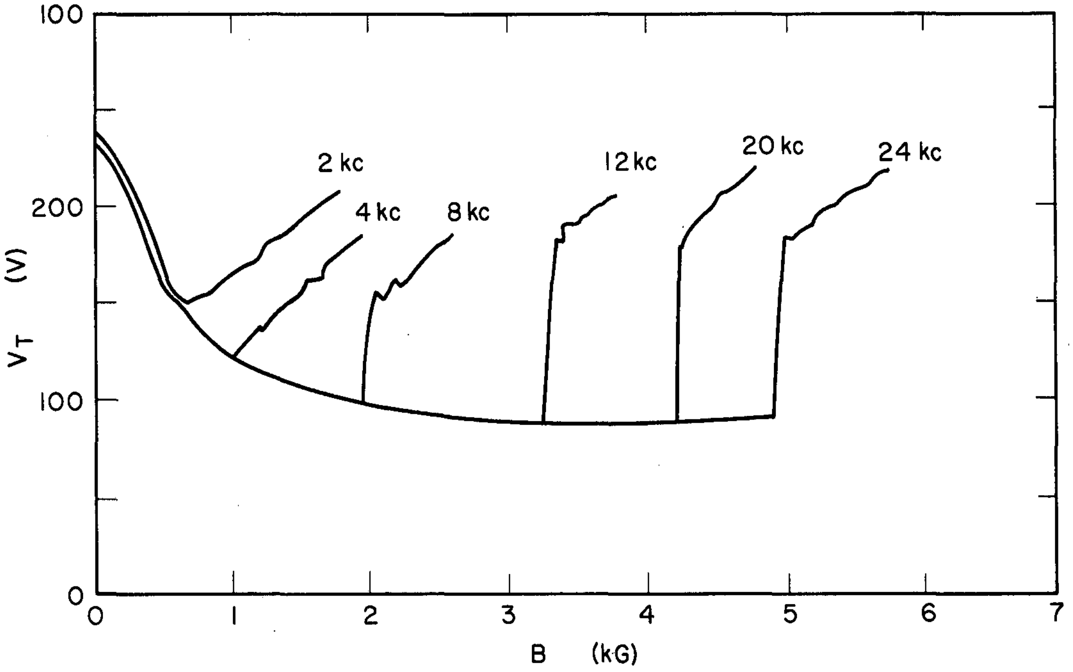

MU-30892

Fig. D-9. V_T vs B for Ne gas, R = 2.75 cm, p = 0.16 mm Hg, I = 400 mA, square wave.

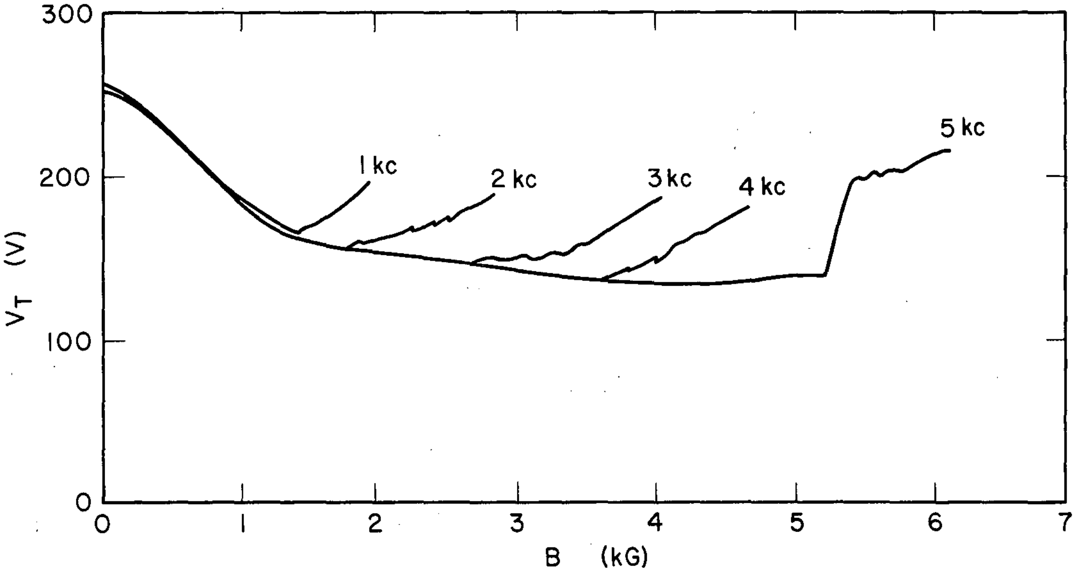

MU-30893

Fig. D-10. V_T vs B for Ne gas, R = 2.75 cm, p = 0.6 mm Hg, I = 500 mA, square wave.

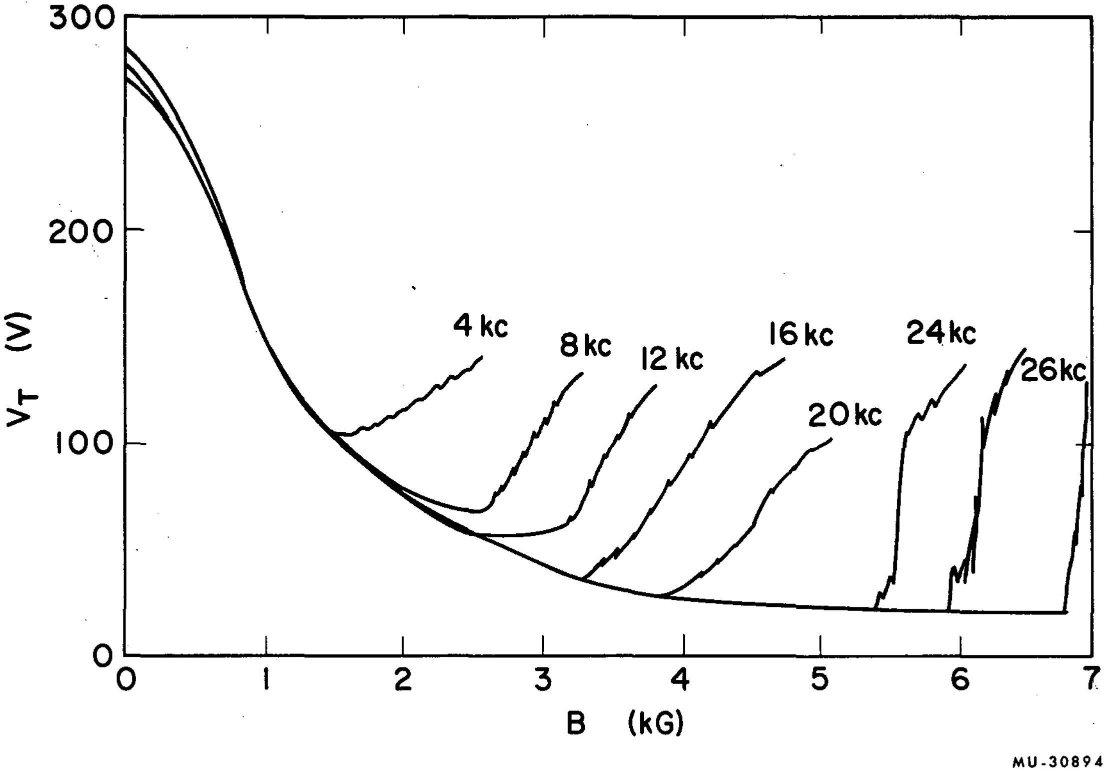

Fig. D-11. V_T vs B for Ar gas, R = 1.27 cm, p = 0.10 mm Hg, I = 500 mA, square wave.

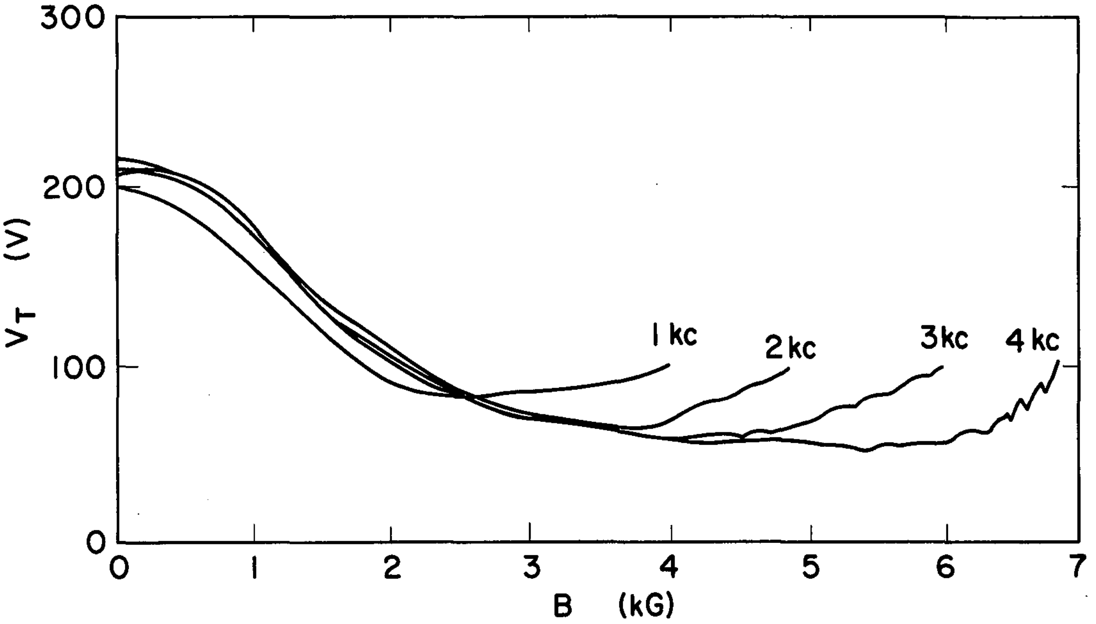

MU-30895

Fig. D-12. V_T vs B for Ar gas, R = 1.27, p = 0.4 mm Hg, I = 400 mA, square wave.

E. Curves of Im(ω), f vs Magnetic Field

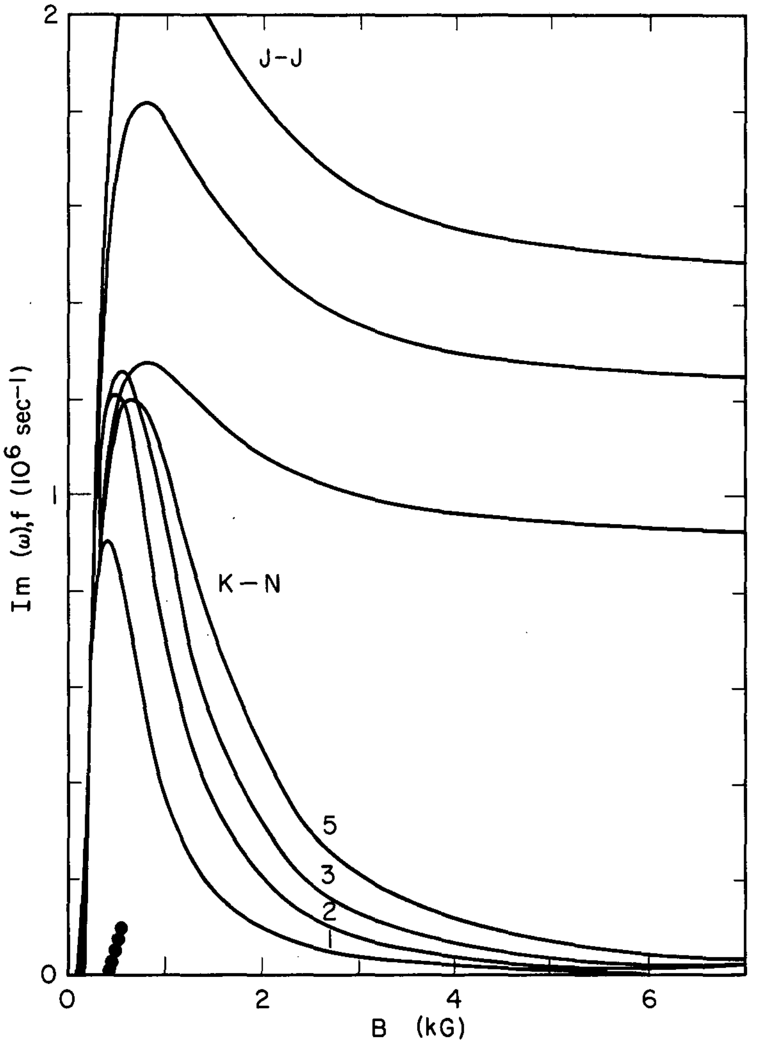

MU-30876

Fig. E-1. Im(ω), f vs B, with H_2^+, p = 0.15 mm Hg, R = 1.27 cm, I = 500 mA, square wave.

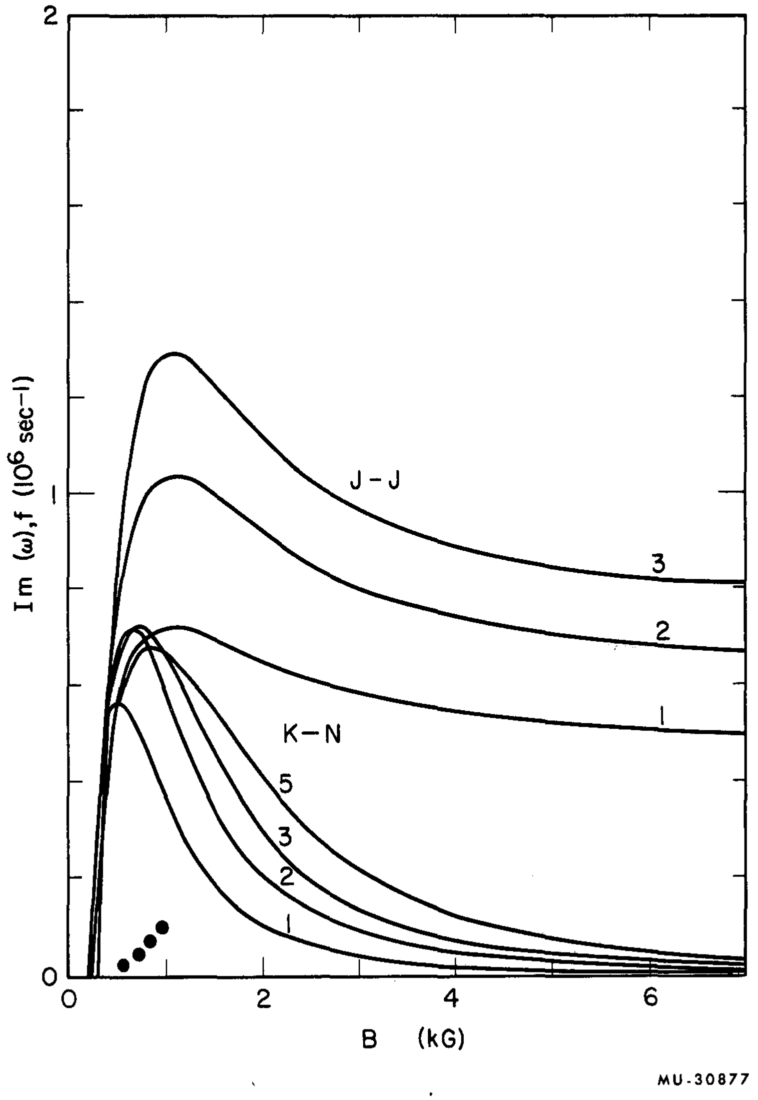

Fig. E-2. Im(ω), f vs B, with D_2^+, p = 0.16 mm Hg, R = 1.27 cm, I = 500 mA, square wave.

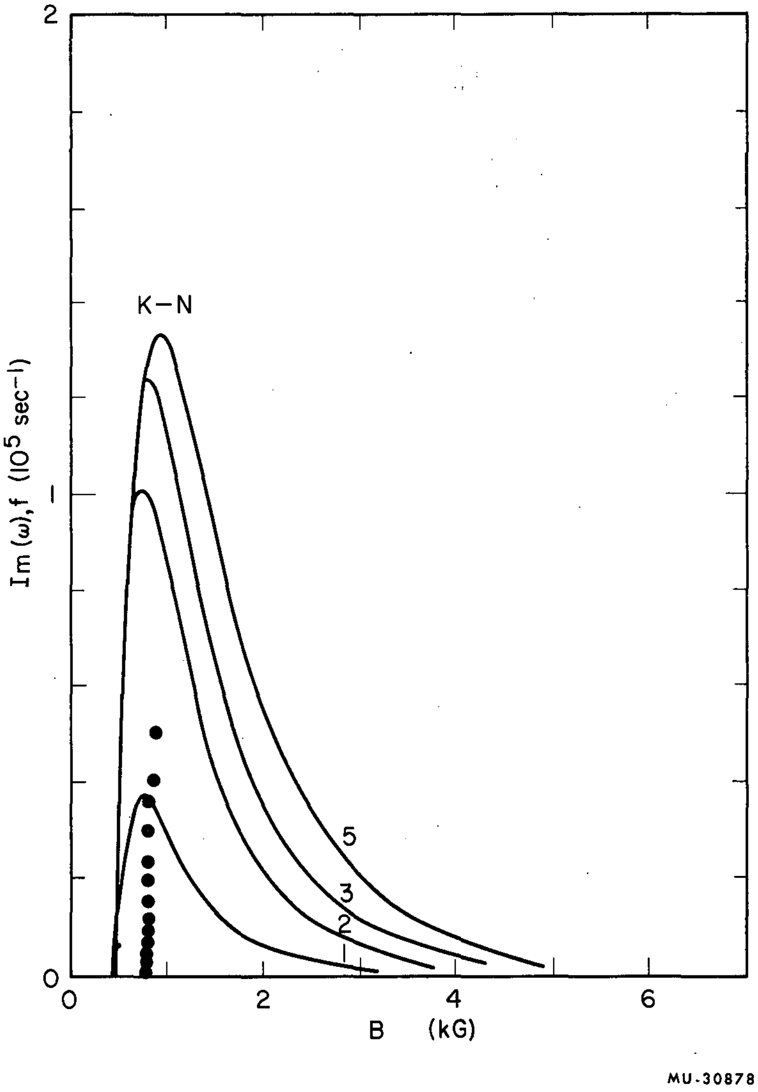

Fig. E-3. Im(ω), f vs B, with He$^+$, p = 0.13 mm Hg, R = 1.27 cm, I = 500 mA, square wave.

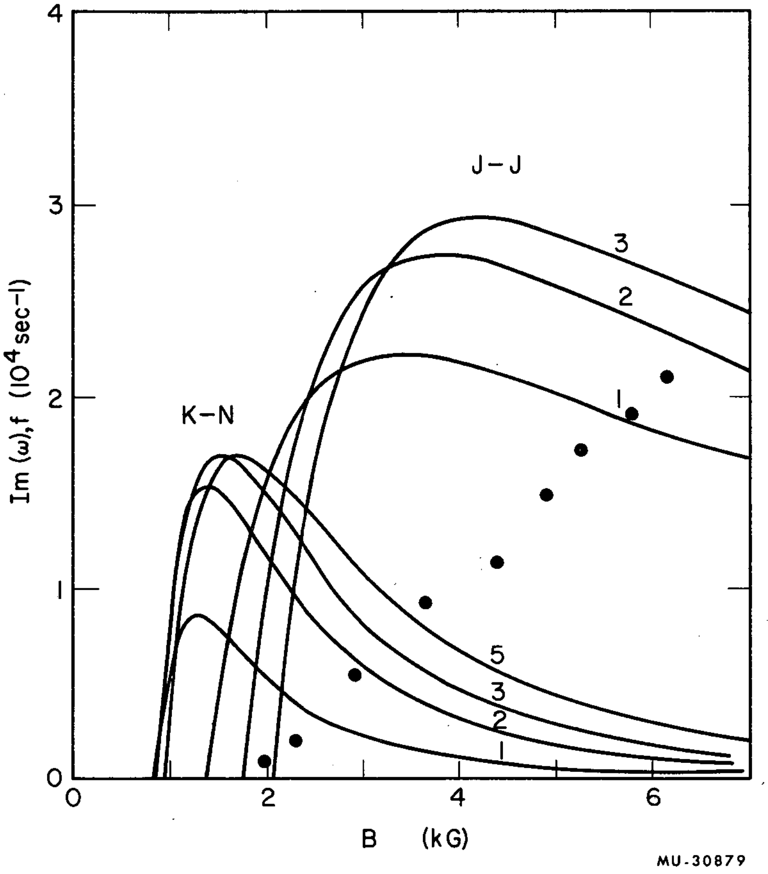

Fig. E-4. Im(ω), f vs B, with Ne_2^+, p = 0.50 mm Hg, R = 1.27 cm, I = 400 mA, square wave.

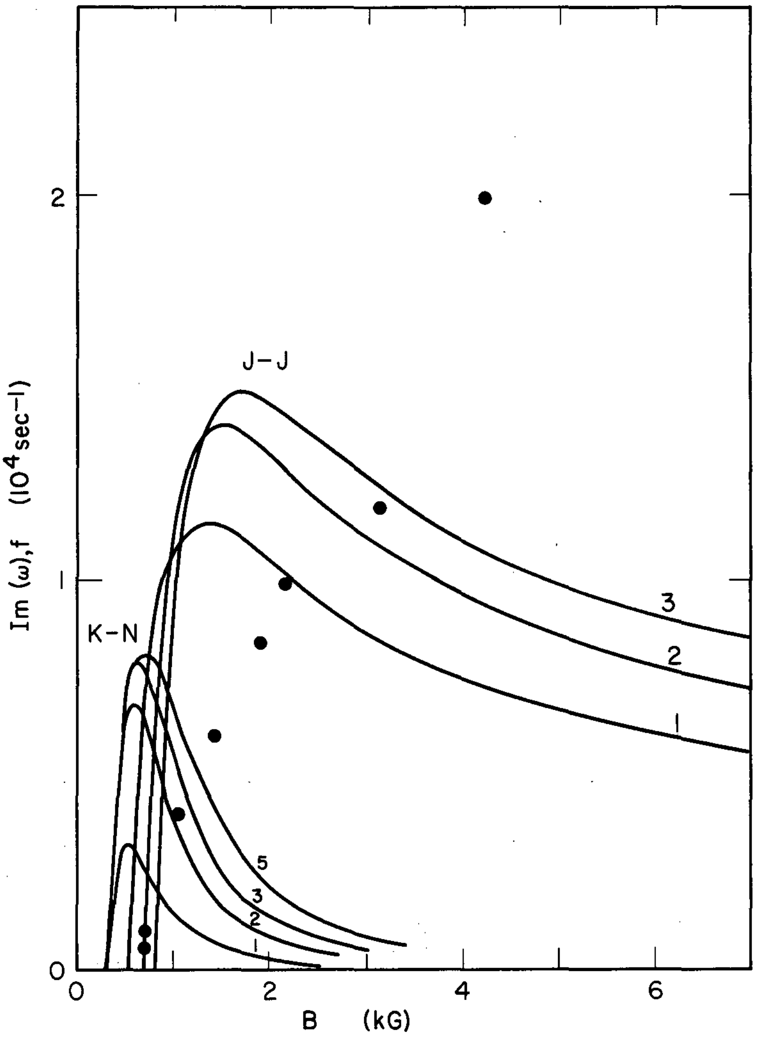

MU-30880

Fig. E-5. Im(ω), f vs B, with Ne_2^+, p = 0.18 mm Hg, R = 2.75 cm, I = 500 mA, square wave.

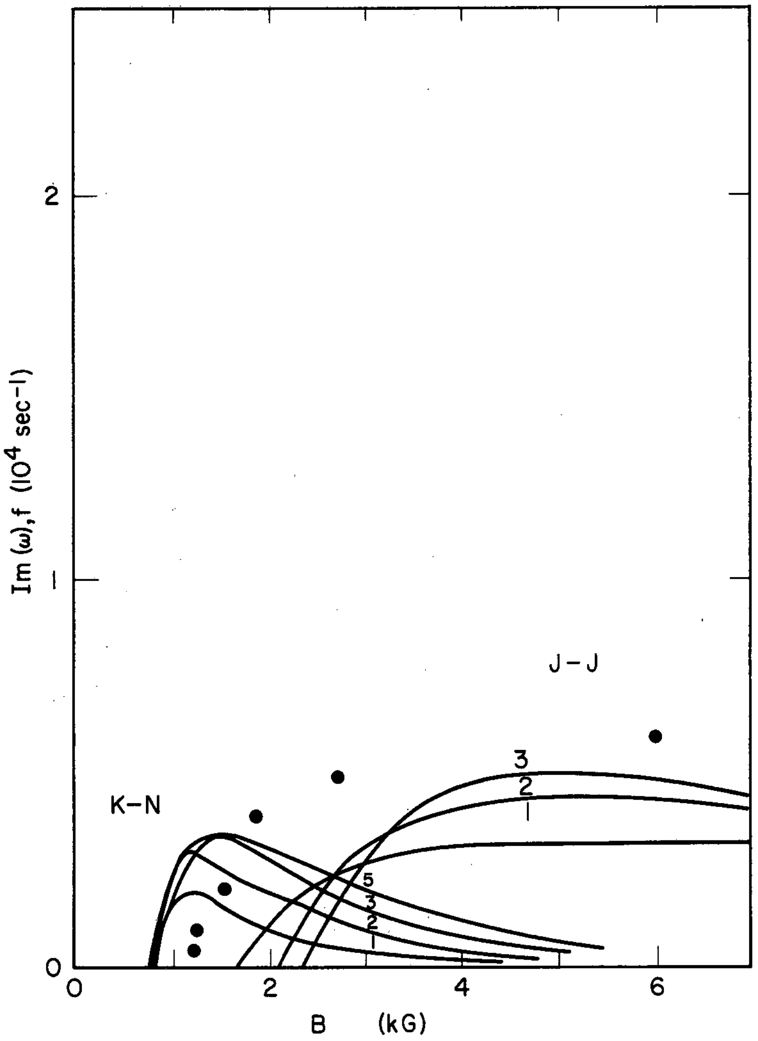

MU-30881

Fig. E-6. Im(ω), f vs B, with Ne^+, p = 0.52 mm Hg, R = 2.75 cm, I = 500 mA, square wave.

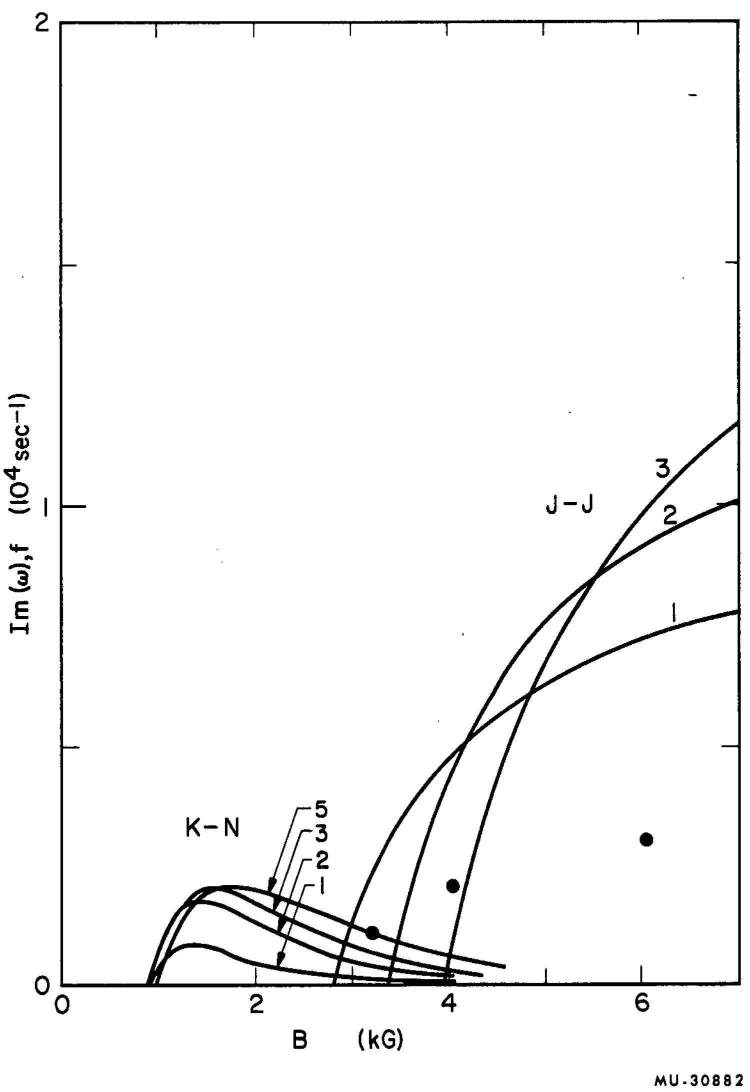

Fig. E-7. Im(ω), f vs B, with Ar_2^+, p = 0.6 mm Hg, R = 1.27 cm, I = 500 mA, square wave.

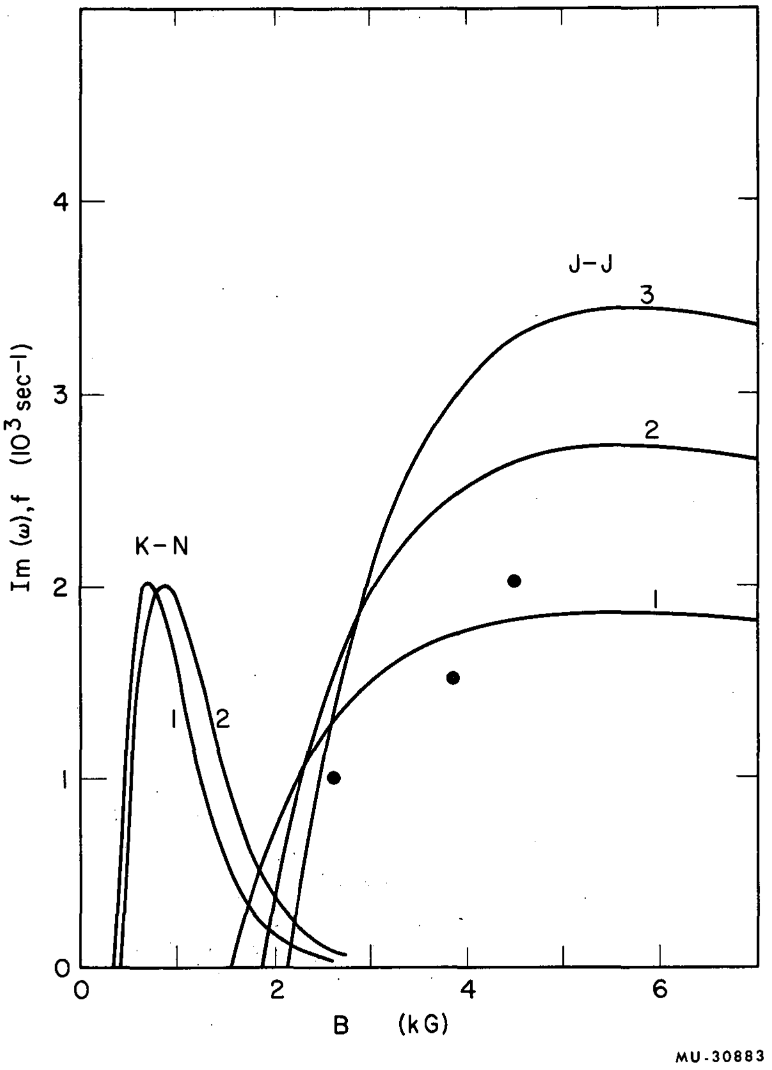

Fig. E-8. Im(ω), f vs B, with Ar_2^+, p = 0.6 mm Hg, R = 2.75 cm, I = 500 mA, square wave.

REFERENCES

1. T. K. Allen, G. A. Paulikas, and R. V. Pyle, Instability of the Positive Column in a Magnetic Field, Phys. Rev. Letters 5, 409 (1960).
2. G. A. Paulikas and R. V. Pyle, Phys. Fluids 5, 348 (1962).
3. B. Lehnert, in Proceedings of the Second United Nations International Conference on the Peaceful Uses of Atomic Energy (United Nations, Geneva, 1958), Vol. 32 p. 349.
4. F. C. Hoh and B. Lehnert, Phys. Fluids 3, 600 (1960).
5. G. V. Gierke and K. H. Wöhler, Nucl. Fusion Suppl. Part 1 (1962).
6. B. B. Kadomtsev and A. V. Nedospasov, J. Nuclear Energy, Part C, 1, 230 (1960).
7. F. C. Hoh, Phys. Rev. Letters 4, 559 (1960).
8. F. C. Hoh, Phys. Fluids 5, 22 (1962).
9. R. R. Johnson and D. A. Jerde, Phys. Fluids 5, 988 (1962).
10. Y. H. Ichikawa, S. Misawa, and Y. Sasakura, The Helical Instability of the Weakly Ionized Plasmas in a Longitudinal Magnetic Field, 1962 (unpublished).
11. A. Simon and G. Guest, Phys. Fluids 5, 121 (1962).
12. H. S. Robertson, Bull. Am. Phys. Soc. 7, 422 (1962).
13. I. L. Ivanov and S. W. Ryvkin, J. Tech. Phys. (U.S.S.R.) 28, 774 (1958); Sov. Phys.-Tech. Phys. 3, 722 (1958).
14. R. D. Larrabee and M. C. Steele, J. Appl. Phys. 31, 1519 (1960).
15. J. Bok and R. Veilex, Compt. rend. 248, 2300 (1959).
16. M. Glicksman and R. A. Powlus, Phys. Rev. 121, 1659 (1961).
17. G. Francis, in Handbuch Der Physik, ed. by S. Flugge (Springer-Verlag, Berlin, 1956), Vol. 22.
18. S. C. Brown, Basic Data of Plasma Physics (John Wiley & Sons, Inc., New York, 1959).
19. R. J. Bickerton and A. von Engel, Proc. Phys. Soc. (London), B69 468 (1956).
20. L. Tonks and I. Langmuir, Phys. Rev. 34, 876 (1929).

21. W. Schottky, Physik. Z. 25, 342 (1924).

22. D. Bohm, E. H. S. Burhop, H. S. W. Massey, and R. M. Williams, in The Characteristics of Electrical Discharges in Magnetic Fields, ed. by A. Guthrie and R. K. Wakerling (McGraw-Hill Book Company, Inc., New York, 1949).

23. R. A. Ellis, Jr., L. P. Goldberg, and J. G. Gorman, Phys. Fluids 3, 468 (1960).

24. W. H. Bostick and M. A. Levine, Phys. Rev. 97, 13 (1955).

25. J. F. Bonnal, G. Briffod, and C. Manus, Compt. rend. 250, 2859 (1960).

26. I. B. Bernstein, E. A. Frieman, R. M. Kulsrud, and M. N. Rosenbluth, Phys. Fluids 3, 136 (1960).

27. L. Spitzer, Jr., Phys. Fluids 3, 659 (1960).

28. L. B. Bierman and D. Pfirsch, Z. Naturforsch, 15a, 10, 14 (1960).

29. G. Francis, Ionization Phenomena in Gases (Butterworth & Company, London, 1960).

30. M. Pahl, Z. Naturforsch, 12a, 632 (1957).

31. W. P. Allis and S. J. Buchsbaum, Notes on Plasma Dynamics, Summer Program (1959) MIT.

32. H. S. Robertson, M. A. Hakeen, J. Appl. Phys. 31, 2063 (1960).

33. A. von Engel, Ionized Gases (Oxford University Press, New York, 1955).

34. A. von Engel and M. Steenbeck, Elektrische Gasentladungen, ihn Physik u. Technik (Verlag Julius Springer, Berlin, 1934), Vol. 2.

35. D. Bohm, E. H. S. Burhop, H. S. W. Massey, and R. M. Williams, The Characteristics of Electrical Discharges in Magnetic Fields, ed. by A. Guthrie and R. K. Wakerling (McGraw-Hill Book Company, Inc., New York, 1949).

36. L. S. Hall, Phys. Fluids 4, 388 (1961).

37. F. C. Hoh, Rev. Mod. Phys. 34, 267 (1962).

38. L. V. Kantorovich and V. I. Krylov, Approximative Methods of Higher Analyses, (Interscience Publishers, Inc., New York, 1958).

39. G. Ecker (Institute for Theoretical Physics, University of Bonn, Bonn, Germany), private communication.

40. B. Lehnert, in High Magnetic Fields (John Wiley & Sons, Inc., New York, 1962).

41. I. Langmuir and H. Mott-Smith, Gen. Elec. Rev. 27, 449, 538, 616, 762, 810 (1924).

42. D. Bohm, E. H. S. Burhop, H. S. W. Massey and R. M. Williams, The Characteristics of Electrical Discharges in Magnetic Fields, ed. by A. Guthrie and R. K. Wakerling (McGraw-Hill Book Company, Inc., New York, 1949), Vol. 5, p. 13.

43. E. O. Johnson and L. Malter, Phys. Rev. 80, 58 (1950).

44. E. Spenke, Z. Physik 127, 221 (1950).

45. L. M. Chanin (Honeywell Research Center, Minneapolis, Minnesota), private communication.

46. N. A. Karelina, J. Phys. (U.S.S.R.), 6, No. 5 (1942).

47. B. Klarfeld, J. Phys. (U.S.S.R.) 5, Nos. 2-3 (1941).

48. R. Seeliger and R. Hirchert, Ann. Phys. 11, 817 (1931).

49. R. L. F. Boyd and N. D. Twiddy, Proc. Roy. Soc. (London) A250, 53 (1959).